Study of Topological Edge States in Selected Solid State Systems

Shivam Yadav

A thesis presented for the degree of

Doctor of Philosophy

Supervisor: Dr. Hab. Andrzej Ptok, Prof. IFJ PAN

Co-supervisor: Dr. Hab. Przemysław Piekarz, Prof. IFJ PAN

THE HENRYK NIEWODNICZAŃSKI
INSTITUTE OF NUCLEAR PHYSICS
POLISH ACADEMY OF SCIENCES

Department of Materials Research by Computers (NZ33)

The Henryk Niewodniczański Institute of Nuclear Physics Polish Academy of Sciences

September 22, 2025

Acknowledgement

I would like to express my sincere appreciation to all those who have supported me throughout the process of writing this thesis. This work would not have been possible without their guidance, encouragement, and understanding.

First and foremost, I extend my deepest gratitude to my supervisor, Andrzej Ptok and co-supervisor, Przemysław Piekarz for their invaluable guidance, insightful feedback, and constant encouragement. Their expertise and availability were crucial in shaping this research from its initial stages to the final product.

I wish to acknowledge the hospitality of the Solid States Physics Laboratory (Le Laboratoire de Physique des Solides) at Université Paris-Saclay during my short-term visit. I am deeply grateful to the late Mark-Oliver Goerbig, for his pivotal role in this project. The valuable discussions I had with him and my supervisor have profoundly shaped this thesis.

Finally, I want to express my heartfelt appreciation for my family and friends. This thesis is a culmination of both my effort and the support I have received from all of you.

English abstract

Topological materials and their disorder-robust edge states have captured significant attention, finding applications beyond fundamental physics. The dimensionality of the edge plays a paramount role in the nature of these edge modes. One dimensional (1D) topological materials, when coupled with a proximate superconductor, are capable of hosting the elusive Majorana bound states, whose non-Abelian nature holds great promise for applications in quantum computing. In this thesis, we studied such a quasi 1D system resembling a ladder made of coupled nanowires. We found that within tight binding description, the ladder with periodic boundary condition realizes topological phase with the topological invariant in range $[-3, 3]$. We show that this is a direct result of the coupling between the nanowires and the topological phase can altered by tuning the coupling strengths between wires. Furthermore, the finite system hosts the Majorana bound modes within the superconducting gap for appropriate parameters.

The two and three dimensional (2D and 3D) topological materials on the other hand have garnered interest due to the gapless states they manifest in the Brillouin zone. These gapless states behave like quasi particles which have the characteristics of the Dirac and Weyl fermions, naturally classifying their host with Dirac and Weyl semimetals (DSM and WSM) respectively. These materials are highly promising for next-generation electronics and spintronics due to their high electron mobility and potential for low-power, high-speed devices. In order to better understand the edge states we study an interface of an insulator and a WSM. We use the low energy effective model description of a time reversal WSM which hosts four Weyl nodes (gapless states). Choosing the parameters which lead to desired interface we solve the problem numerically. Employing the spectral function, we discuss various observations and properties of the edge states of the interface.

Abstrakt w języku polskim

Materiały topologiczne i ich odporne na nieporządek stany brzegowe wzbudziły duże zainteresowanie, znajdując potencjalne zastosowania wykraczające poza badania podstawowe. Wymiarowość krawędzi odgrywa kluczową rolę w naturze tych stanów. Jednowymiarowe (1D) materiały topologiczne, sprzężone z pobliskim nadprzewodnikiem, są zdolne do tworzenia stanów związania Majorany, których nieabelowa natura stwarza potencjał do ich zastosowań w komputerach kwantowych. W niniejszej rozprawie badaliśmy taki quasi-1D układ, w postaci drabinki zawierającej dwa równoległe sprzężone łańcuchy. Stwierdziliśmy, w ramach modelu ciasnego wiązania, że układ z periodycznymi warunkami brzegowymi realizuje fazę topologiczną z niezmiennikiem topologicznym w zakresie $[-3, 3]$. Wykazujemy, że jest to bezpośredni wynik sprzężenia między nanodrutami, a fazę topologiczną można zmienić poprzez dostrojenie wartości tego sprzężenia. Co więcej, skończony układ zawiera stany związane Majorany w przerwie nadprzewodzącej w pewnych zakresach parametrów.

Z drugiej strony, materiały topologiczne dwu- i trójwymiarowe (2D i 3D) wzbudziły zainteresowanie ze względu na stany bezprzerwowe, które manifestują się wewnątrz strefy Brillouina. Te stany bezprzerwowe zachowują się jak quasi-cząstki posiadające cechy fermionów Diraca i Weyla, naturalnie klasyfikując bazowy materiał jako półmetal Diraca i Weyla (DSM i WSM). Materiały te są wysoce obiecujące dla elektroniki nowej generacji i spintroniki ze względu na wysoką ruchliwość elektronów i potencjał dla urządzeń o małej mocy i dużej szybkości. Aby lepiej zrozumieć stany krawędziowe, badamy interfejs pomiędzy izolatorem i WSM. W tej części, wykorzystujemy nieskoenergetyczny model efektywny WSM z symetrią odwrócenia w czasie, który zawiera cztery węzły Weyla (stany bezprzerwowe). Wybierając parametry prowadzące do pożądanego interfejsu, rozwiązujemy problem numerycznie. Wykorzystując funkcję widmową, omawiamy różne obserwacje i właściwości stanów krawędziowych interfejsu.

Contents

Chapter 1

Introduction

The field of condensed matter physics has undergone significant evolution, characterized by groundbreaking experimental and theoretical advancements that have profoundly shaped our understanding of matter. At the turn of the 20^{th} century, Max Planck introduced the concept of quantized energy levels to address the problem of blackbody radiation. His work marked the beginning of quantum mechanics. Max Plank with his idea of quanta revolutionized physics which ultimately led to formulation of Matrix mechanics by Heisenberg and Schrodinger's wave formulation. These formulations became a powerful tool in understanding the electronic and structural properties of solids, forming the basis of solid state physics.

While early condensed matter research primarily focused on symmetry-breaking phenomena, the integration of topology introduced a paradigm shift. Topology, a branch of mathematics dealing with properties invariant under continuous deformations, offered a novel framework for analyzing quantum systems. This transition began with the discovery of quantum Hall effect (QHE), discovered by Klaus von Klitzing in 1980 [1, 2]. This was the first experimental observation of the quantization of the electrical conductance and the discovery was awarded the 1985 Nobel Prize in Physics. The underlying topological phenomenon was put forth by Thouless *et. al* [3] in 1982. This marked the first instance that certain material properties are governed by topological invariants rather than conventional symmetry considerations.

This insight kick-started an extensive theoretical and experimental exploration into systems dominated by topology. Unlike traditional phases of matter characterized by local order parameters, topological phases are defined by global wavefunction properties. The interplay between topology and quantum mechanics has emerged as a central theme in condensed matter physics, leading to the identification of novel materials and phenomena [4–8].

The 1980s and 1990s saw extensive studies of the fractional quantum Hall effect

(FQHE) [8], where electrons in high magnetic fields form correlated states with fractional charge excitations. The FQHE was pivotal in introducing the concept of topological order, characterized by long-range quantum entanglement rather than symmetry-breaking [9]. The discovery of the FQHE, which is an even more complex version of the QHE. While it is not always explicitly listed under *topological materials*, the exotic quantum fluid they discovered is a prime example of a state of matter with topological order earning Robert B. Laughlin, Horst L. Störmer, and Daniel C. Tsui the 1998 Nobel Prize. Xiao-Gang Wen's seminal work further elucidated how topological order manifests through ground-state degeneracy and quasi-particles excitation.

The early 21st century witnessed a renaissance in topology with the theoretical prediction and subsequent experimental realization of topological insulators (TIs) like Bi_2Se_3. Pioneering contributions by Charles Kane, Shou-cheng Zhang, and collaborators established the $\mathbb{Z}_2$ topological invariant as the fundamental quantity behind these phases, which are insulating in the bulk but exhibit robust surface states protected by time-reversal symmetry [5, 10]. Experimental confirmations using angle-resolved photoemission spectroscopy (ARPES) revealed Dirac-like surface states in materials such as Bi_2Se_3, validating theoretical predictions [11]. The 2016 Nobel Prize was awarded to David J. Thouless, F. Duncan M. Haldane, and J. Michael Kosterlitz for their foundational work in the field of topological materials.

Topological superconductors and Weyl semimetals (WSM) expanded the scope of topological physics. The potential observation of Majorana zero modes in hybrid superconducting structures [12], and the observation of Weyl fermions in TaAs crystals [13] highlighted the potential for novel quasiparticles in condensed matter systems.

1.1 Layman's approach to topology in Condensed Matter Physics

Topology, at its core, concerns itself with the qualitative properties of objects that are preserved under smooth deformations such as stretching or bending, but not tearing or sticking. The central idea of this field are concepts such as continuity, connectedness, and compactness. These notions enable the classification of spaces and structures in ways that generalize the traditional geometric metrics such as distance or angles. In the context of condensed matter physics, these topological ideas find natural applications in the analysis of phase transitions, quantum states, and wavefunctions.

A quantum system, described by a wavefunction, often resides in a parameter space that

can be treated as a topological manifold. For instance, consider the parameter space of a one-dimensional (1D) quantum system with a Hamiltonian dependent on momentum. The topology of the eigenstates, as momentum varies, encodes critical physical information about the system, such as the presence of edge states or quantized conductance.

We will review some of the key fascinating interplay between bulk and boundary properties is central to phenomena like the integer quantum Hall effect (IQHE) in Sec. (1.1.1), where quantized resistance arises from chiral edge modes in a two-dimensional (2D) electron gas subjected to a strong magnetic field. The principles of the IQHE, and the notion of robust boundary states, have since been generalized to a wider class of materials. We review the current research in 1D topological materials (Sec. (1.1.3)) with protected edge modes, and 2D and three-dimensional (3D) topological materials (Sec. (1.1.2)), which host unique conducting surface or edge states protected by time-reversal symmetry. These exotic states promise fault-tolerant quantum computing and low-power electronics.

1.1.1 Integer Quantum Hall Effect

The classical Hall effect, discovered by Edwin Hall in 1879, describes the emergence of a voltage perpendicular to both an applied current and a magnetic field in a conductor as shown in Fig. 1.1. This Hall voltage ($V_H = V_x$) arises due to the Lorentz force acting on the charge carriers. The Hall resistance (ratio of Hall voltage to current, V_x/I_y) is typically proportional to the magnetic field and inversely proportional to the carrier density. However, under extreme conditions of low temperatures (typically below 1 K) and strong magnetic fields (typically above 10 T), 2D electron systems exhibit a remarkable deviation from classical behavior known as the IQHE. This effect, first observed by Klaus von Klitzing in 1980 [1], reveals a precise quantization of the Hall conductance, providing profound insights into the quantum nature of electronic transport.

The IQHE is typically observed in high-mobility 2D electron system formed at the interface of semiconductor heterostructures, such as GaAs/AlGaAs. These structures confine electrons to a thin layer, effectively creating a 2D system. The experimental setup involves cooling the sample to temperatures, ranging in the mK to K range, to minimize thermal fluctuations. A strong magnetic field is applied perpendicular to the plane of the electron system as shown in Fig. 1.1. A constant current is then passed through the system, and both the longitudinal voltage (along the direction of current flow, V_x) and the Hall voltage (perpendicular to the current flow, V_y) are measured using a four-terminal measurement configuration to eliminate the effects of contact resistance on the measured voltages. The Hall

conductance, σ_{xy} is given by

$$\sigma_{xy} = \frac{I}{V_H} \tag{1.1}$$

where I is the current and V_H is the Hall voltage (in this case V_y), is found to be quantized in integer multiples of the fundamental constant e^2/h, where e is the elementary charge and h is Planck's constant. The quantization of the Hall conductance in integer multiples is termed as IQHE. It is customary to report the Hall resistance as a function of magnetic field which displays the plateaus making the quantization a central theme as shown in Fig. 1.2

To elucidate this better, consider a semiclassical picture of an electron system confined in the xy-plane subjected to a uniform magnetic field $\mathbf{B} = B\hat{z}$ along the z-direction. The Hamiltonian for a single electron with charge $-e$ and mass m^* (effective mass) is given by:

$$H = \frac{1}{2m^*}(\mathbf{p} + e\mathbf{A})^2 \tag{1.2}$$

where $\mathbf{p} = (p_x, p_y) = (-i\hbar\partial/\partial x, -i\hbar\partial/\partial y)$ is the momentum operator and $\mathbf{A}$ is the vector potential such that $\mathbf{B} = \nabla \times \mathbf{A}$. We can choose the Landau gauge: $\mathbf{A} = (0, Bx, 0)$. In this gauge, the Hamiltonian becomes:

$$H = \frac{1}{2m^*}\left[p_x^2 + (p_y + eBx)^2\right] \tag{1.3}$$

Since the Hamiltonian does not depend on y, the momentum in the y-direction, $p_y = \hbar k_y$, is

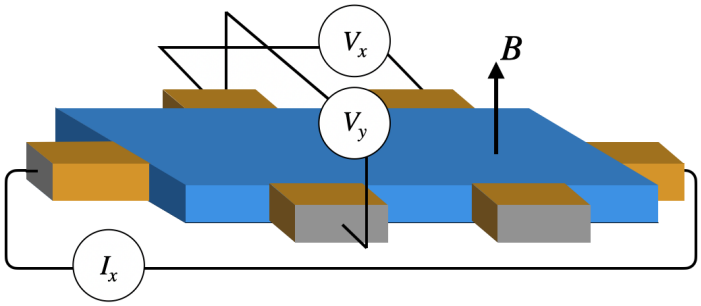

Figure 1.1: The setup shows a slab of material with six contact points to measure the voltage and current across the slab. The external magnetic field B points in z-direction.

a good quantum number. Substituting this into the Hamiltonian, we get:

$$H = \frac{1}{2m^*}\left[p_x^2 + (\hbar k_y + eBx)^2\right] \tag{1.4}$$

This can be rewritten as:

$$H = \frac{p_x^2}{2m^*} + \frac{1}{2}m^*\omega_c^2(x - x_0)^2 \tag{1.5}$$

where $\omega_c = eB/m^*$ is the cyclotron frequency and $x_0 = -(\hbar k_y)/(eB)$ is the center of the harmonic oscillator. This Hamiltonian describes a one-dimensional harmonic oscillator centered at x_0 with frequency ω_c. The energy eigenvalues of a 1D harmonic oscillator are quantized and given by:

$$E_n = \hbar\omega_c\left(n + \frac{1}{2}\right), \qquad n = 0, 1, 2, ... \tag{1.6}$$

Such quantized energy levels are called Landau levels (LL). Each Landau level is highly degenerate thus for a sample of area L_xL_y, the degeneracy of each Landau level is given by $N = eBL_xL_y/h = \Phi/\Phi_0$, where $\Phi = BL_xL_y$ is the total magnetic flux through the sample

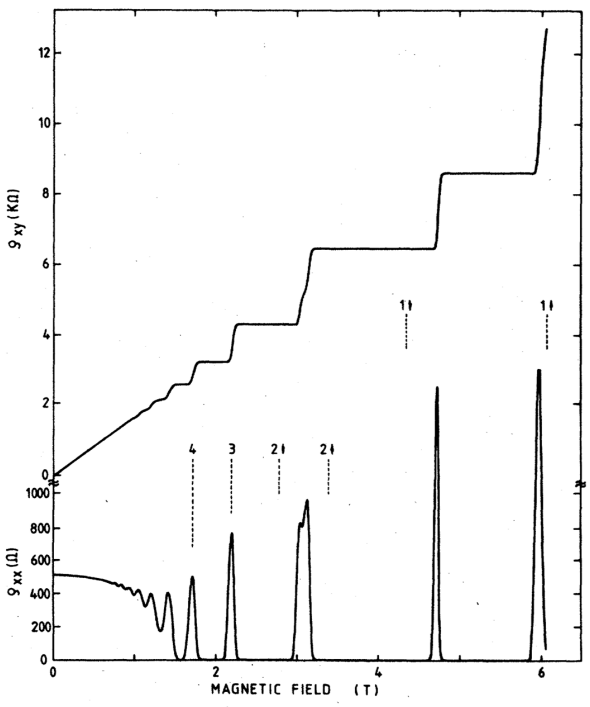

Figure 1.2: Experimental result adopted from Ref. [1], depicts the Hall resistivity as the function of perpendicular magnetic field. The plot shows the famous quantized Hall resistivity plateaus.

and $\Phi_0 = h/e$ is the magnetic flux quantum. We can now incorporate the effect of a weak electric field $\mathbf{E} = E_x\hat{x}$ applied perpendicular to the magnetic field. The Hamiltonian now becomes:

$$H = \frac{1}{2m^*}(\mathbf{p} + e\mathbf{A})^2 + eE_x x \tag{1.7}$$

In the Landau gauge $\mathbf{A} = (0, Bx, 0)$, this is:

$$H = \frac{1}{2m^*}\left[p_x^2 + (p_y + eBx)^2\right] + eE_x x \tag{1.8}$$

The electric field introduces a drift velocity for the center of the Landau orbits. The energy of the Landau levels is shifted by the electric field. For a given nth LL, the energy becomes:

$$E_{n,k_y} = \hbar\omega_c\left(n + \frac{1}{2}\right) + eE_x\left(x_0 - \frac{eE_x}{m^*\omega_c^2}\right) + \frac{m^*}{2}\frac{E_x^2}{B^2} \tag{1.9}$$

$$= \hbar\omega_c\left(n + \frac{1}{2}\right) - eE_x k_y\left(\frac{\hbar}{eB}\right) - \frac{m^*}{2}\frac{E_x^2}{B^2} \tag{1.10}$$

$$= \hbar\omega_c\left(n + \frac{1}{2}\right) - \hbar k_y v_D - \frac{m^*}{2}\frac{E_x^2}{B^2} \tag{1.11}$$

where $x_0 - eE_x/(m^*\omega_c^2)$ is the x-coordinate corresponding to the center of the orbit (related to k_y in a different gauge), and $v_D = E_x/B$ is the drift velocity in the x-direction. Consider a situation where the Fermi level lies within the gap between two Landau levels. If ν LLs are completely filled, the total number of electrons is $N_{tot} = \nu(eBL_xL_y/h)$. When an electric field E_x is applied, these filled Landau levels contribute to the Hall current. The current density in the y-direction (J_y) is given by the product of the electron density, charge, and drift velocity:

$$J_y = n(-e)v_D = -e\,n\,\frac{E_x}{B} \tag{1.12}$$

where $n = N_{tot}/(L_xL_y) = \nu eB/h$ is the electron density. Substituting this into the expression for J_y:

$$J_y = \left(\nu\frac{eB}{h}\right)(-e)\frac{E_x}{B} = -\nu\frac{e^2}{h}E_y \tag{1.13}$$

The Hall current I_y flowing in the y-direction (perpendicular to the applied electric field) is $I_y = J_yL_y$. The Hall voltage V_y is related to the electric field by $V_y = E_yL_y$. The Hall conductance σ_{xy} is defined as the ratio of the Hall current density to the applied electric field

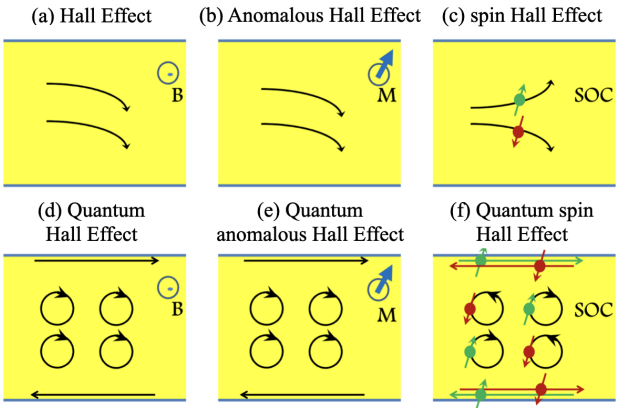

Figure 1.3: Schematic depicts the emergence of states around the edge stemming from the Landau orbits. (a) Show the classical picture and (b) portrays the QHE in quantum mechanical regime in presence of external magnetic feild B. The second column however is for magnetized materials in (b) classical and (e) quantum mechanical regime. Finally, the effect of spin-orbit coupling (SOC) is shown in last column (c) and (f). Adopted from Ref. [16].

in the y-direction (or equivalently, the ratio of the current in the y-direction to the voltage in the x-direction)

$$\sigma_{xy} = \frac{J_y}{E_x} = -\nu\frac{e^2}{h} \tag{1.14}$$

Conventionally, the Hall conductance is defined with the current and voltage directions consistent with a positive charge carrier under the Lorentz force. If we consider the current flowing along the y-direction due to an electric field in the y-direction and the resulting voltage in the x-direction, or vice versa, the magnitude remains the same. Therefore, the absolute value of the Hall conductance is

$$|\sigma_{xy}| = \nu\frac{e^2}{h} \tag{1.15}$$

This leads exactly to the resistance plateau we see in Fig. 1.2. The plateaus in the Hall resistance observed experimentally occur at these quantized values, demonstrating the remarkable precision of the IQHE. The single-particle picture of electrons occupying quantized Landau levels provides a good description. However, at the extreme conditions with temperature in mk and a large magnetic field strength the Hall conductance plateaus appear at fractional multiples of e^2/h, such as $1/3$, $2/5$, $3/7$, ... [8, 14, 15]. The emergence of fractionalised plateaus has been termed as Fractional Quantum Hall Effect (FQHE). The key distinction between the IQHE and the FQHE lies in the dominant role of electron-electron interactions in the latter. These strong interactions drive the system into novel correlated quantum states that cannot be understood by considering individual electrons alone.

The above provides a basic understanding of the quantization based on LL. A more complete picture requires considering the role of edge states, which are crucial for the robustness of the quantized conductance against impurities and disorder. In a real sample with edges, the Landau levels bend near the boundaries, giving rise to 1D chiral edge states that propagate without backscattering as shown in Fig. 1.3(d). These edge states carry the current and are responsible for the unhindered transport observed in the IQHE. The number of these edge channels corresponds to the integer filling factor ν, providing an alternative and more robust explanation for the quantization of the Hall conductance. It was in 1982 that Thouless *et al.,* [3] presented this explanation, and the filling factor ν was termed as TKNN invariant named after Thouless, Kohmoto, Nightingale, and Nijs. It was later showed by M. Kohomoto [17] that TKNN invariant is the Chern number of a 2D topological system with a broken time reversal symmetry. The topological interpretation based on the Chern number further reinforces the understanding of the IQHE as a topologically protected phenomenon, hence weaving, topological phenomenon with condensed matter physics. The IQHE requires a strong external magnetic field, which explicitly breaks time-reversal symmetry.

The search for a system with topological properties without an explicit dependence on external magnetic field led to topological insulators. Kane and Mele in 2005 [5] proposed spin quantum Hall insulators (with Quantum Spin Hall effect) which preserved time reversal symmetry of the electronic states. These insulators had a bulk electronic band gap and supported the transport of spin and charge by gapless edge modes as shown in Fig. 1.3(f). They also showed that the topological invariant of such insulators relies upon a $\mathbb{Z}_2$ invariant. The simplest forms of topological insulators preserve time-reversal symmetry and do not require an external magnetic field for the existence of their protected surface states. The topological order in these materials originates from the intrinsic band structure modified by spin-orbit coupling. The first experimental realization of a 2D topological insulator exhibiting the Quantum spin Hall (QSH) effect came in 2007 [18]. They demonstrated the existence of robust edge states in HgTe/CdTe quantum wells with a specific thickness, confirming the theoretical predictions. Since then the field has seen a rapid development on theoretical and experimental fronts.

1.1.2 Edge states of Bulk Topological materials

Topological edge modes are a class of electronic states that exist robustly at the boundaries or interfaces of materials with non-trivial topological properties, meaning their existence is guaranteed by the fundamental symmetries and band structure topology of the bulk mate-

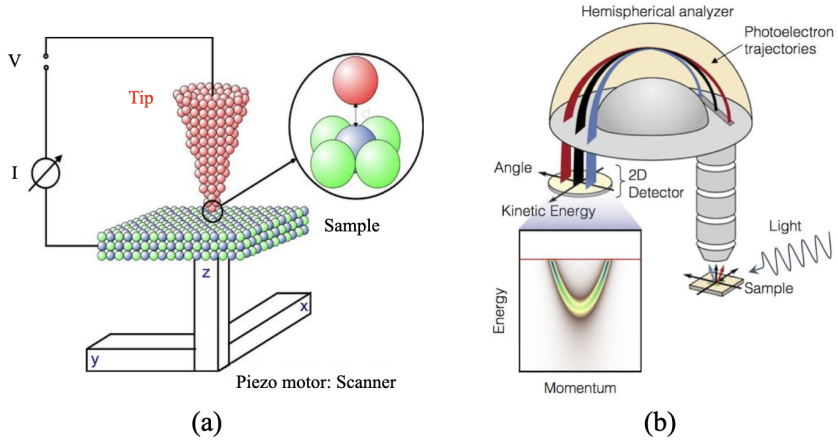

Figure 1.4: Schematic (a) shows the components of STM, with a sharp tip which scans across the sample measuring slight change in the conductance. (b) Illustrates how light produces photoelectron across the sample. The hemispherical analyzer then resolves these beams of photoelectron using the an internal electric field. These resulting beams is used to make a map of intensity corresponding to a planar cross-section in momentum space. Adopted from Refs. [19] and [20], respectively.

rial. This makes them inherently robust against various forms of disorder and imperfections, unlike conventional electronic states. Real-space imaging via scanning tunneling microscopy (STM) has proven particularly revealing in directly visualizing these states.

STM is a powerful analysis technique that allows for atomic scale imaging of conductive surfaces by scanning with a sharp metallic tip across the sample and measuring the tunneling current that flows between the tip and the surface as shown in Fig. 1.4(a). This current is exquisitely sensitive to the local electronic structure. The differential conductance which essentially plots the local electronic density of states as a function of position by measuring the (differential conductance) derivative of current with respect to voltage (dI/dV) - clearly resolved 1D edge channels. These channels exhibited distinctive spatial decay profiles, showing an enhanced local density of states (LDOS), a measure of available electronic states at a specific energy and position, that persisted within (approximately 2 nm) the sample edge before smoothly merging with the bulk states. These measurements provided the first direct visualization of how topological protection manifests at atomic scales. Topological protection refers to the inherent robustness of these states against perturbations that do not break the underlying symmetries, ensuring their coherence and preventing back-scattering. Crucially, the edge states remain coherent even in the presence of non-magnetic defects, which would typically localize or scatter conventional electronic states, highlighting their remarkable resilience.

Complementary angle-resolved photoemission spectroscopy (ARPES) studies have elu-

cidated the intricate electronic structure underlying these edge modes. ARPES is a spectroscopic technique that directly probes the energy and momentum of electrons within a material, providing a "band structure map" of the electronic states. By analyzing the kinetic energy and emission angle of photoemitted electrons [c.f. Fig. 1.4(b)], ARPES can reveal how electron energy varies with momentum, which is crucial for understanding material properties as shown in inset of Fig. 1.4(b). The landmark doped Bi_2Se_3 measurements by Hsieh et al. [21] (c.f. Fig. 1.5) revealed not just the characteristic Dirac cone dispersion of surface states, but crucially showed these states crossing the bulk band gap without hybridization. A Dirac cone describes a unique linear relationship between an electron's energy and its mo-

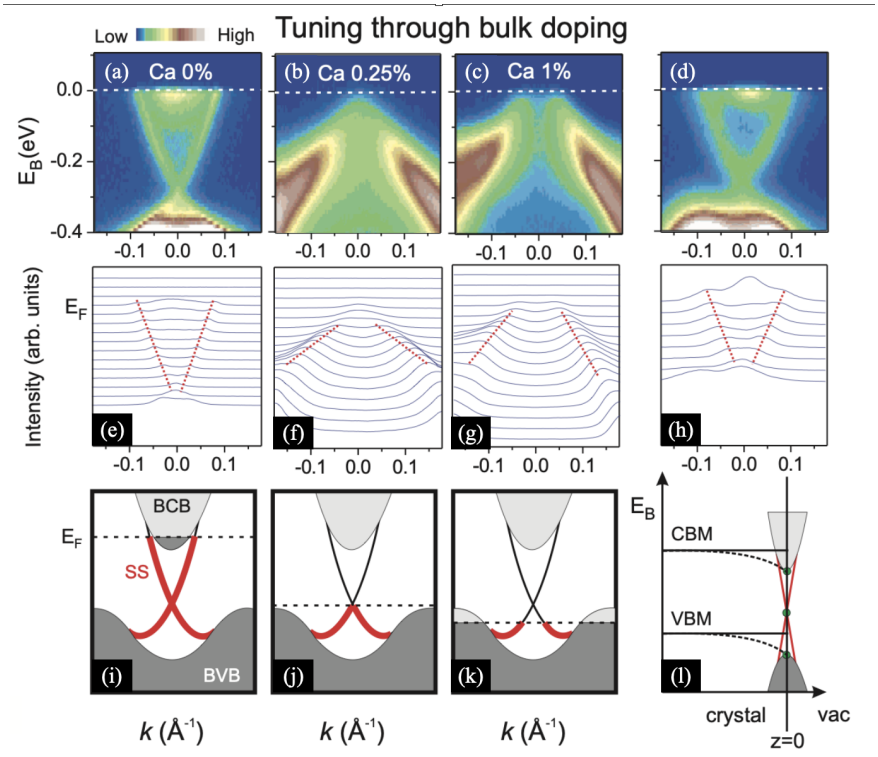

Figure 1.5: (a)-(d) are the ARPES result for $Bi_{2-\delta}Ca_\delta Se_3$ for different doping of Ca across (a)-(c). (e)-(g) Shows the momentum distribution curves corresponding to (a)-(c), red dashed line is the guide to eye. (i)-(k) Shows the bulk conduction band and bulk valance band in dark while the surface states are shown in red. The downwards shift of Fermi energy with varying doping is clear. Whereas (d) is the ARPES result of a typical sample 18h after cleaving and (h) is the corresponding momentum distribution curves and (l) shows the surface states. The evolution of the conduction band minimum (CBM) and valance band maximum (VBM) over time in (l) called surface band bending. Adopted form Ref. [21].

mentum, resembling the energy-momentum dispersion of massless relativistic particles (like photons or neutrinos). In a material's electronic band structure, a Dirac cone appears as two cone-shaped bands (one for valence electrons and one for conduction electrons) that meet at a single point, known as the Dirac point. At this point, the electrons effectively behave as massless Dirac fermions, leading to high mobility and unique transport properties. Further-

more, the spin-resolved ARPES data provided the smoking gun evidence for spin-momentum locking, a key characteristic of topological insulators where the spin direction of an electron is uniquely coupled to its momentum direction. The absence of hybridization means these edge states maintain their distinct identity and do not mix with the bulk electronic states. This retention of separate identity leads to separation between edge and bulk states, later quantitatively confirmed in WTe_2 monolayers by Wu *et. al* [22], explains why edge conduction can dominate overall transport even when substantial bulk carriers are present. This was demonstrated by showing opposing spin polarizations ($\pm\hbar/2$, where $\hbar$ is the reduced Planck constant) for the two branches of the Dirac cone, meaning electrons moving in opposite directions have opposite spins.

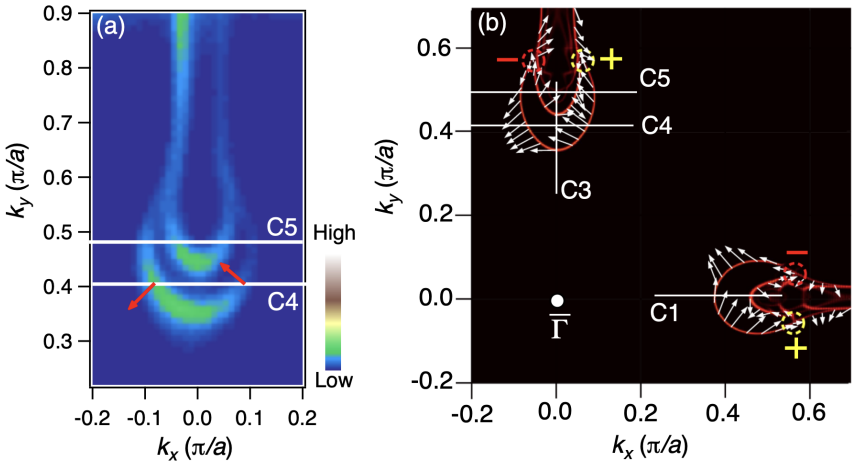

Figure 1.6: Spin polarised Fermi surface texture for the crystal of TaAs using (a) spin resolved ARPES along $\Gamma - Y$. The direction of the red arrow points in the direction of in-plane spin polarization. (b) The calculated Fermi surface texture with arrow point in the direction in-plane spin polarization. Adopted from Ref. [23].

Fermi arcs represent one of the most striking manifestations of topology in quantum materials. Unlike conventional metals where Fermi surfaces form closed loops in momentum space, these open contours directly connect topologically protected Weyl (massless Dirac fermions) or Dirac nodes, creating a new paradigm for electronic structure. The experimental verification of Fermi arcs has relied on sophisticated spectroscopic and transport techniques that reveal their unique properties. ARPES has provided the most direct visualization of these unusual states. In the seminal work on TaAs by Lv *et. al* [24], the ARPES intensity maps clearly showed open-ended Fermi contours bridging pairs of Weyl nodes projected to the surface Brillouin zone. These arcs as shown in Fig. 1.6 exhibited several remarkable features like their length precisely matched the separation between bulk Weyl nodes in momentum space, their spectral weight remained intense right up to the termination points, and they

persisted across multiple cleavage planes. The transport signatures of Fermi arcs are equally distinctive.

The chiral anomaly, first observed in TaP through negative magnetoresistance measurements as shown in Fig. 1.7, occurs when parallel electric and magnetic fields creates population imbalance between Weyl cones of opposite chirality. The quadratic field dependence of conductivity ($\Delta\sigma \propto B^2$) and its strict orientation requirements provide an unambiguous fingerprint of this topological phenomenon.

Quantum oscillation measurements in Cd_3As_2 revealed complementary evidence through the coexistence of two distinct frequencies. A higher frequency corresponding to bulk Dirac states and a lower frequency originating from Fermi arc surface states. The angular dependence of these oscillations mapped out the predicted "bowtie" shaped orbits formed by arc-connected Weyl nodes. More recent experiments have uncovered even richer behavior in

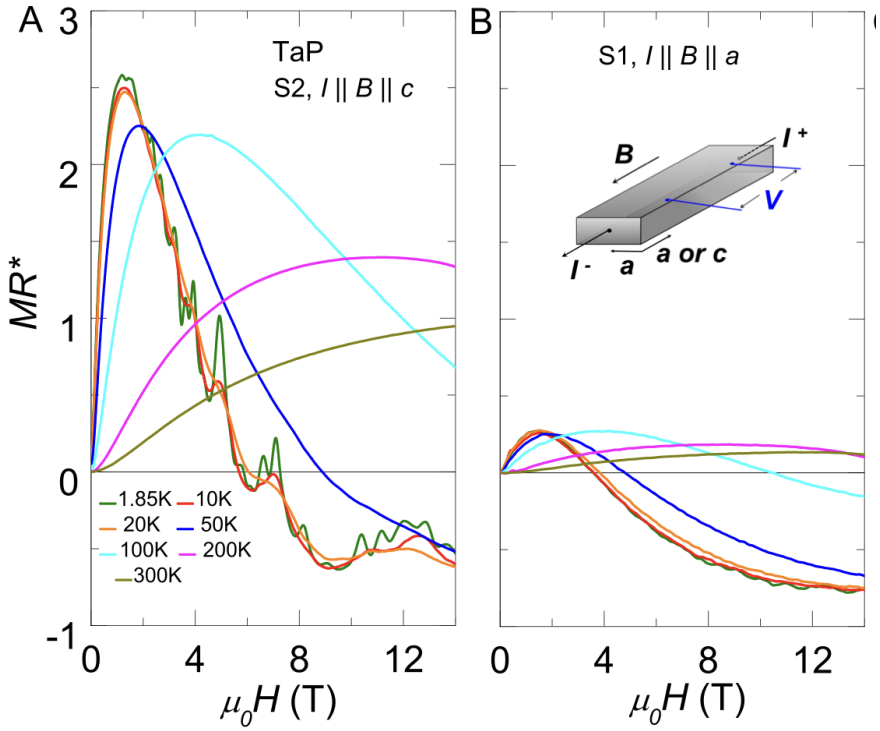

Figure 1.7: Longitudinal magnetoresistance for TaP at multiple different temperature. The measurement is made with the configuration where (A) $I||B||c$ and (B) $I||B||a$, the inset shows the schematic of the experimental setup. Adopted from Ref. [25].

these systems. In type-II Weyl semimetal WTe_2, STM [26, 27] is used to visualize the real-space structure of Fermi arc states through quasiparticle interference patterns (QPI) [28]. When electrons scatter off defects, they create a ripple-like standing wave pattern that STM can detect, serving as a real-space map of the electronic states. By using a Fourier transform to analyze these QPI patterns, scientists can move from a real-space picture to a momentum-

space map, revealing the material's electronic band structure. The key discovery in WTe_2 was the presence of "missing scattering vectors" in the Fourier transform, which directly proves that the electrons on its surface Fermi arcs are spin-polarized. This unique property, known as spin-momentum locking, means that an electron's spin is inextricably linked to its direction of motion, a hallmark feature of a topological state of matter (as shown in Fig. 1.6). Meanwhile, nonlocal transport measurements demonstrated that Fermi arcs can mediate electrical currents over micrometer-scale distances, with the signal persisting to higher temperatures than bulk conduction.

The unique connectivity of Fermi arcs leads to several fundamental consequences. First, they enable new forms of electron orbits in magnetic fields that combine bulk and surface trajectories. Second, their spin-momentum locking creates protected conduction channels that are robust against backscattering. Third, their termination at Weyl nodes means they can mediate transitions between bulk states of opposite chirality. These properties have been quantitatively verified through the combination of ARPES, quantum oscillations, and magnetotransport experiments across multiple material systems.

Transport measurements have quantified the remarkable robustness and unique conductive properties of these edge states. The measurement of quantum spin Hall effect in HgTe quantum wells [18] provided compelling evidence. The quantum spin Hall effect is a topological phase of matter characterized by the presence of spin-polarized edge currents that flow without dissipation in the absence of a magnetic field as shown in Fig. 1.3(f). The experiments showed a $2e^2/h$ conductance plateau. This plateau persists and shows independence from the sample width pointing to it being the edge modes. This width directly corresponds to the bulk bandgap, unequivocally confirming that transport occurs exclusively through in gap edge channels, meaning the conduction pathways exist within the energy gap of the bulk material. Later quantum anomalous Hall experiments [29] achieved even more striking results [c.f. Fig. 1.3(e)]. The quantum anomalous Hall effect is a topological phase where an intrinsic magnetic order leads to quantized Hall conductance even without an external magnetic field, unlike the conventional quantum Hall effect. In these experiments, the Hall resistance was quantized to h/e^2. These exceptionally low resistance values, maintained over millimeter-scale distances, powerfully demonstrate the true dissipationless nature of chiral edge modes, which are one-way conducting channels that are immune to backscattering.

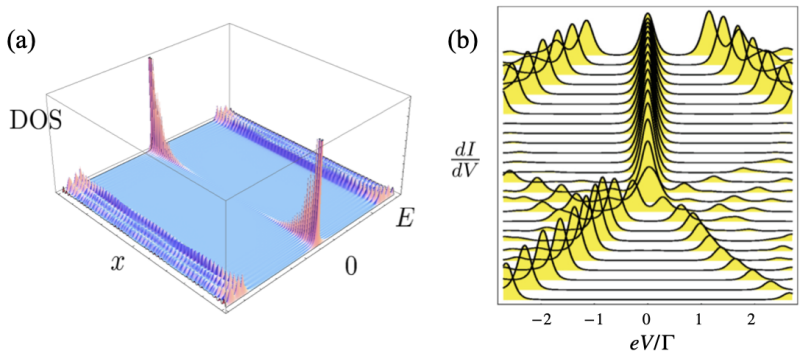

Figure 1.8: (a) Local density of states of a nanowire with proximity induced superconductivity. It shows the presence of superconducting gap along with Majorana zero modes localised at $E = 0$ at the ends of the nanowire. (b) The differential conductance as the function of applied voltage across the ends of the wire. While each line corresponds to a different value of external in-plane magnetic field. The peak for the zero bias voltage appears for a critical value of magnetic field marking the emergence of Majorana zero modes. Adopted from Ref. [30].

1.1.3 Edge modes of 1D topological materials

The combination of the advanced experimental techniques and theoretical understanding has revealed a nuanced hierarchy of protection in topological edge states. While all topological edge states are inherently immune to backscattering from non-magnetic disorder, as shown by STM, only systems where time reversal symmetry is broken (e.g., in quantum anomalous Hall systems) show complete suppression of dissipation, as confirmed by the ultra low longitudinal resistance in transport data. Time reversal symmetry dictates that the laws of physics are the same whether time flows forward or backward; breaking this symmetry can lead to unique transport phenomena. This distinction becomes crucial when considering advanced applications, particularly in quantum computing, where the stricter protection and inherent chirality of chiral Majorana modes. Exotic quasiparticles that are their own antiparticles and are predicted to exist at the edges of certain topological superconductors. These modes constitute half of an ordinary electron, appearing as zero-energy excitations bound to defects or edges that obey non-Abelian statistics, a mathematical property allowing quantum operations through braiding in space rather than conventional gate manipulations. Their potential for topological quantum computation stems from this inherent protection against local decoherence mechanisms, offering a path toward fault-tolerant quantum computing. The pursuit of chiral Majorana edge modes represents a fundamental quest in quantum materials physics, where the exotic quasiparticles emerging in topological superconductors (TSCs) could revolutionize quantum information science.

Majorana modes emerge as solutions to the Bogoliubov-de Gennes equations in systems

exhibiting a confluence of specific physical conditions. These conditions typically include p-wave pairing symmetry, which can be either intrinsic to the material or proximity-induced from an adjacent conventional superconductor, strong spin-orbit coupling, which links an electron's spin to its momentum, and time-reversal symmetry breaking, often achieved through an applied magnetic field or intrinsic magnetism. When these criteria are met, they collectively create a topological superconducting gap that hosts protected edge states, whose behavior can be described by theoretical models such as the Kitaev chain [4]. A key signature of these modes is the emergence of zero-energy excitations at the system boundaries [c.f. Fig. 1.8(a)], with wavefunctions satisfying the unique Majorana condition $\gamma = \gamma^\dagger$, signifying that these quasiparticles are their own antiparticles. In 2D systems, these zero-energy modes manifest as chiral edge currents, circulating either clockwise or counterclockwise depending on the direction of the applied magnetic field.

Compelling experimental evidence for Majorana modes has primarily emerged from two distinct material classes: intrinsic topological superconductors and hybrid nanostructures. In the realm of intrinsic topological superconductors, the iron-based superconductor $FeTe_{0.55}Se_{0.45}$ has garnered significant attention due to its inherent properties that fulfill all the theoretical requirements. This material exhibits a bulk superconducting gap ($\Delta \approx 1.8$ meV) and possesses topological surface states. STM studies like [31], have provided telltale signatures of Majorana modes. Specifically, these experiments revealed quantized $2e^2/h$ zero bias peaks at the cores of magnetic vortices, indicating the presence of zero-energy states. These peaks were characterized by strict spatial localization, typically less than 3 nm, and a notable absence of other states at finite energies within the superconducting gap, a characteristic expected for isolated Majorana bound states. In parallel, hybrid nanostructures have offered a highly tunable platform for the exploration of Majorana physics. Semiconductor nanowires, particularly those made of InSb and proximity-coupled to conventional superconductors, have demonstrated the ability to host these exotic excitations.

A primary experimental signature for the existence of Majorana zero modes (MZMs), is the zero-bias peak observed in tunneling spectroscopy [c.f. Fig. 1.8(b)]. This measurement is typically performed on a hybrid device, such as a semiconductor nanowire coupled to a superconductor, where a normal metal lead probes the local density of states. The differntial conductance (dI/dV) is measured as a function of voltage. A sharp peak at zero voltage indicates the presence of a state precisely at zero energy, the MZM. While this zero-bias peak is a crucial piece of evidence, its identity is muddled by the fact that similar peaks can arise from topologically trivial effects, such as accidental zero-energy Andreev bound states or

disorder. Consequently, additional confirming characteristics, including the peak's robustness against magnetic fields and its quantized height are required, to distinguish a true MZM from a trivial one. Transport measurements on these systems [12], have yielded significant insights. These studies showed the appearance of half-quantized $e^2/2h$ conductance plateaus, a hallmark signature predicted for Majorana zero modes, which remained robust against variations in external parameters such as gate voltage and magnetic field.

The most definitive proofs of Majorana modes, particularly their unique quantum properties, have come from phase-sensitive experiments. A prime example is the observation of the 4π-periodic Josephson effect, which directly demonstrates the parity-switching nature of Majorana states [32]. This phenomenon, contrasts with the conventional 2π periodicity of ordinary superconductors and provides strong evidence for the fractional charge of the carriers involved. Beyond this, experiments demonstrating nonlocal crossed Andreev reflection have further supported the concept of non-local fermion parity storage, where the quantum information encoded in Majorana pairs is distributed across spatially separated locations. While still in their nascent stages, recent braiding experiments are beginning to show preliminary signatures of non-Abelian statistics, which would be the ultimate confirmation of their utility for fault-tolerant quantum computation.

The emergence of distinct topological phases of matter, exemplified by IQHE and QSH effect, necessitates a systematic framework for their classification. While both phenomena exhibit protected conducting states at their boundaries despite a bulk insulating gap, the underlying physical mechanisms and the symmetries at play differ significantly. This calls for a classification scheme that organizes these phases based on fundamental symmetries of the Hamiltonian. The "Tenfold Way" provides such a classification for non-interacting fermionic systems.

1.2 Classification of topological materials

The tenfold classification is also called Cartan classes because the classification scheme originated from the work of mathematician Élie Cartan. His work on Lie groups, symmetric spaces, and their algebraic structures laid the foundation for the classification of gapped quantum systems. Specifically, the tenfold way is a direct application of his classification of symmetric spaces, which themselves are based on the properties of Lie algebras. Cartan showed that these geometric spaces could be organized into a finite number of classes based on their algebraic and topological properties. Decades later, Alexander Altland and Martin Zirnbauer in the field of random matrix theory, which they applied to mesoscopic systems

and disordered superconductors led to the modern tenfold classification [33]. This is of course accomplished by identifying the symmetries of the Hamiltonian which describes the system. Based upon these symmetries, the Hamiltonian exhibits topological invariant. Calculation of the topological invariant hinges upon the representation of the Hamiltonian. A symmetry of a Hamiltonian H is a transformation that leaves the Hamiltonian invariant. For a unitary symmetry, this transformation is represented by a unitary operator U. The defining property of such a symmetry is that it commutes with the Hamiltonian:

$$U\,H\,U^{\dagger} = H\,, \tag{1.16}$$

$$U\,H = H\,U\,, \tag{1.17}$$

since $U^{-1} = U^{\dagger}$. This commutation relation allows the symmetries to lead to a block diagonal representation of the Hamiltonian (as we demonstrate below). The mathematical consequence of two operators commuting, especially a Hermitian operator like H and a unitary operator like U, is that they can be simultaneously diagonalized. This means there exists a common basis of eigenstates for both H and U. Let's consider the eigen spectrum of H namely $|\psi_n\rangle$, hence

$$H|\psi_n\rangle = E_n|\psi_n\rangle\,. \tag{1.18}$$

Now the application of the unitary operator leads to

$$U\,H|\psi_n\rangle = U\,E_n|\psi_n\rangle\,, \tag{1.19}$$

$$H\,U|\psi_n\rangle = E_n\,U|\psi_n\rangle\,. \tag{1.20}$$

This quite obviously implies that if the Hamiltonian has an energy eigenstates $|\psi_n\rangle$ with energy E_n then, $U|\psi_n\rangle$ is also an eigenstate with energy E_n. There are two possible scenarios based on the degeneracy of the energy eigenstates of the Hamiltonian. If E_n is a non-degenerate eigenvalue, meaning $|\psi_n\rangle$ is the unique eigenstates (up to a phase) corresponding to E_n, then $U|\psi_n\rangle$ must be proportional to $|\psi_n\rangle$. That is, $U|\psi_n\rangle = \lambda|\psi_n\rangle$. Since U is unitary matrix its eigenvalues must be of unit magnitude, implying $\lambda = e^{\imath\phi}$ for some phase ϕ. Hence implying that U and H share the eigenstate. On the other hand, if E_n is degenerate, there exists an eigen subspace of states $(|\psi_{n1}\rangle, |\psi_{n2}\rangle, |\psi_{n3}\rangle, \cdots, |\psi_{nk}\rangle)$ which share the eigenstate with energy E_n. In this case, U maps states within the $k-$dimensional subspace with each other. It is always possible to form a new orthonormal basis for the degenerate subspace such

that U is diagonal in this new basis. Consequently, we can find a basis of eigenstate of H that are simultaneous eigenstates of U. The above leads us to conclude that the Hamiltonian can be diagonalised alongwith the unitary matrix U. Chossing an orthonormal basis for U implies that the Hamiltonian can be represented as follows

$$H = \begin{pmatrix} H_1 & 0 & 0 & \cdots \\ 0 & H_2 & 0 & \cdots \\ \vdots & \vdots & \ddots & \vdots \\ 0 & 0 & \cdots & H_m \end{pmatrix} \tag{1.21}$$

here m is the number of unique and distinct eigenvalues of U given by $e^{\imath\phi_1}$, $e^{\imath\phi_2}$, $\cdots e^{\imath\phi_m}$. The orthonormal choice of basis which makes the representation of U diagonal will allow us to block diagonalize H as given above. This can be extended to all set of unitary operators representing the symmetries of the system leaving us with a final block diagonal Hamiltonian.

This block diagonalization effectively decomposes the entire system into independent, non-interacting subsystems. Instead of characterizing the topology of the full system described by H, the problem is reduced to classifying the topology of each individual block H_j. Unitary symmetries, by their very nature of commuting with the Hamiltonian, impose conservation laws. These conservation laws merely partition the Hilbert space. They do not introduce additional structural constraints within each irreducible block that would alter its inherent topological nature. The topological properties of the entire system are then simply the aggregate of the topological properties of its constituent, decoupled blocks. This is akin to analyzing a composite system by studying its independent components; no fundamentally new physics or constraints arise from their mere aggregation.

The classification is determined by most generic symmetries namely, particle-hole/charge conjugation (PHS) $\mathcal{P}$, time reversal (TRS) $\mathcal{T}$, and chiral symmetry (CS) $\mathcal{C} \propto \mathcal{P}\,\mathcal{T}$. They form the fundamental discrete symmetry of a quantum mechanical system and consequently condensed matter physics. It is crucial to realize that the both $\mathcal{T}$ and $\mathcal{P}$ are inherently anti-unitary and $\mathcal{C}$ is a unitary operator. Let's discuss each of these symmetries in detail, starting with $\mathcal{T}$. The second quantised Hamiltonian when acted upon by $\mathcal{T}$ is considered to time-reversal invariant if and only if

$$\mathcal{T}^{-1} H \mathcal{T} = H \tag{1.22}$$

It follows from Wigner's theorem which extends to condensed matter systems that the time

reversal operator is represented by anti-unitary operator. This anti-unitary operator can be written as $\mathcal{T} = U_T \mathcal{K}$, here U_T is a unitary operator and $\mathcal{K}$ is the complex conjugation operator. The time reversal operator comes in two flavors given the Hamiltonian is time reversal invariant which is particularly captured by $\mathcal{T}^2$ which itself is a unitary. We can summarize the different possibilities as follows

$$T = \begin{cases} 0 & \text{Hamiltonian is not time reversal invariant} \\ +1 & \text{Hamiltonian is time reversal invariant and } \mathcal{T}^2 = 1 \\ -1 & \text{Hamiltonian is time reversal invariant and } \mathcal{T}^2 = -1 \end{cases} \tag{1.23}$$

here we use T as a short hand to describe the different possibilities. It is well known that $\mathcal{T}^2 = 1$ describes the systems which are bosonic or with integer spin. On the other hand, $\mathcal{T}^2 = -1$ describes the fermionic system with half-integer spins. This also leads to the Kramers degeneracy which demands two-fold degeneracy for every eigenstate of the system. The above impose different conditions on the structure of the block-diagonal Hamiltonian hence segregating different classes of systems from each other. The particle-hole symmetry is another symmetry which plays a classifying role for the block-diagonal Hamiltonian similar to the time reversal symmetry. The Hamiltonian is said to be invariant under particle-hole symmetry if

$$\mathcal{P}^{-1} H \mathcal{P} = -H \tag{1.24}$$

the minus sign ensures that for a given eigenstate with energy E there exists another state with energy $-E$. Particle-hole symmetry similar to time reversal symmetry has an antiunitary representation. This allows particle-hole symmetry to have its own classification of Hamiltonian

$$P = \begin{cases} 0 & \text{Hamiltonian is not particle-hole invariant} \\ +1 & \text{Hamiltonian is particle-hole invariant and } \mathcal{P}^2 = 1 \\ -1 & \text{Hamiltonian is particle-hole invariant and } \mathcal{P}^2 = -1 \end{cases} \tag{1.25}$$

The classification would constitute of total $3 \times 3 = 9$ classes but there happens to exist one more class of symmetry namely, chiral symmetry which demands a chiral invariant Hamiltonian to follow

$$\mathcal{C}^{-1} H \mathcal{C} = -H \tag{1.26}$$

Chiral symmetry $\mathcal{C}$ which is not independent of particle-hole and time reversal symmetry (if they are present). Chiral symmetry is given by composition of the other two hence $\mathcal{C} = \mathcal{P} \cdot \mathcal{T}$. This implies that absence of one of $\mathcal{P}$ or $\mathcal{T}$, leads to absence of $\mathcal{C}$. It is important to note that as $\mathcal{C}$ is a product of two anti-unitary representations, making it unitary. Contrary to the other two symmetries, $\mathcal{C}$ is either absent or present due to its unitary nature. The classes of classification based on $\mathcal{P}$, and $\mathcal{T}$ were 9 with one of them being the absence of both, this possibility now gets altered due to the $\mathcal{C}$ which has 2 different possibility hence the total classes are $3 \times 3 - 1 + 2 = 10$. All these 10 possibilities are listed in the Tab. 1.1.

The classification shown in Tab. 1.1 lists different set of values the topological invariants can acquire for different symmetry classes. The entry '0' for a certain class signifies its trivial topological nature or absence of an invariant. These systems being topologically trivial are equivalent from this perspective. The entry $\mathbb{Z}$ stands for the set of integers and hence such systems will have a topological invariant which can take any value from set of integers. Tab. 1.1 also shows example of such system, which happens to quantum Hall effect.

$2\,\mathbb{Z}$ implies that the topological invariant will be an even integer. A quantum dot with spinfull time reversal symmetry is an example of such a system. The Kramer's degeneracy restricts the number of filled energy levels to be even. Lastly, $\mathbb{Z}_2$ is the set of $\{-1, 1\}$ which results in topological phase of only two kind. Topological invariant for a nanowire is a $\mathbb{Z}_2$ invariant. Another example is a 3D topological insulator with protected time reversal symmetry.

W have set the stage with a broad overview of the current experimental landscape in condensed matter physics. We began by introducing the QHE, demonstrating how the emergence of LLs leads to the quantization of conductance. This discussion then expanded to show how anomalous and spin quantum Hall effects are also rooted in the topological properties. We further explored how 1D topological materials can host exotic edge modes, and we detailed the experimental techniques used for their detection. The unifying framework for all of these diverse phenomena is the tenfold classification, which serves as the scaffolding for this thesis.

1.3 Aim and scope of the thesis

Topological materials are crucial because their electronic properties are not determined by local symmetry but by a global topological invariant, making them remarkably robust against disorder and local imperfections [34, 35]. This principle manifests across different dimensions, leading to a variety of groundbreaking applications. In 1D systems, this protection allows

Class	TRS	PHS	CS	0D	1D	2D	3D	Example Systems
A	0	0	0	$\mathbb{Z}$	0	$\mathbb{Z}$	0	Quantum Hall systems
AI	+1	0	0	$\mathbb{Z}$	0	0	0	Spinless bosons
AII	−1	0	0	$2\mathbb{Z}$	0	$\mathbb{Z}_2$	$\mathbb{Z}_2$	Topological insulators
AIII	0	0	1	0	$\mathbb{Z}$	0	$\mathbb{Z}$	Systems like graphene
BDI	+1	+1	1	$\mathbb{Z}_2$	$\mathbb{Z}$	0	0	1D superconductors
C	0	−1	0	0	0	$2\mathbb{Z}$	0	Spin-singlet superconductors
CI	+1	−1	1	0	0	0	$2\mathbb{Z}$	Spin-symmetric superconductors
CII	−1	−1	1	0	$2\mathbb{Z}$	0	$\mathbb{Z}_2$	Quantum spin Hall systems
D	0	+1	0	$\mathbb{Z}_2$	$\mathbb{Z}_2$	$\mathbb{Z}$	0	Majorana fermions in superconductors
DIII	−1	+1	1	0	$\mathbb{Z}_2$	$\mathbb{Z}_2$	$\mathbb{Z}$	Helical Majorana edge states

Table 1.1: Cartan's classification of symmetry classes with topological invariants in various spatial dimensions of the boundary.

for the existence of exotic zero energy quasiparticles like Majorana bound states, which are promising candidates for building fault-tolerant topological quantum computers [36]. In 3D materials such as Weyl and Dirac semimetals, the bulk-boundary correspondence ensures that the gapped bulk hosts gapless, topologically protected surface states [24, 37]. These states, which can exhibit high electron mobility and unique spin properties, are being explored for next generation low power electronics, spintronics [38], and optoelectronics [39], representing a new frontier in materials science and technology.

The goal of this thesis is to explore topological properties of some solid state systems. In first case, we investigate system similar to the nanowire with the anitiferromagnetic order (the Chapter 3). In such type structure the topological properties are manifested by emergence of Majorana bound states. We present analyses of similar problem in the ladder with spin block chains. This study is motivated by the quasi-1D $BaFe_2S_3$, containing spin block ladders of Fe atoms. On the other hand, it is well known that the topological states can also arise in the

different type of interfaces. Current advancements in experimental techniques and theoretical understanding of topological behavior of such topological heterostructure have resulted in discovery of Dirac and Weyl semimetals. Naturally, the other center of attention in this thesis is a topological heterostructure or an interface of an insulator and Weyl semimetal with four nodal points (the Chapter 5). We focus on understanding the edge states of the interface, the spectral function and properties of such edge states. The thesis is organized such that Chapters 3 and 5 present the original results for investigated systems, while Chapters 2 and 4 present the extensive introductions.

In the chapters to come, we will dive deeper using the tight-binding framework to study topological properties. The Chapter 2 dedicated to 1D topological materials will introduce the notion of topological invariants using the key models like Su-Schrieffer-Heeger, Kitaev chain, e.t.c which have ended up forming the bedrock for the study of topological materials. The discussions will be directed towards introducing the rise to the edge modes like Majorana bound modes in these systems. Using the techniques developed in the Chapter 2 we will present the results of our study on a system of coupled nanowires to probe the topological phases and corresponding edge states of such a system in the Chapter 3. We will then revisit 2D and 3D topological materials in the Chapter 4 to review the source of their topological behavior. Focusing on band inversion in pioneering models of topological insulators like Kane-Mele model, Bernevig-Hughes-Zhang model, e.t.c, we will introduce the 3D Dirac and Weyl semimetals. Finally in the Chapter 5 employing our understanding of topological materials and heterostructures, we will show our results related to the investigation of an interface. More specifically, we will demonstrate the rich physical possibilities the continuum model of an interface holds. We will focus on the interface made up of an insulator and a topological material (Weyl semimetal), and analyze the nature of the edge states of the interface.

Chapter 2

1D topological materials

1D topological materials represent a fascinating frontier in condensed matter physics, hosting unique quantum states at their boundaries, namely at their ends [40–42]. Unlike conventional materials, these systems possess a topological invariant which remains unchanged even under external perturbation, deformations or disorder as long as the systems fundamental symmetries are preserved [43]. The topological invariant changes for the finite system at the ends leading to localized edge modes directly resulting from topological phase transition which are as robust as the topological invariant. These systems, often realized as nanowires [12] or assembled atomic chains [40], derive their topological properties from specific symmetries and interactions within their electronic structure. Nanowire(s) possess robust boundary states that are protected against local perturbations and disorder by the underlying topology of their bulk band structure, a phenomenon encapsulated by the bulk-boundary correspondence [44, 45]. The experimental exploration of these materials has unveiled novel phenomena, most notably the potential for hosting Majorana bound states (MBS), which are exotic quasiparticles that are their own antiparticles [46]. These non-Abelian anyons, localized at the ends of topological superconductors, hold profound implications for fundamental physics due to their unique exchange statistics and offer a promising avenue for fault-tolerant quantum technologies, as their non-local nature provides inherent protection against decoherence [47–49].

In this chapter we aim to introduce the fundamental theoretical tools required to quantify the topological invariant. Moreover, we will review the extensive literature from both theoretical and experimental front on the topological phases of nanowire with different properties and the edge modes they host. To provide a clear illustration of how symmetries can lead to non-trivial topological phases and protected boundary states, we will use the Su-Schrieffer-Heeger (SSH) model as a conceptual bridge in Sec. 2.1. We will shift our focus

from SSH model to Kitaev chain in Sec. 2.2, demonstrating the origin of MBS (Sec. 2.2.1) and discuss the modern theoretical tools like Bogoliubov–de Gennes equations used to study them (Sec. 2.2.2) along with the experimental possibilites of the realization of MBS. Finally, we explore the spinfull nanowire (Sec. 2.3) and their topological phases (Sec. 2.3.1) and the corresponding experiments on finite nanowire searching for MBS (Sec. 2.3.2)

2.1 Topology of SSH model

SSH model [50] offers a foundational understanding that can be extended to analyze more complex and experimentally relevant 1D topological materials. It stands as a cornerstone in the understanding of topological phases of matter, particularly in 1D. Originally proposed to describe the electronic properties of polyacetylene, a conjugated polymer characterized by alternating single and double bonds, it serves as an elegant and intuitive minimal model that captures the essential physics of topological insulators in 1D. Its simplicity lies in its ability to demonstrate the emergence of topological phases solely through the interplay of dimerization and sublattice symmetry, leading to distinct trivial and topological phases separated by a quantum phase transition. This model effectively bridges the gap between simplified theoretical constructs and more complex real materials, providing a pedagogical framework to grasp the core principles of topological protection and the existence of zero-energy edge states. The model describes a 1D chain of atoms or molecules with alternating hopping amplitudes. This staggered hopping creates two distinct sublattices, typically labeled A and B, within each unit cell. The physical system is characterized by two hopping parameters: the intra-cell hopping amplitude $t - \delta t$, and the inter-cell hopping amplitude $t + \delta t$. These alternating hopping(s) are responsible for the topological properties of the system. The Hamiltonian for the SSH model in real space can be written as

$$H = \sum_i \left[(t+\delta t)\, c^\dagger_{i,A} c_{i,B} + (t-\delta t)\, c^\dagger_{i+1,A} c_{i,B} \right] + \text{h.c.} \tag{2.1}$$

here $c^\dagger_{i,A}$ and $c^\dagger_{i,B}$ are creation operators for sublattices A and B in the ith unit cell, respectively. The term h.c. refers to the Hermitian conjugate, ensuring the Hamiltonian is Hermitian. For simplicity we have considered spinless electrons. In order to progress further we assume an infinite lattice sites with periodic boundary condition. This allows us to perform the Fourier transform of the operators and move to momentum space labeled by $\boldsymbol{k}$.

$$c^\dagger_{k,A} = \frac{1}{\sqrt{2\pi}} \sum_i e^{\imath \boldsymbol{k}\cdot\boldsymbol{a}_i} c^\dagger_{i,A} \tag{2.2}$$

here $\boldsymbol{a}_i$ is the lattice lattice vector. As the system is 1D, $\boldsymbol{a}_i = a\,\hat{\boldsymbol{n}}$ where, $\hat{\boldsymbol{n}}$ points in the direction of chain with a being the lattice constant. After substitution a summation furnishes the following Hamiltonian in momentum space

$$H(k) \;=\; \bar{d}(k)\cdot\bar{\sigma}\,, \tag{2.3}$$

$\bar{\sigma}$ is the Pauli's spin vector given as $(\sigma_0,\, \sigma_x,\, \sigma_y,\, \sigma_z)$. Along with

$$d_x \;=\; (t+\delta t) + (t-\delta t)\cos ka\,, \tag{2.4}$$

$$d_y \;=\; (t-\delta t)\sin ka\,, \tag{2.5}$$

$$d_z \;=\; 0\,. \tag{2.6}$$

Note that we have suppressed the momentum dependence on the component of vector $\bar{d}(k)$. Evidently, the Brillouin zone (BZ) for the system is of length $2\pi/a$ and thus $k \in (-\pi/a,\, \pi/a)$. Shifting our attention towards the symmetries of the Hamiltonian we note that $H(k)$ respects the following

- Time reversal symmetry $\mathcal{T}$: Given by an anti-unitary operator K satisfies $\mathcal{T}^\dagger H_k \mathcal{T} = H_{-k}$.
- Sublattice symmetry: The unitary operator given by $\mathcal{S} = \sigma_z$, anti-commutes with the Hamiltonian.
- The above permits an anti-commuting anti-unitary operator $\mathcal{C} = \mathcal{S}\mathcal{T}$.

This positions the SSH model in class A, AIII, AI, BDI and D. The choice of class is made based upon the additive terms we allow in the model. The energy spectra for the this system is given by

$$E_k \;=\; \pm\sqrt{d_x^2 + d_y^2} \tag{2.7}$$

and the corresponding energy eigenvectors are given by

$$|\pm\rangle \;=\; \begin{pmatrix} \pm\, e^{-\imath\phi} \\ 1 \end{pmatrix} \tag{2.8}$$

where $\tan\phi = d_y/d_x$. For a set of parameters t and δt, every momenta k in BZ has a corresponding eigenvector. This vector field is smooth and continuous as momentum changes. Consider that $\delta t < 0$, this makes it possible for the existence of a real momentum k_0 for which

$d_x = 0$. Hence, choice of $\delta t < 0$ leads to degeneracy of the energy eigenvalues in the BZ. As the momentum k changes the vector $\bar{d}$ loops around the origin [c.f. Fig. 2.1(b)]. This is called the winding number and it is the topological invariant for this system.

2.1.1 Edge states of SSH model

The chiral symmetry $\mathcal{C}$ anti-commutes with the Hamiltonian and hence maps states with positive energy to states with negative energy. As discussed previously there exist degenrate point in the spectra. The effects of such a degeneracy can be probed better with a low energy effective model. To construct such a model we first assume that $\delta t \ll t$ and we focus near the momentum where the degenerate point exists. The approximations enforce the degeneracy near $k = \pi/a + q$, here q is a small momentum about which we expand the Hamiltonian which gives us

$$H \quad = \quad 2\delta t\, \sigma_x + taq\, \sigma_y \tag{2.9}$$

redefining $2\delta t = m$ and $ta = v_F$ as done conventionally in literature. The energy spectrum

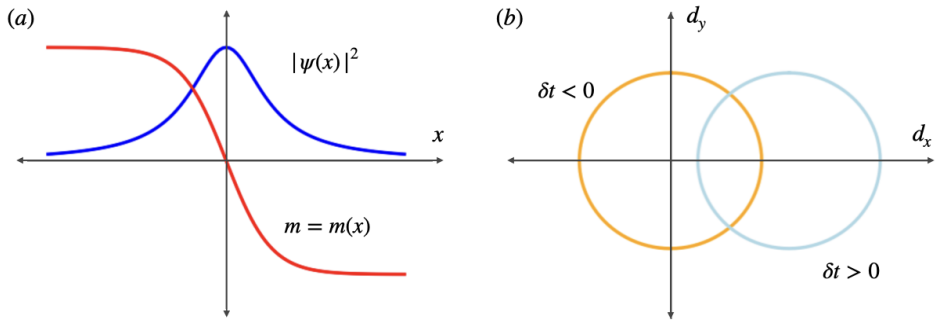

Figure 2.1: Schematic presents (a) the edge state superimposed with a spatially changing mass term of a general functional such that $m(x)$ changes monotonously changes sign from $x = -\infty$ to $x = \infty$. (b) The winding of components of Pauli basis for trivial ($\delta t > 0$) and non-trivial ($\delta t < 0$) topology.

is given by $E = \pm\sqrt{v_F^2 q^2 + m^2}$. To describe the zero mode we allow the m to spatially vary such that $m < 0$ when $x \to \infty$ and $m > 0$ when $x \to -\infty$. This spatial variation of m breaks the homogeneity of the continuum Hamiltonian. In effect producing an edge or a boundary in the system. We want the wave function for the zero mode hence we demand $H|u\rangle = 0$.

This os a first order partial differential equation and it can be resolve as following

$$(-iv_F\sigma_y\partial_x + m(x)\sigma_x)\psi(x) = 0 \tag{2.10}$$

$$\psi(x) = \exp\left(-\int_0^x m(x')/v_F\, dx'\right)|+\rangle \tag{2.11}$$

here $|\pm\rangle$ are the eigenvectors of σ_z with eigenvalue ± 1. Independent of the functional form of m the zero mode is a localized states near the boundary of the model [c.f. Fig. 2.1(a)]. Note that the chirality operator gives the partner state which has energy with opposite signature. The above result verifies the fundamental nature of topological insulators– Bulk boundary correspondence.

2.2 Superconducting nanowire

While the SSH model provides a foundational understanding of the connection between bulk topological invariants and protected edge states in insulators. Demonstrating how dimerization can lead to robust, localized electronic states at boundaries, superconducting systems host an even more exotic possibility namely, Majorana bound states (MBS). These elusive zero-energy quasiparticles emerge as Bogoliubov excitations in topological superconductors, where the inherent particle-hole symmetry, a fundamental characteristic of superconducting systems, plays a central and crucial role in their existence and protection.

To bridge the conceptual gap between the simpler SSH model and the more complex reality of topological superconductors hosting MBS, we introduce the Kitaev chain model. Proposed by Alexei Kitaev in 2001 [4], this 1D model of spinless fermions with p-wave superconducting pairing serves as a exemplary example of a topological superconductor and provides an elegant, exactly solvable framework for understanding the emergence of Majorana bound states. The Kitaev chain Hamiltonian is given by

$$H = -\sum_j \mu c_j^\dagger c_j + \sum_j \left(-t\, c_{j+1}^\dagger c_j - \Delta c_{j+1}^\dagger c_j^\dagger + \text{h.c.}\right). \tag{2.12}$$

where μ is the chemical potential, Δ is the superconducting order parameter for the p-wave superconducting pairing, and c_j are fermionic annihilation operators.

From a symmetry perspective, the addition of superconductivity breaks particle-number conservation but preserves particle-hole symmetry. The Kitaev model exhibits two distinct phases namely, a topologically trivial phase and a topologically non-trivial phase, separated by a quantum phase transition. To understand how these phases arise, we can diagonalize

the Hamiltonian using the Bogoliubov-de Gennes (BdG) formalism. First, we transform the real-space Hamiltonian into momentum space by introducing the Fourier transform of the fermionic operators

$$c_j = \frac{1}{\sqrt{N}} \sum_k e^{\imath\, k\, j} c_k \tag{2.13}$$

where N is the number of sites and k represents the momentum. To analyze the Kitaev chain in momentum space, we introduce the Nambu spinor $\Psi^\dagger = \begin{pmatrix} c_k^\dagger & c_{-k} \end{pmatrix}$ and the finally the Hamiltonian in BdG basis is $H = (1/2) \sum_k \Psi^\dagger \mathcal{H}_k \Psi$ and $\mathcal{H}$ is given by

$$\mathcal{H}_k = -(\mu + 2t\cos k)\sigma_z - 2\Delta \sin k \sigma_y \tag{2.14}$$

$$= \begin{pmatrix} -\mu - 2t\cos k & 2\imath\Delta \sin k \\ -2\imath\Delta \sin k & \mu + 2t\cos k \end{pmatrix}. \tag{2.15}$$

Here σ_y, and σ_z are the Pauli matrices. The eigenvalues of this matrix determine the energy spectrum, i.e. quasiparticle energy spectrum.

$$E_k = \pm\sqrt{(\mu + 2t\cos k)^2 + (2\Delta \sin k)^2} \tag{2.16}$$

The system is gapped when $E_k \neq 0$ for all k. A topological phase transition occurs when the energy gap closes because the gap closing point signifies a qualitative change in the bulk band structure's topology. A topological phase transition occurs when the energy gap closes, i.e., $E_k = 0$ for some momentum k. This happens when both terms under the square root are simultaneously zero hence

$$\mu + 2t\cos k = 0\ ,\ \text{and} \quad 2\Delta \sin k = 0 \tag{2.17}$$

From the second condition, $\sin k = 0$, which implies $k = 0$ or $k = \pi$. If $k = 0$, the first condition becomes $2t + \mu = 0$, or $\mu = -2t$. If $k = \pi$, the first condition becomes $-2t + \mu = 0$, or $\mu = 2t$. Thus, the quantum phase transitions occur at $\mu = \pm 2t$. In the trivial phase, typically characterized by $|\mu| > 2t$, the system behaves as a conventional insulator, and no zero-energy edge states are present. However, when the system enters the topological non-trivial phase, defined by $|\mu| < 2t$ and a finite Δ, the bulk becomes superconducting with a finite energy gap, but remarkably, two zero-energy Majorana bound states emerge, localized at the ends of the chain. These MBS are robustly protected by the bulk energy gap and the inherent particle-hole symmetry of the Hamiltonian. The existence of these zero-energy

modes leads to a twofold degeneracy in the ground state, a hallmark of topological order. This bulk-boundary correspondence, where the topological properties of the bulk dictate the existence of boundary states, is a central concept in topological phases of matter. The Kitaev model's simplicity allows for a clear demonstration of how tuning system parameters (like μ) can drive a transition between these topologically distinct phases, making it an invaluable theoretical tool for understanding more complex real-world systems.

2.2.1 Emergence of Majorana zero modes in Kitaev chain

The existence and localization of Majorana zero modes depend critically on the parameters of the Hamiltonian. When the parameters are such that $|\mu > 2t$, the system enters the topologically trivial phase. In this regime, the energy gap closes and reopens, but the system now has no zero-energy modes. The topological phase is defined by the condition $|\mu| < 2t$, within this phase, the system has a bulk energy gap and hosts Majorana zero modes at its ends. The essence of the Kitaev chain's topological phase lies in a change of basis from conventional fermions to Majorana operators. Each fermionic operator can be decomposed into a pair of real, Hermitian Majorana operators:

$$c_j = \frac{1}{2}(\gamma_{j,1} + \imath\gamma_{j,2}), \quad \text{and} \quad c_j^\dagger = \frac{1}{2}(\gamma_{j,1} - \imath\gamma_{j,2}) \tag{2.18}$$

By substituting these expressions into the Hamiltonian (Eq. (2.12)) and considering the topological regime, the Hamiltonian can be rewritten in a remarkably simple form. For the specific case where $t = \Delta$ and $\mu = 0$, the Hamiltonian simplifies to

$$H = \sum_{j}^{N} \gamma_{j,2}\gamma_{j+1,1} \tag{2.19}$$

here N is the number of sites in the chain. This form reveals the core mechanism of localization. The Hamiltonian consists of terms that pair up a Majorana mode from site j with the mode from site $j + 1$. However, the very first Majorana operator, $\gamma_{1,1}$, and the very last one, $\gamma_{N,2}$, are left unpaired and are not present in the Hamiltonian. Since these operators do not contribute to the system's energy, they form the zero-energy modes. Because they are only present at the ends of the chain, their existence is localized to the boundaries. This zero-energy, and spatially separated state are the Majorana zero mode, which is protected from local perturbations as long as the system remains in its topological phase.

We can analyze the zero-energy eigenstate of the system. Consdering the Majorana mode is given by the state $(\psi_1, \cdots, \psi_N, \phi_1, \cdots, \phi_N)$, the equation for a zero-energy state at site

j,in the BdG basis is given as:

$$-t(\psi_{j+1} + \psi_{j-1}) - \mu\psi_j - \Delta(\phi_{j+1} - \phi_{j-1}) = 0 \tag{2.20}$$

$$-t(\phi_{j+1} + \phi_{j-1}) - \mu\phi_j + \Delta(\psi_{j+1} - \psi_{j-1}) = 0 \tag{2.21}$$

as the Majorana zero modes are their own antiparticle $\psi_j = \phi_j^*$. This is a second-order recurrence relation. The solution has the form $\psi_j \propto r^j$, using this this form yields a characteristic equation for r, whose roots are:

$$r_\pm \quad = \quad \frac{-\mu \pm \sqrt{\mu^2 + 4\Delta^2 - 4t^2}}{(t + \Delta)} \tag{2.22}$$

The true solution of the Majorana modes turn out to be linear combination of r_+ and r_-. In the topological phase, where $|\mu| < 2t$, the solutions are complex with an amplitude less than one, $|r| < 1$. This means the wavefunction decays exponentially as it moves away from the boundary. The amplitude of the left-end mode at site j is proportional to $e^{-j/\xi}$, and similarly for the right-end mode. ξ is the localization length or correlation length of the system. The correlation length depends on the parameters of the Hamiltonian. This splitting is described by the energy of the coupled state, which decays exponentially with the length of the chain:

$$E \quad \propto \quad e^{-N/\xi} \tag{2.23}$$

For the topological phase, the value of ξ remains finite, and as long as the chain is much longer than this length ($\xi \ll N$), the energy splitting becomes negligible, and the modes are effectively at zero energy. This exponential suppression of the energy splitting is the crucial element of topological protection, as it makes the modes highly robust against local perturbations and noise.

2.2.2 Majorana bound states

The theoretical foundation for MBS lies in the Bogoliubov transformation, a canonical transformation that fundamentally differs from the unitary transformations typically employed in the SSH model. For a superconducting system characterized by a pairing potential Δ, this transformation elegantly mixes electron and hole operators to create new, independent quasiparticle excitations [c.f. Fig. 2.3(c)-(d)]. In experimental realizations of 1D topological superconductivity, particularly in semiconductor nanowire and atomic chains, the superconducting pairing potential Δ is typically introduced via the *proximity effect*. This phenomenon

occurs when a non-superconducting material, such as a semiconductor nanowire with strong spin-orbit coupling, is brought into intimate contact with a conventional s-wave superconductor (e.g., Al or Nb) [51]. The Cooper pairs from the conventional superconductor leak into the adjacent non-superconducting material, inducing a superconducting gap and effectively imbuing it with superconducting properties. This induced superconductivity, combined with a Zeeman field (to break time-reversal symmetry and open a topological gap) and strong spin-orbit coupling inherent to the semiconductor, can drive the system into a topological superconducting phase.

Semiconductor-superconductor hybrid structures, often involving InAs or InSb nano wires grown epitaxially with superconducting shells, have been a prominent platform for these investigations. Early seminal works, such as those by Mourik et al. [12] and Deng et al. [52], demonstrated zero-bias conductance peaks in such devices, interpreted as signatures of MBS. Similarly, in atomic chains, superconductivity is introduced by depositing magnetic atoms (e.g., Fe) on a superconducting substrate (e.g., Pb). The magnetic moments of the atoms, coupled with the proximity-induced superconductivity from the substrate, can create the necessary conditions for topological superconductivity and the emergence of MBS at the chain ends, as explored in experiments by Nadj-Perge et al. [40]. The strength and nature of this induced pairing potential are critical parameters that dictate the topological phase and the properties of the resulting MBS. Specifically, the electron annihilation operators $c_{i\uparrow}$

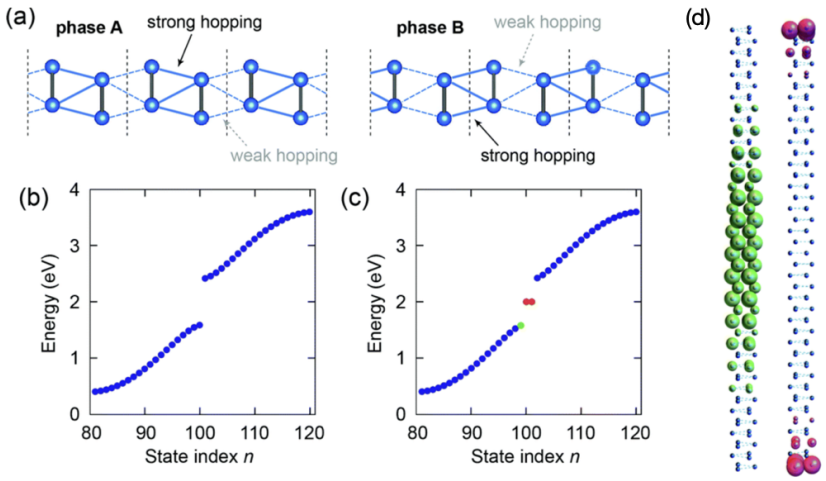

Figure 2.2: 1D metallic chain of M_6X_6 (M=Mo, and W; X=S, Se, and Te) shows two different phase for a finite chain with length of 20 unit cells. (a) Is the topologically trivial phase with the corresponding (b) energies levels. Phase B however, is topologically non-trivial and shows (c) zero energy modes in the energy levels. (d) These zero energy modes indeed lead to MBS localised at the ends of the nanowire (red). Adopted from Ref. [53].

and $c_{i\downarrow}$ are expressed as linear combinations of new quasiparticle operators γ_n and their

conjugates $\gamma_n^\dagger$

$$\begin{aligned} c_{i\uparrow} &= \sum_n \left(u_{in\uparrow}\gamma_n + v^*_{in\uparrow}\gamma_n^\dagger \right) \\ c_{i\downarrow} &= \sum_n \left(u_{in\downarrow}\gamma_n - v^*_{in\downarrow}\gamma_n^\dagger \right) \end{aligned} \tag{2.24}$$

where u and v represent the electron and hole components, respectively, of the quasiparticle wavefunctions. A key condition for a quasiparticle operator to represent a self-conjugate Majorana fermion is $\gamma = \gamma^\dagger$. This unique condition is naturally fulfilled at zero energy within the topological phase of superconductors, leading to MBS (as shown in Fig. 2.2(d)) that robustly localize at boundaries or defects of the material.

Unlike the electronic edge states found in the SSH model, MBS exhibit a remarkable property of it having a non-local entanglement. A pair of MBS can share quantum information while being spatially separated, meaning their quantum state is distributed across the physical ends of the topological superconductor. This intrinsic non-locality makes them exceptionally robust against local perturbations and decoherence, rendering them highly promising candidates for the realization of fault-tolerant topological quantum computing. However, their experimental identification presents significant challenges, as it requires careful distinction from trivial zero-energy states, such as Andreev bound states, which can mimic some of their signatures. This necessitates the application of multiple complementary measurement techniques to unequivocally confirm the presence of Majorana states.

2.2.3 Bogoliubov–de Gennes equations

The BdG Hamiltonian provides a mean-field description of superconducting systems, effectively transforming the many-body problem of interacting electrons into a single-particle problem of quasiparticles. In momentum space, the minimal model for 1D topological superconductors, often realized in semiconductor nanowires, can be elegantly captured by the following BdG Hamiltonian [12, 52] :

$$H_{BdG} = (\epsilon_k - \mu)\tau_z + \Delta\tau_x + \lambda k\sigma_z\tau_z + B\sigma_x \,. \tag{2.25}$$

Each term in this Hamiltonian plays a critical role in shaping the electronic and superconducting properties that ultimately lead to topological phases. The first term, $(\epsilon_k - \mu)\tau_z$, describes the normal state kinetic energy and the chemical potential. Here, $\epsilon_k = -2t\cos ka$ represents the tight-binding dispersion for electrons hopping between sites with amplitude t on a lattice with spacing a. The Pauli matrix τ_z acts in particle-hole space, ensuring that

this term contributes with opposite signs for particles and holes, a fundamental aspect of the BdG formalism. The second term, $\Delta\tau_x$, introduces the s-wave superconducting pairing potential, Δ [c.f. Fig. 2.3]. The Pauli matrix τ_x is responsible for mixing particle and hole components, which is the essence of Cooper pair formation in a superconductor. This term opens a superconducting gap in the bulk excitation spectrum, a prerequisite for the emergence of protected zero-energy modes.

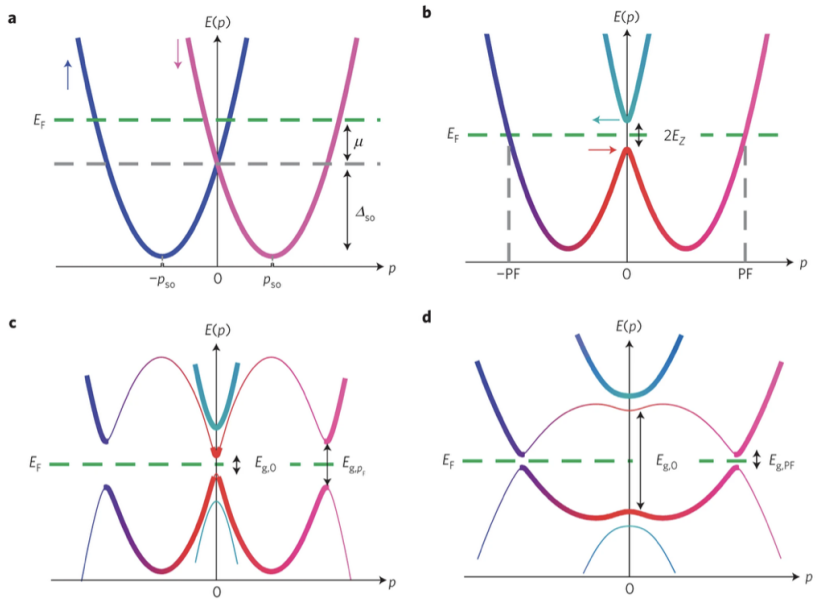

Figure 2.3: The energy bands of an infinite nanowire. (a) The bands split due to spin-orbit coupling (Δ_{SO}) into spin-up (blue) and spin-down (magenta). (b) Introduction of a Zeeman field spilts the energy of bands near the band crossing point ($p = 0$) and a gap opens up ($2E_Z$). (c) As superconductivity is induced in the system there appear energy bands for holes (light) and opening a superconducting gap. (d) Shows the effect of further increasing the Zeeman field which broadens the gap near $p = 0$. Adopted form Ref. [54].

The remaining two terms are vital for engineering the topological phase. The third term, $\lambda k\sigma_z\tau_z$, represents the Rashba spin-orbit coupling (SOC), with λ as its strength [c.f. Fig. 2.3(a)]. This interaction arises from structural inversion asymmetry and couples the electron's momentum k to its spin, specifically through the σ_y Pauli matrix in spin space. The τ_z matrix again ensures its particle-hole symmetric nature. Rashba SOC is crucial as it lifts the spin degeneracy of the electronic bands and creates a helical band structure, where spin and momentum are locked. Finally, the $B\sigma_x$ term accounts for the Zeeman energy induced by an external magnetic field B. This term acts purely in spin space via σ_x, explicitly breaking time-reversal symmetry and further splitting the spin-degenerate bands created by SOC. The interplay of strong spin-orbit coupling and a sufficiently strong Zeeman field is paramount for driving the system into a topological superconducting phase, as it effectively

creates an analogue of a p-wave superconductor from a conventional s-wave one.

A defining characteristic of the BdG Hamiltonian in this context is its particle-hole symmetry, implemented by the anti-unitary operator $\mathcal{P} = \tau_x K$, where K denotes complex conjugation. As we saw in the Chapter 1, this symmetry dictates that for every eigenstate of the Hamiltonian with energy E, there exists a corresponding eigenstate with energy $-E$. Mathematically, this is expressed as $\{H_{BdG}(k), \mathcal{P}\} = 0$. This fundamental symmetry is the bedrock upon which Majorana bound states are built, as it guarantees that if a zero-energy solution exists, it must be its own anti-particle, i.e., a Majorana fermion ($\gamma = \gamma^\dagger$) (as shown in FIg. 2.2(c)-(d)). The topological phase transition occurs when the bulk energy gap, which separates the positive and negative energy quasiparticle excitations, closes at specific points in momentum space (typically $k = 0$ or $k = \pi$) and then reopens. This gap closing signifies a change in the topological invariant of the system, leading to the emergence of robust, non-degenerate zero-energy states at the system's boundaries in a finite-sized wire.

2.3 Spin-full Nanowires

Two primary platforms have emerged, semiconductor nanowires exhibiting proximity-induced superconductivity and meticulously engineered atomic chains on superconducting surfaces. Semiconductor nanowires, typically fabricated from materials possessing strong spin-orbit coupling (e.g., InSb, InAs) and interfaced with a conventional superconductor (e.g., NbTiN, Al), are designed to host a topological superconducting phase when subjected to an external magnetic field. This configuration aims to foster a regime where the interplay of spin orbit coupling, superconductivity, and Zeeman splitting facilitates the emergence of MBS at the nanowire terminals. Concurrently, atomic chains, comprising magnetic atoms (e.g., Fe, Co) precisely manipulated on the surface of a superconductor (e.g., Pb, Nb), present an alternative and highly controllable environment for MBS formation [40, 55–57]. In these systems, the intrinsic magnetic ordering of the atoms can induce a topological phase in the underlying superconductor, leading to the manifestation of zero-energy states at the ends of the chain. This methodology offers the distinct advantage of atomic scale precision in fabrication and the capacity for direct probing of the spatial characteristics of these edge states via STM.

We consider a generalized Hamiltonian framework, often rooted in the tight-binding approximation. This offers a powerful and intuitive platform for understanding and predicting topological phenomena. We begin with a 1D chain, with s-type superconductivity resulting from proximity-induced effects. We consider an external magnetic field along with Rashba

spin-orbit coupling (SOC) [58]. While an external magnetic field is a common ingredient for breaking time-reversal symmetry and driving a system into a topological superconducting phase.

Building on the understanding of the role of the magnetic field, Klinovaja *et. al* [59] proposed an alternative mechanism where Majorana zero modes could be stabilized by helical nuclear spin order instead of an external magnetic field. This implies that the effective Zeeman-like term in the generalized Hamiltonian could originate from internal material properties rather than an applied field. Extending this, the framework also accommodates other complex magnetic orderings, such as ferromagnetic ordering, and anti-ferromagnetically ordered chain, subjected to an external magnetic field oriented along the nanowire. The low-energy physics of this system is captured by the following Hamiltonian

$$H = H_0 + H_{SC} + H_{FM/AFM} \tag{2.26}$$

Here, H_0 describes the Rashba nanowire, H_{SC} represents the induced superconductivity, and $H_{FM/AFM}$ accounts for the ferromagnetic or antiferromagnetic order within the nanowire. This Hamiltonian can be presented in the tight binding formalism as follows

$$\begin{aligned} H_0 = & \sum_{ij,ss',\sigma} [-t_{ij}^{ss'} - (\mu + h\sigma)\delta_{ij}\delta_{ss'}] c_{is\sigma}^{\dagger} c_{js'\sigma} \\ & -\imath\lambda \sum_{i,\sigma,\sigma'} [c_{iA\sigma}^{\dagger} \sigma_{\sigma\sigma'}^{y} c_{iB\sigma'} + c_{iB\sigma}^{\dagger} \sigma_{\sigma\sigma'}^{y} c_{i+1A\sigma'}] + \text{h.c.} \end{aligned} \tag{2.27}$$

where $c_{is\sigma}^{\dagger}(c_{is\sigma})$ is the creation (annihilation) operator for electron with spin σ in sublattice $s \in \{A, B\}$ in the ith unit cell (incase of AFM). We only have nearest neighbor hopping hence, $t_{ij}^{ss'} = t = 1$ for the adjacent sites and zero otherwise. μ is the chemical potential and h is the external Zeeman field. λ denotes the strength of SOC. Additionally, the induced superconductivity is of BCS-type with Δ being the superconducting order parameter and H_{SC} is given by

$$H_{SC} = \Delta \sum_{is} \left(c_{is\uparrow}^{\dagger} c_{is\downarrow}^{\dagger} + c_{is\downarrow} c_{is\uparrow} \right) \tag{2.28}$$

The antiferromagnetic (AFM) ordering is given by

$$H_{AFM} = -m_0 \sum_{i\sigma} \sigma \left(c_{iA\sigma}^{\dagger} c_{iA\sigma} - c_{iB\sigma}^{\dagger} c_{iB\sigma} \right) \tag{2.29}$$

here, m_0 is the amplitude of the AFM order. Moreover, the ferromagnetic term is given as

$$H_{FM} = \frac{J}{2}\sum_{i\sigma\sigma'} c^{\dagger}_{i\sigma}(\boldsymbol{S}_i \cdot \boldsymbol{\sigma}_{\sigma\sigma'})c_{i\sigma} \tag{2.30}$$

$\boldsymbol{S}_i$ is the site dependent magnetic moment with the assumption that the governing dynamics are much slower than electron. J is the magnitude of the magnetic moment. This forms the real space representation of the tight binding model for a nanowire with Rashba SOC and AFM order.

2.3.1 Topological phases of nanowire

Lutchyn *et. al* [58], and Oreg *et. al* [60], independently proposed that a 1D semiconductor nanowire with strong spin-orbit coupling, such as InAs or InSb, in proximity to a conventional s-wave superconductor and subjected to an external magnetic field can host Majorana zero modes at its ends. This concept was further extended the theory to different type of hybrid system by Dumitrescu *et. al* [61], and proposed the realization of Majorana fermions in chiral topological ferromagnetic nanowires, highlighting the role of induced superconductivity in ferromagnetic systems. Similarly, Alicea [62] demonstrated that Majoranas could potentially exist in 1D quantum wires even without a long-range superconducting order. Ferromagnetism

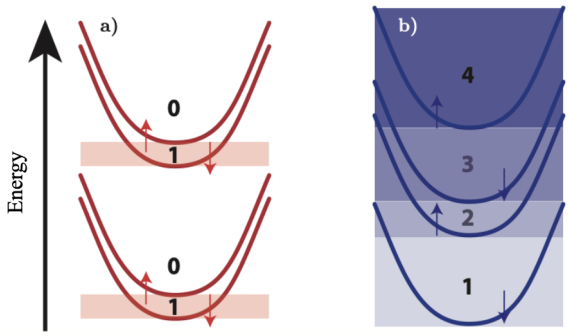

Figure 2.4: (a) Shows the energy bands of a class D topological nanowire. The original bands are influenced by the spin-orbit coupling in the system creating degenrate bands which is lifted by an external Zeeman field (as marked by red arrows). When the Fermi level lies in the pink shaded region, an induced superconductivity can create a Majorana zero modes at the ends of the wire. (b) Shows the bands for the multichannel ferromagnetic nanowire. An induced superconductivity of p-type transforms the system to BDI class widening the range of parameters which allow topological phase of nanowaire. As μ is increased the number of Majorana zero modes increase as shown in the shaded region. Adopted from Ref. [61].

and superconductivity are typically at odds, as a ferromagnet's internal magnetic field breaks the Cooper pairs necessary for superconductivity. However, in a 1D system, this very conflict can create a new, topologically non-trivial state. This phenomenon is analogous to the

Kitaev chain, where the spinless fermions with p-wave with superconducting pairing give rise to topological phase. In hybrid nanowires, the key principle is that the spin-polarized band structure, created by the ferromagnetic exchange field, can effectively split into two sub-bands [c.f. Fig. 2.4]. Each of these sub-bands behaves like a separate Kitaev chain, which can lead to chiral topological superconductivity [61]. 1D nanowire made from metallic transition metal monochalcogenide, M_6X_6 (M = Mo, and W; X = S, Se, and Te) have been synthesized experimentally. Jin *et. al* [53], using the extended version of SSH model (reinforced by the first principle calculations) showed that the boundary is inhabited by Dirac fermions. Opening a gap at the Dirac point leads to emergence of edge modes in the system.

In order to uncover the topological phases of the nanowire with AFM order, we begin with Fourier transforming the Hamiltonian to represent it in the momentum space which gives following

$$\begin{aligned} H_0(k) &= \sum_{k,\sigma} \epsilon_k \left(c^\dagger_{kA\sigma} c_{kB\sigma} + \text{h.c.}\right) - \sum_{k,s,\sigma} (\mu + h\sigma)\, c^\dagger_{ks\sigma} c_{ks\sigma} \\ &\quad + \sum_{k,\sigma,\sigma'} \imath\lambda_k (c^\dagger_{kA\sigma} \sigma^y_{\sigma\sigma'} c_{kB\sigma'} + \text{h.c.}) \end{aligned} \tag{2.31}$$

here, $\epsilon_k = -2t\cos k$, and $\lambda_k = -2\imath\lambda \sin k$. Additionally,

$$H_{SC}(k) = \Delta \sum_{ks} (c^\dagger_{ks\uparrow} c^\dagger_{-ks\downarrow} + c_{-ks\downarrow} c_{ks\uparrow}) \tag{2.32}$$

$$H_{AFM}(k) = -m_0 \sum \sigma (c^\dagger_{kA\sigma} c_{kA\sigma} - c^\dagger_{kB\sigma} c_{kB\sigma}) \tag{2.33}$$

we now define the Nambu spinor $\psi^\dagger_k = \left(c_{kA\uparrow}\ c_{kB\uparrow}\ c_{kA\downarrow}\ c_{kB\downarrow}\ c^\dagger_{-kA\uparrow}\ c^\dagger_{-kB\uparrow}\ c^\dagger_{-kA\downarrow}\ c^\dagger_{-kB\downarrow}\right)$. The Hamiltonian can now be written as $H(k) = \sum_k \psi^\dagger_k \mathcal{H}_k \psi_k$, here $\mathcal{H}_k$ is the BdG Hamiltonian which has the following form

$$\begin{aligned} \mathcal{H}_k &= \epsilon_k \boldsymbol{\tau}^3 \boldsymbol{\sigma}^0 \boldsymbol{\rho}^1 - \mu \boldsymbol{\tau}^3 \boldsymbol{\sigma}^0 \boldsymbol{\rho}^0 - h \boldsymbol{\tau}^3 \boldsymbol{\sigma}^3 \boldsymbol{\rho}^0 + \imath\lambda_k \boldsymbol{\tau}^3 \boldsymbol{\sigma}^2 \boldsymbol{\rho}^1 \\ &\quad - \Delta \boldsymbol{\tau}^2 \boldsymbol{\sigma}^2 \boldsymbol{\rho}^0 - m_0 \boldsymbol{\tau}^3 \boldsymbol{\sigma}^3 \boldsymbol{\rho}^3 \end{aligned} \tag{2.34}$$

The Pauli matrices $\boldsymbol{\tau}$, $\boldsymbol{\sigma}$, $\boldsymbol{\rho}$ signify the subspace of the Hamiltonian associated with particle-hole, spin and sublattice subspace respectively. The BdG Hamiltonian inherently possesses particle-hole symmetry. This is a fundamental symmetry for superconductors. It is described by the anti-unitary operator $\mathcal{P} = \boldsymbol{\tau}^1 \boldsymbol{\sigma}^0 \boldsymbol{\rho}^0 K$, where K is the complex conjugation operator and as usual the operator satisfies $\mathcal{P}^{-1} \mathcal{H}_k \mathcal{P} = -\mathcal{H}_{-k}$. We can define another operator say $\mathcal{T} = \boldsymbol{\tau}^0 \boldsymbol{\sigma}^0 \boldsymbol{\rho}^0 K$. The Hamiltonian follows $\mathcal{T}^{-1} \mathcal{H}_k \mathcal{T} = \mathcal{H}_{-k}$ and $\mathcal{T}^2 = 1$. Although the

Hamiltonian lacks physical time reversal symmetry, this new operator replaces it as a pseudo time reversal symmetry of BdG Hamiltonian. Lastly, the Hamiltonian possess the chiral or in this case the sublattice symmetry. The symmetry is given by operator $\mathcal{S} = \mathcal{P}\mathcal{T}$.

Given the presence of particle-hole symmetry and chiral symmetry, but the absence of time-reversal symmetry, this Hamiltonian belongs to Symmetry Class BDI in the tenfold classification. For 1D systems in Class BDI, the topological invariant is a $\mathbb{Z}$ invariant, meaning it can take any integer value. A gapped BdG Hamiltonian $\mathcal{H}_k$ in Class BDI (which includes Class D as a special case where chiral symmetry is absent), the topological invariant can be related to the sign of the Pfaffian of the Hamiltonian evaluated at specific high-symmetry points in the Brillouin zone. For 1D systems, these crucial points are $k = 0$ and $k = \pi/2$. The Pfaffian of an antisymmetric matrix A is defined such that $\mathrm{Pf}(A)^2 = \det(A)$. To utilize the Pfaffian, the BdG Hamiltonian it is typical to transform the BdG Hamiltonian into the chiral form where is takes a completely off-diagonal form. For the system under consideration it can be done via unitary rotation by $U = e^{\imath\frac{\pi}{4}\boldsymbol{\tau}^2}\boldsymbol{\sigma}^0\boldsymbol{\rho}^0$. The BdG Hamiltonian takes the following form

$$\hat{\mathcal{H}}_k = U^\dagger \mathcal{H}_k U = \begin{pmatrix} 0 & \mathcal{A}(k) \\ \mathcal{A}^\dagger(-k) & 0 \end{pmatrix} \tag{2.35}$$

here

$$\mathcal{A}(k) = \epsilon_k \boldsymbol{\sigma}^0\boldsymbol{\rho}^1 - \mu\boldsymbol{\sigma}^0\boldsymbol{\rho}^0 - h\boldsymbol{\sigma}^3\boldsymbol{\rho}^0 + \imath\lambda_k\boldsymbol{\sigma}^2\boldsymbol{\rho}^1 + \imath\Delta\boldsymbol{\sigma}^2\boldsymbol{\rho}^0 - m_0\boldsymbol{\sigma}^3\boldsymbol{\rho}^3 \tag{2.36}$$

The $\mathbb{Z}_2$ topological invariant of the BdG Hamiltonian is captured by the Pfaffian. This invariant captures the change in the sign of the Pfaffian as k crosses the topological phase transition, which corresponds to the closing and reopening of the bulk energy gap. If the

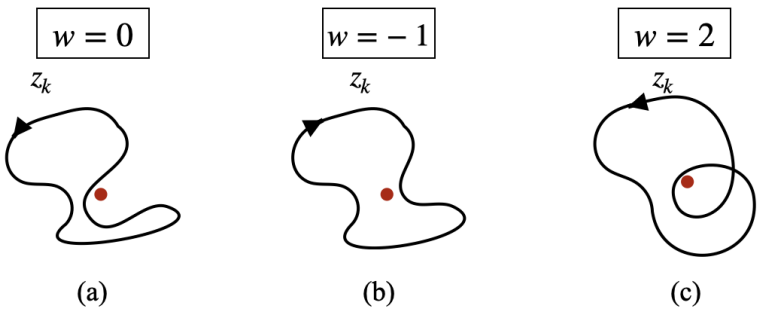

Figure 2.5: A schematic representation of closed path traversed by z_k shown by the arrow as k changes within BZ. (a) Winding number $w = 0$ as the origin excluded gives no contribution in the Eq. (2.39). However, (b) has $w = -1$,, and (c) has $w = 2$.

non-trivial topological phase is captured by a quantity say $\mathcal{Q} = -1$ and topological trivial phase with $\mathcal{Q} = 1$ then

$$\mathcal{Q} = \text{sgn}[\text{Pf}(\mathcal{W}(k=0))] \cdot \text{sgn}[\text{Pf}(\mathcal{W}(k=\pi/2))] \tag{2.37}$$

here $\mathcal{W} = \mathcal{H}_k\mathcal{S}$, using the fact that $\det(U) = 1$

$$\begin{aligned} \text{Pf}(\mathcal{W}(k)) &= \text{Pf}[U^\dagger \mathcal{H}_k U \mathcal{S}] \\ &= \text{Pf}[U^\dagger \mathcal{H}_k U \mathcal{S} U^T U^*] \\ &= \det(U^\dagger)\text{Pf}[\mathcal{H}_k U \mathcal{S} U^T] \\ &= \text{Pf}[-\mathcal{H}_k \boldsymbol{\tau}^3 \boldsymbol{\sigma}^0 \boldsymbol{\rho}^0] \\ &= \det(\mathcal{A}(k)) \end{aligned} \tag{2.38}$$

The full $\mathbb{Z}$ topological invariant is given by the winding number. The winding number w is defined based on the topological information captured by the off-diagonal block $\mathcal{A}$. The winding number is given by [63, 64]

$$w = \frac{1}{2\pi\imath}\int_{-\pi}^{\pi} \frac{dz_k}{z_k} \tag{2.39}$$

here, $z_k = \det(\mathcal{A})$. In essence, the integral measure the 'winding' of the $\mathcal{A}$ matrix as the momentum spans the Brillouin zone. More specifically, it quantifies the number of times the determinant encircles the complex plane [c.f. Fig. 2.5]. A non-zero integer value for w signifies a topologically non-trivial phase, directly correlating with the presence of zero-energy MBS at the system's boundaries. This general formulation provides a robust way to calculate the topological invariant even for more complex multi-band systems that can be reduced to this block off-diagonal form.

It is important to distinguish this from the topological classification of the SSH model. While systems like Kitaev chain or nano wires and the SSH model host zero-energy edge states, their underlying physics and the nature of these states differ fundamentally. The SSH model describes dimerization in a non-superconducting chain. Dimerization refers to the alternating bond strengths within the 1D lattice, effectively breaking the translational symmetry of a uniform chain into a two atom unit cell. This was typically captured by the different sign of δt in the hopping parameters (say t_1 and t_2) as we saw in previous section. The hopping t_1 connects atoms within the same unit cell (e.g., A to B), while t_2 connects atoms between adjacent unit cells (e.g., B in cell n to A in cell $n+1$). The

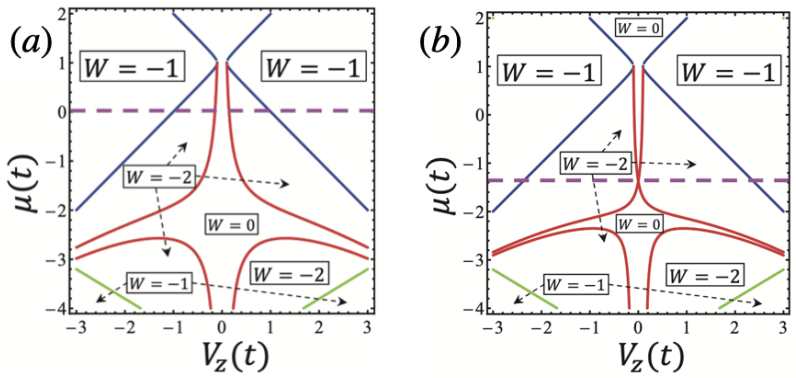

Figure 2.6: In a nanowire with an external Zeeman field the induced superconductivity produces both an s-type (Δ_1) and p-type (Δ_2). (a) The topological phase diagram for the case where $\Delta_1 > \delta_2$ and (b) $\Delta_1 = \Delta_2$. Adopted from Ref. [65].

relative strengths of t_1 and t_2 determine the topological phase. When $|t_1| > |t_2|$, the chain is effectively "dimerized" with strong bonds within the unit cell, leading to a trivial insulating phase. Conversely, when $|t_1| < |t_2|$, the strong bonds are between unit cells, resulting in a topologically non-trivial phase characterized by zero-energy fermionic edge states that are protected by chiral (sublattice) symmetry and characterized by an integer winding number related to sublattice polarization.

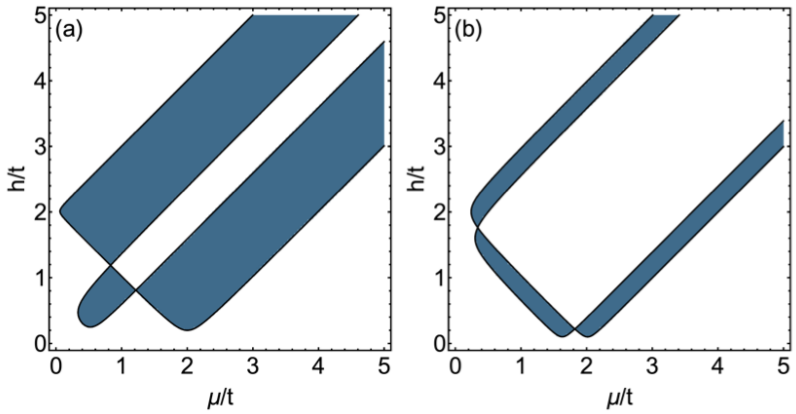

Figure 2.7: The topological phase diagram for a dimerized nanowire (SSH like) with hopping parameters given by $t(1 \pm \delta)$ with external magnetic field h, Rashba SOC and proximated superconductivity. The blue region signifies a non-trivial topological region of the phase space. (a) $\delta = 0.2$ and (b) $\delta = 0.8$ clearly show that the dimerization reduces the topologically non-trivial region of the phase. Adopted from Ref. [66].

In the much more versatile case of nanowires there are multiple parameters that are involved. Winding number phase diagram involves systematically varying two parameters of the Hamiltonian and calculating the winding number for each combination. This process reveals distinct regions of the topological phase where the winding number maintains a constant integer value, separated by phase boundaries where the bulk energy gap closes. The com-

parison of these phase diagrams, generated by varying different potentials, offers profound insights into the mechanisms driving topological superconductivity. Chemical potential (μ) vs. Zeeman field (h) is a foundational type of phase diagram for topological superconductivity in nanowires. It typically illustrates the transition from a trivial to a topological phase as the Zeeman energy (h) surpasses a critical value, often forming a parabolic-like region in the $\mu - h$ plane where MBS are expected. The chemical potential (μ) is typically controlled experimentally by gate voltages, and the Zeeman energy by an external magnetic field (h). Fig. 2.6 shows the phase diagram by marking different winding numbers separated by colored lines. The nanowire under study is composed of 1D lattice sites with each having two sublattices. The system is under an external Zeeman field and has a proximity induced superconductivity of s type. They further consider the superconducting amplitude to be Δ_1 between the sites within same lattice site and Δ_2 between sites from adjacent lattice sites.

On the contrary, a system with a homogeneous s type superconductivity given by Δ and a dimerized hopping like the SSH model was studied by Kobiałka *et. al* [66]. Fig. 2.7 plots the topological phase of a dimerised nanowire with Rashba SOC. It is evident how small variations in the parameters can drastically change the topological phase of the system.

Kobiałka *et. al* [67] studied a nanowire with proximity induced s type superconductivity. The nanowire is subjected to an external magnetic field along with an internal antiferromagnetic order parametrized by m_0. The nanowire also has a Rashba SOC, and the topological phase is shown in Fig. 2.8. Additionally, Crawford *et. al* [68] studied a nanowire with an antiferromagnetic order. Although the underlying mechanism for spin orbit coupling and AFM order is different from [67] the phase diagrams show remarkable similarity as shown in Fig. 2.9.

2.3.2 Edge modes of nanowire

We adopt the Bogoliubov–de Gennes (BdG) representation, as the formalism is a standard theoretical framework for describing superconductivity in systems where a single-particle Hamiltonian is known. This formalism is particularly well-suited for studying topological superconductors as it naturally incorporates the pairing of electrons and holes, which is fundamental to the superconducting state. In BdG basis, $c_{is\sigma} = \sum_n \left(u_{is\sigma n}\gamma_n - \sigma v^*_{is\sigma n}\gamma_n^\dagger\right)$, here γ_n are the fermionic operators. Diagonalizing the BdG Hamiltonian yields the quasiparticle energy spectrum of the superconducting system. The BdG formalism is crucial for identifying the conditions under which zero-energy Majorana modes appear. Majorana modes correspond to zero-energy eigenstates of the BdG Hamiltonian that satisfy the Majo-

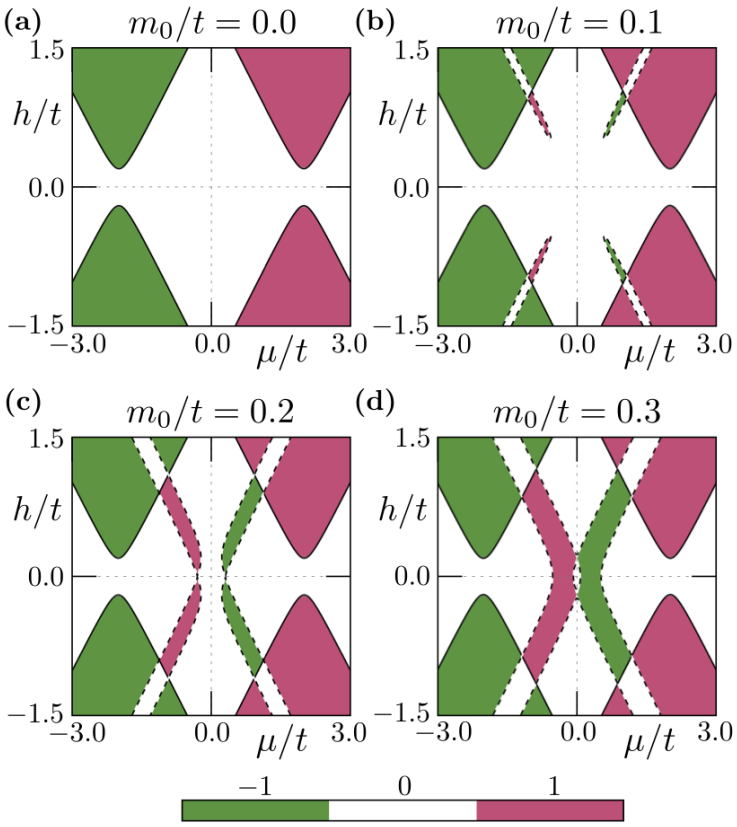

Figure 2.8: Topological phase diagram for a Rashba nanowire with proximated superconductivty (Δ) and a Zeeman field (h). The chain has an AFM ordering (m_0) and the topological phase demonstrate the effect of topological region in (a)-(d). Increasing the strength of AFM introduces new region of non-trivial topological phase which end up connecting the parabolic regions of (a) $m_0 = 0$ as shown in (c) and (d). Adopted from Ref. [67].

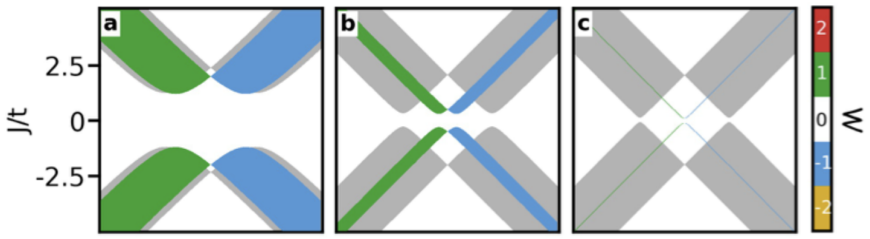

Figure 2.9: The topological phase for an AFM nanowire based on magnetic adatoms on Nb-inspired superconducting substrate. Phase diagram are made for chemical potential μ vs. Zeeman strength J for (a) $(\Delta, \lambda) = (1.2t, 0.8t)$, (b) $(\Delta, \lambda) = (0.3t, 0.2t)$, and (c) $(\Delta, \lambda) = (0.1t, 0.01t)$. λ begin the Rashba SOC and Δ is the superconducting order parameter. Adopted from Ref. [68].

rana condition, meaning they are their own antiparticles which mathematically translates to $\gamma_m = \gamma_m^\dagger$.

The theoretical framework for Majorana Bound States in one-dimensional systems, particularly nanowires, hinges on the delicate interplay of several fundamental physical ingredients: strong spin-orbit coupling, a magnetic field, and proximity-induced superconductivity. In a

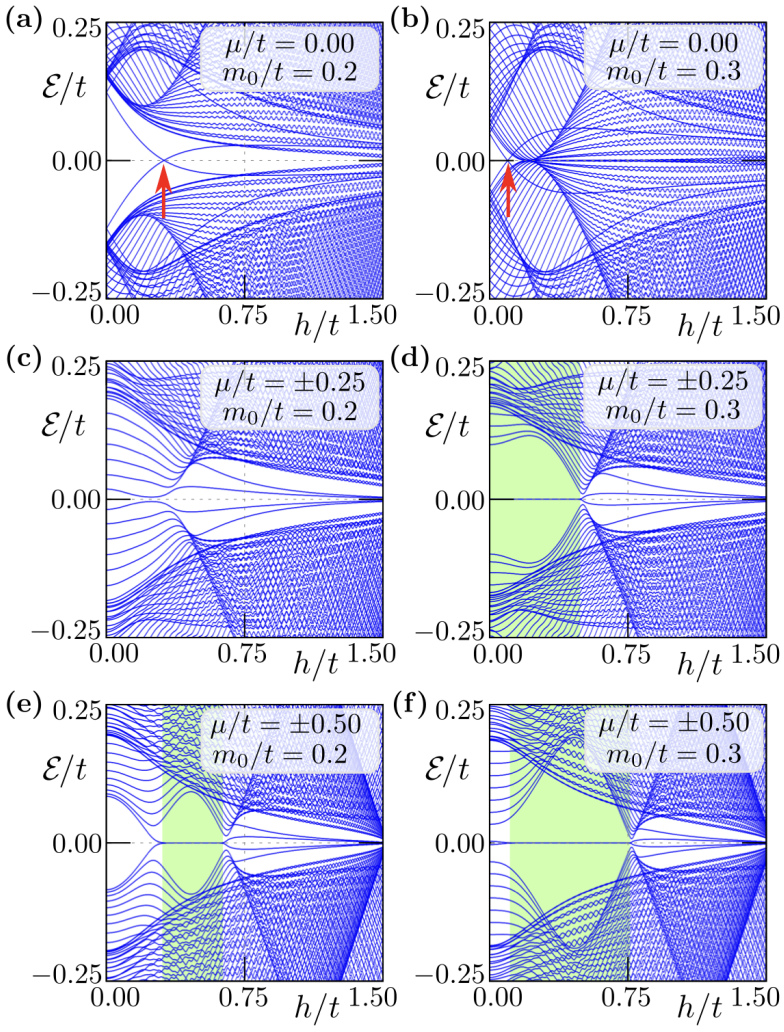

Figure 2.10: The panel depicts the energy spectrum of a finite nanowire with 200 sites. The superconducting order parameter $\Delta = 0.1\,t$ and SOC $\lambda = 0.15\,t$. The panel has been adopted from Ref. [67].

typical nanowire, the intrinsic spin-orbit interaction effectively couples the electron's spin to its momentum, leading to a helical band structure. When an external magnetic field is applied along the nanowire's axis, it introduces a Zeeman splitting that can, under specific conditions, invert the energy bands [c.f. Fig. 2.10(e) and (f)]. This band inversion is crucial for establishing the topological phase. Subsequently, by bringing this nanowire into intimate contact with a conventional s-wave superconductor, a superconducting energy gap is effectively induced in the nanowire through the proximity effect. The critical condition for the emergence of MBS occurs when the chemical potential of the nanowire lies within this induced superconducting gap, and the Zeeman energy surpasses a critical threshold determined by the induced gap and the strength of the spin-orbit coupling [c.f. Fig. 2.10(a),(c) and (d)]. In this precise regime, the system undergoes a topological phase transition, and a pair of

MBS are theoretically predicted to emerge and localize at the nanowire's ends.

These boundary states are the elusive Majoranas, characterized by their zero-energy nature meaning their energy lies precisely at the Fermi level, within the superconducting gap. Crucially, their topological origin endows them with robustness against local perturbations, making them resilient to disorder and noise that would typically decohere conventional quantum states. From the perspective of the local density of states (LDOS), the presence of MBS manifests as a sharp, quantized peak at zero energy, specifically at the ends of the topological segment. In an ideal scenario, this zero energy peak in the LDOS would correspond to a conductance peak of $2e^2/h$ in tunneling measurements, reflecting the unique Andreev reflection properties facilitated by the Majorana states. The spatial confinement of these zero-energy states to the boundaries, with an exponential decay into the bulk of the nanowire, is a direct consequence of the topological protection and a key characteristic for their experimental identification.

The diagonalization of Hamiltonian leads to the energy spectrum as shown in Fig. 2.10. The panel shows the effect magnetic field has on the energy spectrum. The magnetic field breaks the time reversal symmetry of the Hamiltonian which is necessary for the emergence of uncoupled Majorana modes. Ideally, Majorana zero modes at the ends of a topological superconductor are at exactly zero energy. However, due to their spatial overlap in finite nanowires, they can hybridize and develop a small energy splitting. This splitting can be influenced by the magnetic field. As the magnetic field is varied, the energy splitting between the Majorana modes can oscillate. If this splitting becomes significant, the modes are no longer at precisely zero energy, which can be seen as a form of unpairing from the ideal zero-energy state. The critical value of the magnetic field at which this topological phase transition occurs depends on other parameters such as the chemical potential and the induced superconducting gap. Furthermore, the orientation of the applied magnetic field relative to the nanowire and its SOC vector can also significantly influence the topological phase diagram. Therefore, both the magnitude and the direction of the magnetic field are crucial parameters in the theoretical and experimental investigation of topological superconductivity in 1D nanowires.

As shown in the Fig. 2.10(a) for a given strength of AFM ordering the energy bands cross the $\mathcal{E} = 0$ (marked by red arrow), but they do not lead to non trivial MBS. As seen in Fig. 2.10(c) and (e) that the Zeeman field closes the gap leading to MBS for a critical value of μ. As the Zeeman field is increased the gap reopens leading to trivial phase. The second column of Fig. 2.10 reaffirms this only for a higher value of m_0. One of the ways to visualize

these Majorana modes is to look at the local density of states in the BdG framework it is given as

$$\begin{aligned} \rho_{is}(\omega) &= -\frac{1}{\pi}\sum_{\sigma} \mathrm{Im}\langle c_{is\sigma}|(\omega - H)^{-1}|c^{\dagger}_{is\sigma}\rangle \\ &= -\frac{1}{\pi}\sum_{\sigma} \mathrm{Im}\mathrm{G}_{is\sigma}(\omega + \imath 0^{+}) \end{aligned} \tag{2.40}$$

A key experimental signature for the presence of Majorana bound states is the observation of a zero-bias conductance peak (ZBCP) in tunneling spectroscopy measurements. Theoretically, a quantized ZBCP with a conductance value of $2e^2/h$ is predicted when a single spin-polarized channel is available for tunneling into a Majorana mode [69]. This precise quantization stems from perfect Andreev reflection, a process where an electron incident from a normal metal lead is retro-reflected as a hole, simultaneously accompanied by the absorption of a Cooper pair by the superconductor. This mechanism is uniquely augmented by the presence of a zero-energy MBS.

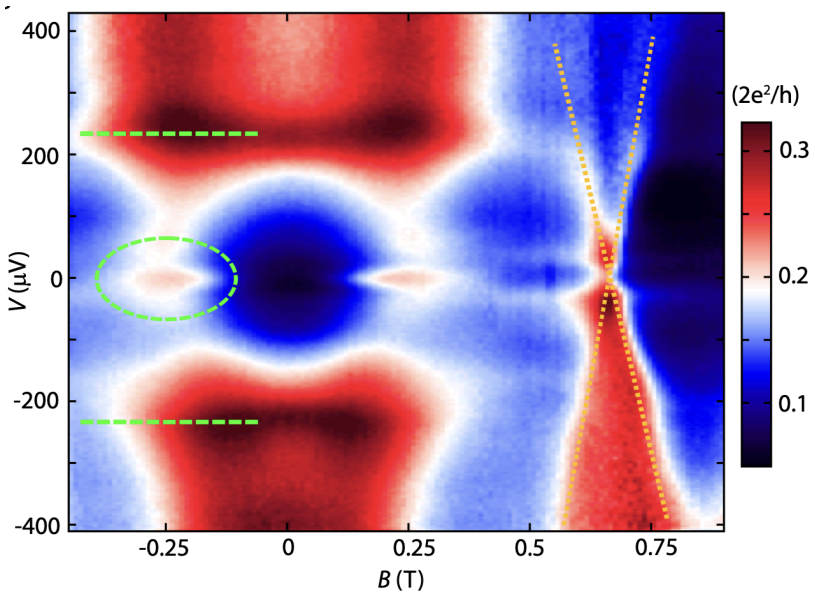

Figure 2.11: A contour plot of dI/dV for voltage V and magnetic field B. The green dashed circle shows the zero bias peak around ~ -0.25 T, additionally, the green lines are the gap edge states. The topologically trivial states appear at ~ 0.6 T, crossing the ZBP marked by yellow dashed lines. Adopted from Ref. [12].

In practical experimental observations, the ZBCP observed in nanowire devices displays several characteristic attributes that are indicative, though not conclusive, of MBS. These peaks frequently exhibit remarkable resilience to variations in gate voltage, suggesting that their zero energy character is largely insensitive to minor electrostatic potential fluctuations which is considered a hallmark anticipated for topologically protected states [52]. Mourik

et al. [12] marked a pivotal achievement with the initial observation of a robust ZBCP in InSb nanowires mounted on NbTiN a superconductor. The device architecture employed an InSb nanowire with superconducting contacts, and critically, a ZBCP emerged when the external magnetic field surpassed a specific threshold, hinting at a potential transition into a topological phase as shown in Fig. 2.11. Furthermore, the ZBCP typically diminishes above a critical magnetic field, which aligns with the theoretical phase diagram predicting the closure of the topological gap and the system's reversion to a trivial superconducting state as depicted by yellow dashed line in Fig. 2.11. The temperature dependence of the ZBCP also commonly adheres to anticipated scaling laws, with the peak amplitude decreasing as temperature rises, consistent with thermal broadening of a zero-energy state [70]. While these features are necessary conditions for MBS, they are, in isolation, insufficient to provide unequivocal confirmation of their topological origin. Deng et al. [71] offered deeper insights by designing a nanowire incorporating a deliberate quantum dot region. This configuration facilitated the exploration of quantum dot-Majorana hybridization, allowing the discrete energy levels of the quantum dot to be tuned into interaction with the putative MBS. Their key finding revealed the coalescence of Andreev bound states into a zero mode as the quantum dot level was brought into resonance, a behavior consistent with the formation of a Majorana state at the interface between the quantum dot and the topological superconducting segment. These compelling experiments, however, also underscored the inherent difficulties in unambiguously interpreting ZBCPs. The most formidable challenge lies in differentiating trivial explanations for ZBCPs from those of genuine topological origin. Disorder-induced Andreev bound states (ABS) can also appear at zero energy in conventional superconductors, particularly in the presence of impurities or structural inhomogeneities [72]. These zero-energy states can mimic the ZBCP characteristic of MBS, rendering their distinction paramount. Similarly, gradual confinement potentials at the ends of a finite-length superconducting wire can give rise to quasi Majorana states, which, while not topologically protected, can exhibit features resembling true MBS [73]. Additionally, prevalent trivial explanation, especially associated to devices integrating quantum dots, is the Kondo effect. In a quantum dot with an odd electron count, strong electron correlations can lead to a Kondo resonance at zero energy, which manifests as a ZBCP in tunneling spectroscopy [74]. Discriminating the Kondo effect from MBS necessitates meticulous analysis of temperature dependence, magnetic field response, and gate voltage characteristics.

Beyond the realm of nanowires, atomic chains assembled on superconducting surfaces have emerged as a highly promising alternative avenue for realizing and investigating MBS.

This approach offers distinct advantages, particularly concerning atomic-scale precision and direct spatial characterization. The fabrication protocols for these systems typically encompass two principal techniques: self assembly and atomic manipulation. Self assembly entails the controlled deposition of magnetic atoms, such as Fe or Co, onto a meticulously prepared superconducting surface, like Pb(110) or Nb. Under specific growth conditions, these magnetic atoms can spontaneously organize into 1D chains, driven by surface reconstruction and inter-atomic forces. Atomic manipulation, conversely, leverages the unparalleled precision of a STM tip to individually position magnetic atoms, enabling the construction of custom-designed chains with exquisite control over their length and geometric configuration. This degree of precision represents a significant advantage, facilitating the fine-tuning of system parameters. The STM serves not only as a fabrication instrument but also as the primary tool for elucidating the electronic properties of these atomic chains. The characteristic signatures of MBS in atomic chains are predominantly revealed through scanning tunneling spectroscopy (STS), which quantifies the local density of states. A key signature is the spatial localization of zero-energy states, consistently observed to be precisely confined to the ends of the magnetic chains [40]. This spatial confinement directly reflects the boundary conditions imposed by the topological phase. Furthermore, the distinctive decay of the Majorana wavefunction away from the chain terminals can be directly measured, typically conforming to an exponential decay modulated by an oscillatory term, $\psi(x) \sim e^{-x/\xi} \sin(k_F x)$, here ξ denotes the superconducting coherence length and k_F is the Fermi wavevector [75]. This unique spatial fingerprint aids in differentiating MBS from trivial states that may not exhibit such a well-defined decay profile. Spin polarization measurements, utilizing spin-resolved STM, provide supplementary validation by confirming the anticipated spin texture of the zero-energy states, further bolstering their Majorana character [76].

Several pivotal experiments have showcased the successful realization of MBS in atomic chains. Nadj-Perge et al. [40] reported the groundbreaking observation of zero-energy states at the ends of atomic Fe chains grown on a superconducting Pb(110) surface [42]. The central finding demonstrated clear spectroscopic peaks at zero energy, precisely localized at the chain extremities. Crucially, they provided corroboration through the length dependence of the state splitting: for finite chains, the two MBS at opposing ends hybridize, leading to a minute energy splitting that diminishes exponentially with chain length, a behavior consistent with theoretical predictions for MBS hybridization [77]. Subsequently, Ruby et al. [78] conducted subgap spectroscopy on Co chains on a superconducting surface, unveiling quantized conductance at the chain ends. They further presented vital control experiments by

comparing magnetic Co chains with non-magnetic counterparts, unequivocally demonstrating that the zero energy states emerged solely in the presence of magnetic ordering, thereby precluding trivial origins related to non-magnetic impurities or defects. The atomic chain platform offers several distinct advantages over semiconductor nanowires. Paramount among these is the atomic-scale precision in controlling the position and structure of the magnetic impurities, enabling meticulous engineering of the 1D system. Moreover, the utilization of STM facilitates direct spatial imaging and spectroscopy of the electronic states, furnishing a potent diagnostic capability that is challenging to implement in embedded nanowire heterostructures. This direct visualization capacity provides a compelling avenue to confirm the spatial localization and wave-function characteristics of MBS.

Chapter 3

Topological ladder

We discussed in previous chapter the physics of a 1D nanowire which enables MBS providing it topological robustness for the potential application in fault tolerant systems. We saw how Majorana quasiparticles in spinless fermion chain [4] can be extended to several spinfull systems of various kinds. Some of them are magnetic chains proximatized by a superconductor [55, 56, 77, 79–84]. Some recent setups proposed for the realization of the Majorana edge modes [30, 85, 86]. We saw how fabrication of nanowire by manipulating atoms to form the magnetic chain of Fe [40, 42, 76, 87–89] or Co [42] can be deposited on superconducting surface (like lead) to induce superconductivity.

In the superconducting chain in ambient of magnetic order, the topological phase can be induced by the external magnetic field [41, 90, 91]. In such situation, the increase of the external Zeeman field leads to closing of the trivial superconducting gap, and reopen "new" topological gap. Such setup can be mimicked by the magnetic order realized within chain, which in simplest case has form of the ferromagnetic (FM) order. Nevertheless, the realization of the topological phase is not limited to the ferromagnetic chains, but also can be realized in the presence of anitferromagnetic (AFM) order [67, 92]. The recent progress of the experimental techniques allow fabrication of the atomic chain via *atom-by-atom* engineering [89]. Magnetic order realized within ad-atom chain can be controlled e.g. by the relative position with respect to the surface atoms [93–96]. In such case, the topological phase depends strongly on the length of the chain [96, 97]. Moreover, in the general case non-collinear magnetic order can support manifestation of the topological phase due to the mimicked effect similar to the spin–orbit coupling [55, 56, 77, 79–84].

The compounds $BaFe_2S_3$ and $BaFe_2Se_3$ represent a unique class with a quasi 1D structure [98, 99]. These materials, which contain Fe-based "spin-ladders," offer a simplified platform for studying the intricate interplay between dimensionality, strong electronic cor-

relations, magnetism, and superconductivity. In this chapter we focus on the $BaFe_2Ch_3$ (Ch=S, Se) compounds [100]. The defining crystal structure consisting a double chains or ladder with the edges sharing FeS_4 or $FeSe_4$ tetrahedra intercalated with barium (Fig. 3.1). $BaFe_2S_3$ crystallizes in a base-centered orthorhombic structure with the $Cmcm$ space group, while $BaFe_2Se_3$ adopts a primitive orthorhombic structure with the $Pnma$ space group [101]. The primary structural difference arises from a tilting of the ladders in $BaFe_2Se_3$, which leads to an alternation of Fe-Fe distances along the chains, a feature absent in the more symmetric $BaFe_2S_3$ [102]. At room temperature, $BaFeSe_3$ exhibits multiferroic behaviour [103–105] and short range magnetic order [106, 107]. The most remarkable property of these compounds is the emergence of superconductivity under high hydrostatic pressure. External hydrostatic pressure leads to several structural phase transitions in both cases [102, 108–112]. In $BaFe_2S_3$, superconductivity with a critical temperature (T_c) up to 24 K is observed for pressures above 10 GPa [99]. Theoretical and experimental studies suggest that as pressure increases, the system undergoes an insulator to metal transition, and the magnetic moments are suppressed before superconductivity emerges from this non magnetic metallic state [102]. In $BaFe_2Se_3$, superconductivity is also induced under pressure (10.2-15 GPa), albeit with a lower T_c of around 10 K [113–115]. Intriguingly, superconductivity in this material appears to emerge directly from a magnetic phase where large local magnetic moments persist, only vanishing at much higher pressures ($\sim$ 30 GPa) [102, 113]. This indicates that the superconducting pairing in $BaFe_2Se_3$ may be catalyzed by magnetic fluctuations in a manner distinct from that of its sulfur counterpart.

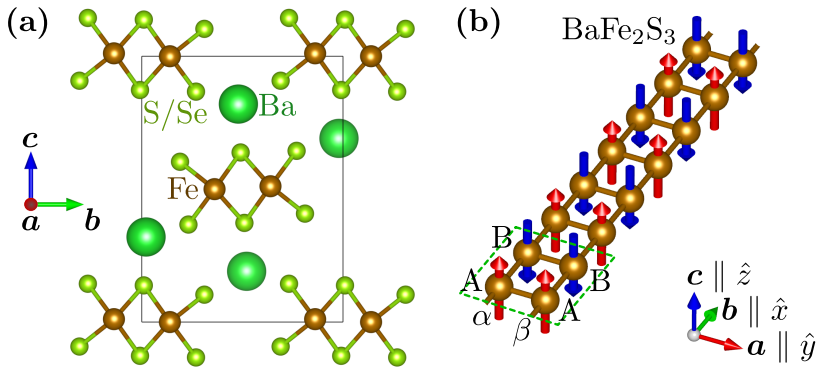

Figure 3.1: (a) Crystal structure of $BaFe_2Ch_3$ (Ch=S, Se) with $Pnma$ symmetry. (b) The iron ladder has a canonical (π,0) AFM-like order in $BaFe_2S_3$ hence the magnetic unit cell contain two pairs effectively forming our system.

At ambient pressure, both $BaFe_2S_3$ and $BaFe_2Se_3$ behave as Mott insulators [116, 117], a state where electron localization prevents electrical conduction despite an unfilled electronic band. This insulating behavior is intimately linked to their magnetic ground states. However,

their magnetic ordering is qualitatively different and provides them intriguing properties, like block spin magnetic order [113, 118, 119], driven by the correlation [120–122]. $BaFe_2S_3$ exhibits a stripe-type AFM order below its Néel temperature (T_N) of approximately 120 K, where spins are ferromagnetically aligned along the rungs of the ladder and antiferromagnetically along the legs [99]. Additionally, $BaFe_2Se_3$ shows a similar T_N of around 140 K and hosts an AFM order [123]. This magnetic state has also led to predictions and observations of multiferroicity in $BaFe_2Se_3$, a phenomenon where both magnetic and ferroelectric orders coexist [103]. Additionally, the magnetic order can be modified by the external hydrostatic pressure [111, 112, 124].

The magnetic order realized in $BaFe_2S_3$ and $BaFe_2Se_3$ corresponds to canonical $(\pi, 0)$ AFM-like order [see Fig. 3.1(b)]. The Fe ladder ties together with FM coupling between magnetic moments between the rungs coupling two chains ultimately forming the ladder, which then reflects the same magnetic moment orientation. Additionally, along the chains an AFM coupling is realized. In the case of $BaFe_2S_3$ the magnetic moment changes the orientation site-by-site [Fig. 3.1(b)], while in the $BaFe_2Se_3$ form the spin block with opposite magnetic moments (not presented).

Naturally, the presence of AFM-like orders within these ladder structures naturally prompts questions regarding the potential realization of topological phases. Motivated by this, our study here provides a comprehensive discussion of the topological properties of the magnetic ladder system. Previous theoretical investigations of antiferromagnetic chains have already revealed a rich topological phases [67]. In this context, additional topological regions can be realized in the phase diagram, which, under certain conditions, can lead to the emergence of a topological phase even in the presence of an extremely small magnetic field. Furthermore, a topological phase can be anticipated when the Fermi level is shifted away from the band edges. Here, we specifically focus on the ladder with an AFM-like order, such as that realized in $BaFe_2S_3$ [as presented on Fig. 3.1(b)].

3.1 Model and framework

In our study we investigate a theoretical model of a magnetic ladder characterized by an AFM-like magnetic order. The geometry of this system is visualized in Fig. 3.1(b). The structure consists of two parallel chains, labeled as α and β, lying in the xy-plane and aligned along the $\hat{x}$-direction. The magnetic unit cell contain two pairs of sites with opposite magnetic moment with spin $\uparrow$ and $\downarrow$, denoted by A and B, respectively. Additionally, we assume that the magnetic moments are located along $\hat{z}$. The electronic hopping within this

system is defined by two key pathways: intra-chain hopping along the $\hat{x}$-direction and inter-chain coupling, which connects the two chains along the $\hat{y}$-direction. The system can be described by the Hamiltonian:

$$H = H_0 + H_{AFM} + H_{SC}. \tag{3.1}$$

First term describes the kinetic energy of non-interacting electrons within the ladder and is given by

$$\begin{aligned} H_0 \;=\; & \sum_{\substack{i,j,s,s' \\ w,w',\sigma}} \Big[-t - (\mu + \sigma\, h)\delta_{ij}\delta_{ss'}\delta_{ww'} - t_\perp \delta_{ij}\delta_{ss'} \Big] c^\dagger_{isw\sigma} c_{jsw'\sigma} \\ & - \sum_{\substack{ij \\ w\sigma\sigma'}} \imath\lambda \left(c^\dagger_{iAw\sigma}\sigma^y_{\sigma,\sigma'} c_{iBw\sigma'} + c^\dagger_{iBw\sigma}\sigma^y_{\sigma,\sigma'} c_{i+1Aw\sigma'} + \text{h.c.} \right) \\ & - \sum_{\substack{isw \\ w'\sigma\sigma'}} \imath\eta \left(c^\dagger_{isw\sigma}\sigma^x_{\sigma\sigma'} c_{isw'\sigma'} + c_{isw'\sigma'}\sigma^x_{\sigma\sigma'} c^\dagger_{isw\sigma} \right). \end{aligned} \tag{3.2}$$

Here, $c_{isw\sigma}$ ($c^\dagger_{isw\sigma}$) denotes the annihilation (creation) operator of electron with spin σ in sth site of wth wire in ith unit cell, and h.c. stands for the Hermitian conjugate. The parameters μ and h denotes the chemical potential and external magnetic field, respectively. The hopping parameters are defined as follows: t is the intra-chain hopping integral along the $\hat{x}$-direction, which defines the kinetic energy of electrons moving along a single ladder leg. For simplification, this parameter is used as the energy unit for the entire system. The inter-chain hopping integral, $t_\perp$, couples the two parallel chains of the ladder along the $\hat{y}$-direction, enabling electron transport across the rungs. The chemical potential, μ, controls the total electron filling of the system and, consequently, the position of the Fermi level. An external magnetic field, h, is assumed to be oriented along the $\hat{z}$-direction and couples to the spin of the electrons, with the spin index $\sigma = \pm 1$ representing the two spin projections. Finally, the coefficients for Rashba spin-orbit couplings (SOCs) along the $\hat{x}$ and $\hat{y}$ directions are denoted by λ and η, respectively. These terms introduce a coupling between the electron's spin and its momentum. By adjusting the relative values of these hopping and SOC parameters, our model can effectively navigate between a regime of weakly coupled wires and one where the wires are strongly coupled. Second term H_{AFM} describes the on-site interaction of electrons with the AFM order, which naturally introduces two non-equivalent sublattices (A and B)

with opposite magnetic moments. This term is defined as:

$$H_{AFM} = -m_0 \sum_{iw\sigma} \sigma \left(c^\dagger_{iAw\sigma} c_{iAw\sigma} - c^\dagger_{iBw\sigma} c_{iBw\sigma} \right). \tag{3.3}$$

Here, m_0 corresponds to the magnitude of the magnetic moments. Finally, last term H_{SC} represents the superconducting state induced within the ladder. This is assumed to arise from a proximity effect with a neighboring ordinary superconductor. The term is taken to have a BCS-like form, describing an s-wave pairing potential:

$$H_{SC} = \Delta \sum_{isw} (c^\dagger_{isw\uparrow} c^\dagger_{isw\downarrow} + c_{isw\downarrow} c_{isw\uparrow}), \tag{3.4}$$

where Δ denote superconducting order parameter. To facilitate the analysis of this system, we employ a periodic boundary condition and transform the Hamiltonian into momentum space using a Fourier transform. The creation and annihilation operators are transformed as follows:

$$c^\dagger_{isw\sigma} = \frac{1}{\sqrt{N}} \sum_k \exp\left(-\imath \boldsymbol{k} \cdot \boldsymbol{R}_{is}\right) c^\dagger_{ksw\sigma}, \qquad \text{and} \qquad c_{isw\sigma} = \frac{1}{\sqrt{N}} \sum_k \exp\left(\imath \boldsymbol{k} \cdot \boldsymbol{R}_{is}\right) c_{ksw\sigma} \tag{3.5}$$

where $c_{ksw\sigma}$ ($c^\dagger_{ksw\sigma}$) denotes the annihilation (creation) operator of electron with momentum k in sth magnetic sublattice of wth wire, while N denotes number of states. The presence of four sites per magnetic unit cell necessitates the folding of the Brillouin Zone, restricting the momentum vector to the range $k \in [-\pi/2, \pi/2)$. In momentum space appropriate terms of the Hamiltonian can be rewrite as:

$$\begin{aligned} H_0 = & \sum_{kw\sigma} \mathcal{E}_k \left(c^\dagger_{kAw\sigma} c_{kBw\sigma} + \text{h.c.} \right) - \sum_{ks\sigma} t_\perp \left(c^\dagger_{ks\alpha\sigma} c_{ks\beta\sigma} + \text{h.c.} \right) - \sum_{ksw\sigma} (\mu + \sigma h) c^\dagger_{ksw\sigma} c_{ksw\sigma} \\ & + \sum_{kw\sigma\sigma'} \imath \mathcal{L}_k \, c^\dagger_{kAw\sigma} \sigma^y_{\sigma\sigma'} c_{kBw\sigma'} + \text{h.c.} - \sum_{\substack{ksw \\ w'\sigma\sigma'}} \imath\eta \, c^\dagger_{ksw\sigma} \sigma^x_{\sigma\sigma'} c_{ksw'\sigma'} + \text{h.c.}, \end{aligned} \tag{3.6}$$

$$H_{AFM} = -m_0 \sum_{kw\sigma} \sigma (c^\dagger_{kAw\sigma} c_{kAw\sigma} - c^\dagger_{kBw\sigma} c_{kBw\sigma}), \tag{3.7}$$

$$H_{SC} = \Delta \sum_{ksw} (c^\dagger_{ksw\uparrow} c^\dagger_{-ksw\downarrow} + c_{-ksw\downarrow} c_{ksw\uparrow}). \tag{3.8}$$

Here, $\mathcal{E}_k = -2t \cos k$, and $\mathcal{L}_k = -2\imath \sin k$. As we can see, presented model can be also interpreted as two-orbital (α and β wires) system with hybridization $t_\perp$ and η between orbitals

at the same (A and B) sites. In this perspective, the inter-chain hopping parameter, $t_\perp$, and the Rashba SOC term, η, act as hybridization terms that couple these two orbitals at the same A and B sites. This dual interpretation offers a valuable alternative for understanding the system's band structure and electronic properties.

To analyze the topological properties of the system, we express the Hamiltonian in the basis of a tensor product of four Pauli matrices. This formalism allows us to compactly represent the various degrees of freedom of the system namely, particle-hole, sublattice, wire, and spin. Specifically, we use a basis where the Pauli matrix τ acts on the particle-hole subspace, ρ acts on the sublattice subspace, ν acts on the wire subspace, and σ acts on the spin subspace. In such a representation the Hamiltonian is given by

$$H = \sum_k \psi_k^\dagger \mathbb{H}_k \psi_k, \tag{3.9}$$

where $\mathbb{H}_k$ is the Hamiltonian in the matrix form for momentum k, while $\psi_k^\dagger$ is the Nambu vector for such a representation given by:

$$\begin{aligned} \psi_k^\dagger &= \Big(c_{kA\alpha\uparrow}^\dagger \; c_{kA\alpha\downarrow}^\dagger \; c_{kA\beta\uparrow}^\dagger \; c_{kA\beta\downarrow}^\dagger \; c_{kB\alpha\uparrow}^\dagger \; c_{kB\alpha\downarrow}^\dagger \; c_{kB\beta\uparrow}^\dagger \; c_{kB\beta\downarrow}^\dagger \\ &\quad c_{-kA\alpha\uparrow} \; c_{-kA\alpha\downarrow} \; c_{-kA\beta\uparrow} \; c_{-kA\beta\downarrow} \; c_{-kB\alpha\uparrow} \; c_{-kB\alpha\downarrow} \; c_{-kB\beta\uparrow} \; c_{-kB\beta\downarrow}\Big). \end{aligned} \tag{3.10}$$

This approach facilitates the application of the BdG formalism to obtain the energy spectrum and to identify topological phase transitions. The Hamiltonian in matrix form can be represented as:

$$\begin{aligned} \mathbb{H}_k &= \mathcal{E}_k \tau^3\rho^1\nu^0\sigma^0 - t_\perp \tau^3\rho^0\nu^1\sigma^0 - \mu\tau^3\rho^0\nu^0\sigma^0 - h\tau^3\rho^0\nu^0\sigma^3 \\ &+ \imath\mathcal{L}_k\tau^3\rho^1\nu^0\sigma^2 + \eta\tau^3\rho^0\nu^2\sigma^1 - \Delta\tau^2\rho^0\nu^0\sigma^2 - m_0\tau^3\rho^3\nu^0\sigma^3 \end{aligned} \tag{3.11}$$

The superscript labels which range from 0 to 3 for all subspaces represent the identity, x, y, and z Pauli matrices respectively in their respective subspaces.

Having established the BdG Hamiltonian for the nanowire, we now turn our attention to the fundamental symmetries it possesses. These symmetries are essential for understanding the system's topological properties it manifests. The first key symmetry is the particle-hole symmetry, which is an intrinsic property of the BdG formalism. This symmetry is described by an antiunitary operator, $\mathcal{P}$, which can be expressed as $\mathcal{P} = \tau^1\rho^0\nu^0\sigma^0\mathcal{K}$, here $\mathcal{K}$ is the

complex conjugation operator. This operator acts on the Hamiltonian,

$$\mathcal{P}^{-1}\mathbb{H}_k\mathcal{P} \quad = \quad -\mathbb{H}_{-k}. \tag{3.12}$$

In addition to particle-hole symmetry, the Hamiltonian exhibits a pseudo time reversal symmetry say $\mathcal{T}$. The pseudo time reversal symmetry is given by an antiunitary operator $\mathcal{T} = \tau^0\rho^0\nu^1\sigma^0\mathcal{K}$ and its action on the Hamiltonian is given by

$$\mathcal{T}^{-1}\mathbb{H}_k\mathcal{T} \quad = \quad \mathbb{H}_{-k}. \tag{3.13}$$

Ultimately, the combination of the particle-hole and pseudo time reversal symmetries gives rise to chiral symmetry given by $\mathcal{C} = \mathcal{P}\mathcal{T}$ having a unitary representation.

3.2 Topological phase

To probe the topological properties of the system, we can now employ a $\mathbb{Z}$ topological invariant, specifically the winding number, as demonstrated in previous studies [64]. This invariant classifies the different topological phases of the system. To facilitate the calculation of the winding number, the Hamiltonian must be brought into a block off-diagonal form via a unitary transformation. This transformation, $\mathcal{U} = \exp(i\frac{\pi}{4}\tau^3)\rho^0\nu^0\sigma^0$ re-organizes the Hamiltonian as:

$$\mathbb{H}_k \quad = \quad \begin{pmatrix} 0 & \mathcal{A}(k) \\ \mathcal{A}^\dagger(-k) & 0 \end{pmatrix}. \tag{3.14}$$

The winding number, which is an integer value, can then be computed by integrating the determinant of the off-diagonal block $\mathcal{A}(k)$ over the Brillouin Zone:

$$w = \frac{1}{2\pi\imath}\int_{k=-\frac{\pi}{2}}^{k=\frac{\pi}{2}} \frac{dz_k}{z_k} \tag{3.15}$$

here $z_k = \mathrm{Det}(\mathcal{A})$, The matrix $\mathcal{A}(k)$ is an 8×8 matrix in the sublattice, wire, and spin basis, and its structure is given by:

$$\begin{aligned} \mathcal{A}(k) \quad = \quad & \mathcal{E}_k\rho^1\nu^0\sigma^0 - t_\perp\rho^0\nu^1\sigma^0 - \mu\rho^0\nu^0\sigma^0 - h\rho^0\nu^0\sigma^3 \\ & +\imath\mathcal{L}_k\rho^1\nu^0\sigma^2 + \eta\rho^0\nu^2\sigma^1 - m_0\rho^3\nu^0\sigma^3 + \imath\Delta\rho^0\nu^0\sigma^2 \end{aligned} \tag{3.16}$$

The winding number is evaluated using the determinant of $\mathcal{A}(k)$. Because the determinant of a matrix is invariant under a change of basis, the winding number itself is independent of the specific basis chosen for the representation. This inherent invariance provides the freedom to transform the system into a more convenient basis. We can rewrite $\mathcal{A}(k)$ in a different basis as follows

$$\begin{aligned}\mathcal{A}(k) &= \left(\mathcal{E}_k\rho^1\sigma^0 + \imath\mathcal{L}_k\rho^1\sigma^2 - \mu\rho^0\sigma^0 - h\rho^0\sigma^3 - m_0\rho^3\sigma^3 + \imath\Delta\rho^0\sigma^2\right)\nu^0 \\ &\quad -t_\perp\rho^0\sigma^0\nu^1 + \eta\rho^0\sigma^1\nu^2 \qquad (3.17)\\ &= \mathcal{A}_0(k)\nu^0 - t_\perp\rho^0\sigma^0\nu^1 + \eta\rho^0\sigma^1\nu^2 \qquad (3.18)\end{aligned}$$

here $\mathcal{A}_0(k)$ is the off diagonal term of the block Hamiltonian of a single nanowire as extensively studied by [67]. $det(\mathcal{A})$ can be expressed in terms of $\mathcal{A}_0$ by applying the properties of block-diagonal matrices

$$\det(\mathcal{A}) = \det(\mathcal{A}_0)\det[\mathcal{A}_0 - (t_\perp^2 + \eta^2)\,T\mathcal{A}_0^{-1}T^\dagger] \qquad (3.19)$$

This expression can be rearranged by applying the property $\det(A)\det(B) = \det(AB)$, which combines the terms and yields:

$$\det(\mathcal{A}) = \det[\mathcal{A}_0^2 - (t_\perp^2 + \eta^2)\,\mathcal{A}_0T\mathcal{A}_0^{-1}T^\dagger] \qquad (3.20)$$

here the operator T is defined as $T = (-t_\perp\rho^0\sigma^0 - \imath\eta\rho^0\sigma^1)/\sqrt{t_\perp^2 + \eta^2}$. To eliminate the computationally intensive inverse term $\mathcal{A}_0^{-1}$ we can rearrange and arrive at an alternate form. By utilizing the fact that $T^\dagger T = \rho^0\sigma^0$ which gives us the follow:

$$\det(\mathcal{A}) = \det[\mathcal{A}_0T^\dagger\mathcal{A}_0T - (t_\perp^2 + \eta^2)] \qquad (3.21)$$

This identity provides a simplified and more efficient expression for calculating the determinant. Beyond the computational advantages, this form reveals deeper physical consequences. To illustrate this, consider the case where the wires are coupled kinetically and the SOC along the rung is absent i.e. $\eta = 0$. This simplification yields

$$\begin{aligned}\det(\mathcal{A}) &= \det[\mathcal{A}_0^2 - t_\perp^2] \qquad (3.22)\\ &= \det(\mathcal{A}_0 - t_\perp)\det(\mathcal{A}_0 + t_\perp) \qquad (3.23)\\ &= \det(\mathcal{A}_0(\mu - t_\perp))\det(\mathcal{A}_0(\mu + t_\perp)) \qquad (3.24)\end{aligned}$$

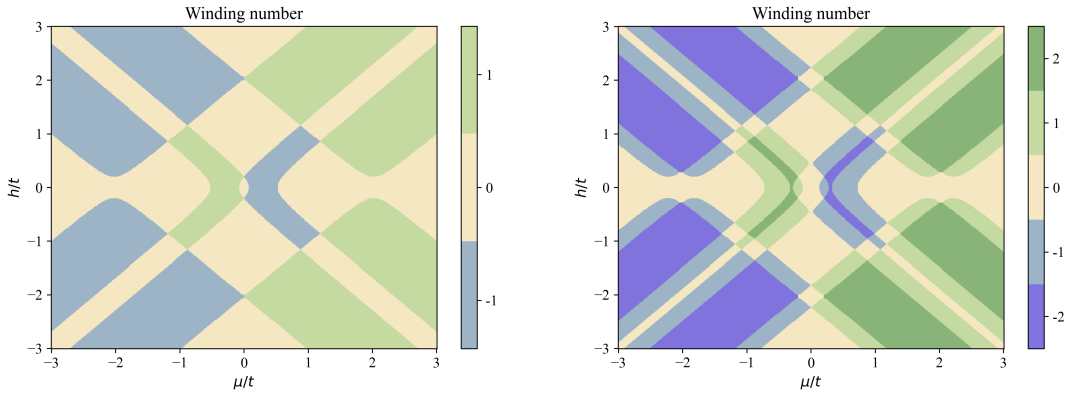

(a) (b)

Figure 3.2: Comparison of topological phase of (a) the Rashba nanowire [67] and (b) the ladder system. Results presented are for $m_0 = -0.3t$, $\lambda = -0.15t$, and $\Delta = -0.15t$, and (b) the ladder has $t_\perp = 0.2t$ and $\eta = 0.2\lambda$ resulting in the weakly coupled nanowires.

This result implies that the winding number for ladder is composition of winding number of two separate nanowires with shifted chemical potential. Consequently, topological phase for $\eta = 0$ is a superimposed topological phase of two nanowires, enabling the ladder to host topological phases with winding number greater than $|\pm 1|$.

The topological phase of ladder quickly diverges from this additive behavior as η takes any non zero value. Fig. 3.2(a) shows the phase diagram of a topological nanowire and Fig. 3.2(b) is the topological phase for the ladder system with identical parameters as nanowire with a $t_\perp = 0.2t$ and $\eta = 0.2\lambda$ (which is $0.03t$). The linearity in the composition of the determinants starts showing up in the topological phase of ladder even with this small η as can be seen as thinned stripes of winding number corresponding to -2 in Fig. 3.2(b) near $h = 0$ extending outwards with slope ± 1. The phase diagram begins to show substantial differences with changes in the parameters. One such natural choice is to couple the nanowires as strongly as the rungs are i.e. $t = t_\perp$ and $\lambda = \eta$. The results shown in Fig. 3.3(a) has no marquee feature of nanowire except for the parabolic region with topological phase ± 1. Interestingly, the phase diagram has these seeming artifact which appears to be like a hairline scratch around $h \approx \pm 1$. A closer examination of this region reveals the region having an intricate boundary and is topological in nature with winding number ± 3 as shown in Fig. 3.4(a). The region of ± 3 winding number is not restricted for these parameters, infact for a relatively small Δ the phase diagram shows an more pronounced regions with winding number ± 3 as shown in Fig. 3.3(b). Note that coupling is still quite small and as shown in Fig. 3.4(b) which is a closeup of region with winding number -3, still hosts the rectilinear boundaries between the topological and trivial region similar to single nanowire.

Naturally, we probe the topological phase space with a varying Δ. Fig. 3.5(a) is the prepared with choice of parameters so that is cuts across the topological phase presented in Fig. 3.2(b) at $h = 0.5t$. The phase diagram reveals two separate lobes of topological region. Each of them hosting regions with winding number ± 2 which in itself is predominantly due super imposed regions (as η is small). It is clear from phase diagram that as $|\Delta|$ increases beyond a certain value [c.f. Fig. 3.5] the rest of the parameters are no longer sufficient and the topological regions are henceforth bounded. Fig. 3.5(b) shows the topological phase in the absence of magnetic field. The circular regions move closer as the magnetic field is reduced. These phase diagrams collectively paints a picture of $\mu - h - \Delta$ phase volume where topologically rich regions for $|h| < 0.5t$ are tube like structure which get distorted and move apart. Additionally, changing the strength of magnetic moment m_0 introduces isolated small regions with winding number ± 2 as shown in the inset of Fig. 3.5(b). To better understand the effect of the AFM order and the regions with winding number ± 3, we slice across $h = -0.975t$ in Fig. 3.3(a) which passes through region with winding number -3. Fig. 3.6(a) shows a fascinating landscape of topologically non trivial regions even for $m_0 = 0$. Unlike previous results, Fig. 3.6(a) for the first time provides a substantially larger regions with winding number ± 3. Albeit, the boundary of these region is sometimes not smooth and composed of fringe like patterns as shown in Fig. 3.6(b).

Lastly we probe the effects of magnetic field and the region with winding number ± 3 while varying m_0. In doing so we slice across Fig. 3.3(a) at $\mu = 0.3t$ shown in Fig. 3.7(a) and across $\mu = -0.9t$ shown in Fig. 3.7(b). Evidently, even in the regime of coupling with $t = t_\perp$ and $\lambda = \eta$ the region with winding number ± 3 only appear for a specific value of magnetic

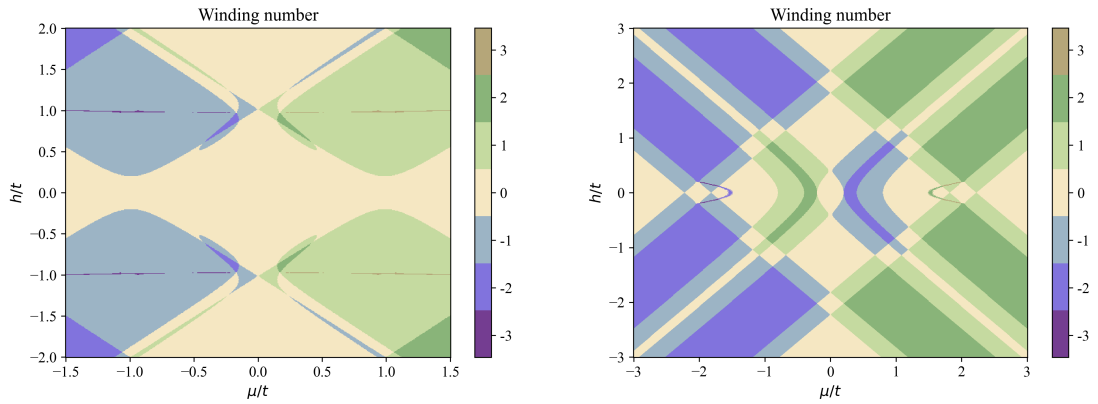

(a) (b)

Figure 3.3: Topological phase for (a) the ladder with $t = t_\perp$ and $\lambda = \eta$ leading to strongly coupled chains alongwith $m_0 = -0.1t$, and $\Delta = -0.15t$. (b) Topological phase of ladder with weakly coupled chains with same parameters as Fig. 3.2 and $\Delta = -0.0015t$.

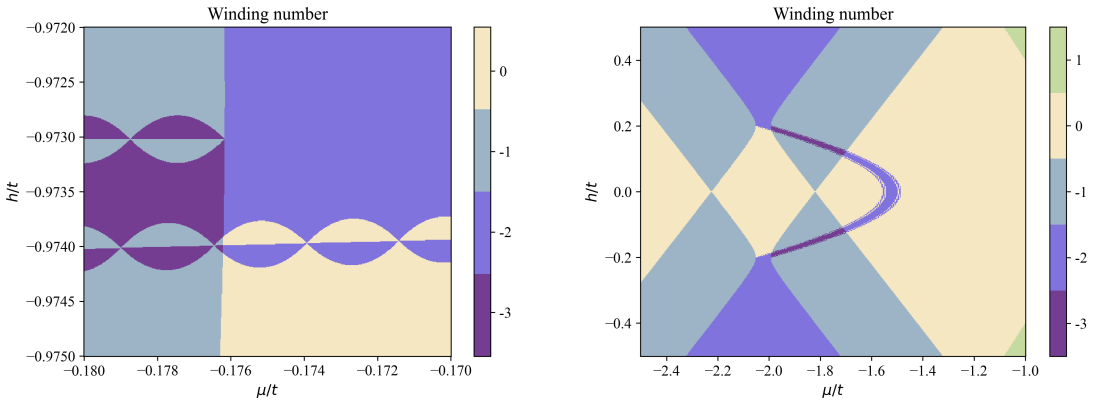

(a) (b)

Figure 3.4: A close up of the topological phase presented in Fig. 3.3.(a) Shows the boundary between trivial and non-trivial topological phase around $\mu \sim 0.175t$, and $h \sim 0.97t$. (b) On the other hand shows a clear boundary of topological phase, with a pocket of region with winding number -3 from Fig. 3.3(b).

field. This sliver of h gets wider as $|\mu|$ is increased along with m_0. Collectively, based on our observations the topological phase has ± 3 regions but for a specific and small window of magnetic field. Although this region can be inflated using other parameters, the value of magnetic field remains very crucial.

3.3 Probing the finite system

The theoretical study of finite nanowires is an indispensable component which serves as the crucial bridge between abstract topological theory and the tangible reality of experimental observation [62]. While idealized models of infinitely long wires provide the foundational

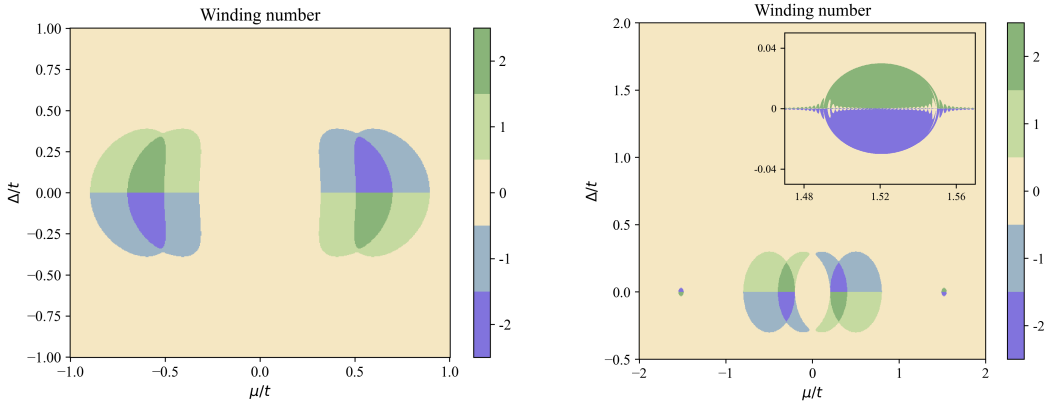

(a) (b)

Figure 3.5: Cross section of topological phase presented in Fig. 3.3(b) along (a) $h = 0.5t$, and $h = 0$.

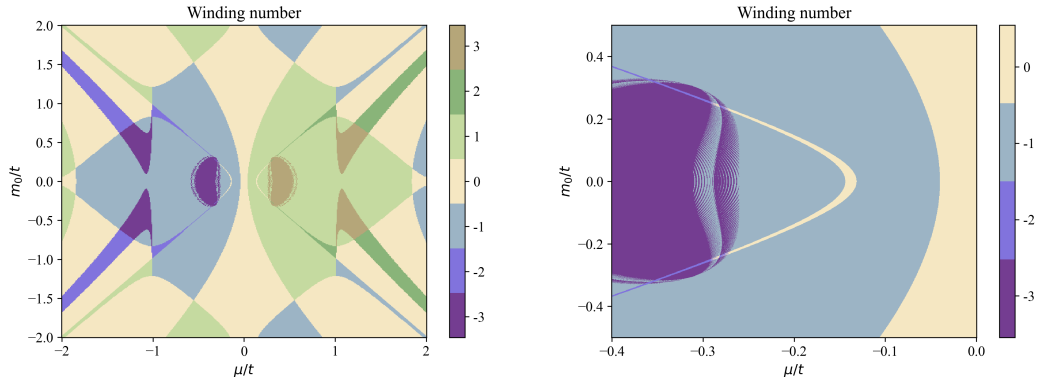

(a) (b)

Figure 3.6: The panel displays winding number for μ vs. m_0 and (b) provides a closer look at the intricate fringes like pattern from $\mu \in (0.4t, 0t)$ and $\Delta \in (-0.5t, 0.5t)$ of topological phase shown in (a). The parameters have been chosen such that $t_\perp = t$, $h = -0.975$, $\Delta = -0.2t$, and $\lambda = \eta = -0.15t$

understanding of topological phases and the conditions for hosting Majorana fermions, they are inherently limited in their ability to predict the specific, measurable signatures required for experimental verification. Experimental devices are, by their nature, finite and subject to a host of real world constraints such as boundary effects, material inhomogeneity, and disorder. Consequently, theoretical frameworks that account for these finite size properties are essential not only for interpreting experimental data but also for guiding the very design of the experiments themselves.

The core motivation for modeling finite system stems from a fundamental discrepancy between theory and practice. The prediction of topological phase, where a gapped bulk state hosts zero energy modes at the system's boundaries, is a key consequence of infinite system

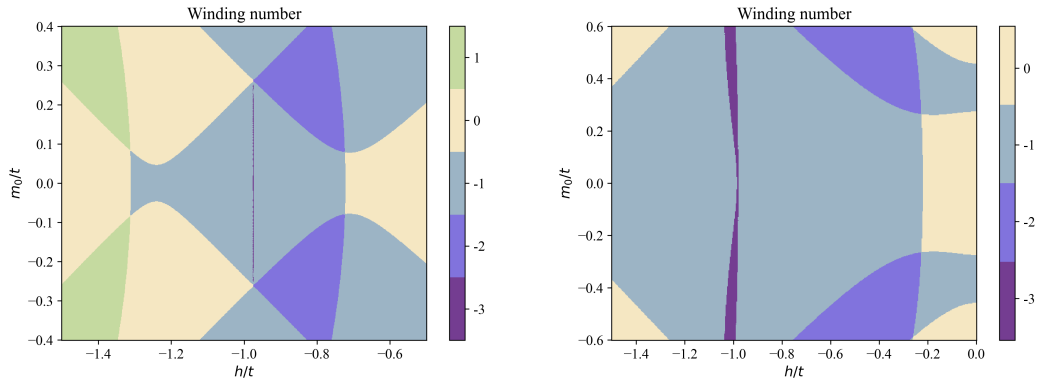

(a) (b)

Figure 3.7: The topological for h vs. m_0 for different range. The parameters have been chosen such that $t_\perp = t$, $\Delta = -0.2t$, $\lambda = \eta = -0.15t$, (a) $\mu = -0.3$, and (b) $\mu = -0.9$

theory. In such a model, the Majorana bound states are truly degenerate at exactly zero energy. However, any real nanowire has a finite length, and the Majorana fermions localized at opposite ends of the wire are not completely decoupled. They exhibit a small but finite wave function overlap, leading to a minute energy splitting. This effect, known as Majorana hybridization, causes the zero energy modes to split into two states at a minuscule non zero energy [58]. This splitting is a direct consequence of the wire's finite length and is a key prediction that an infinite model cannot capture. The theoretical calculation of this splitting as a function of wire length and other parameters provides a direct, quantitative target for experimentalists, who must resolve these tiny energy scales to confirm the topological nature of the observed states.

Beyond simply predicting signatures, finite theoretical models are indispensable for helping experimentalists distinguish genuine Majorana signatures from other, more conventional, zero energy states. Real world devices are never perfect and contain disorder, impurities, and quantum dot states that can also give rise to zero energy peaks in the conductance spectrum, leading to trivial zero energy modes [12]. By including disorder and realistic geometries in their simulations, theorists can study how these trivial zero modes behave compared to their topological counterparts. For example, a shorter nanowire will exhibit a more easily measurable energy splitting between the Majorana modes, while in a longer wire, the splitting is exponentially suppressed, making the modes appear to be at zero energy [58]. The theoretical predictions of these distinct behaviors provide a vital framework for interpreting ambiguous experimental data and confidently identifying the topological origin of a zero bias anomaly.

In previous sections we saw how periodic boundary condition for the ladder gave topologically diverse characteristics. We now focus our attention to study the finite ladder with open boundary conditions. The emergence of topology in a finite system is a direct consequence of the bulk-boundary correspondence. As it states that the topological properties of the bulk material predict the existence of protected, gapless states at its boundaries. In our case, the ladder's ends act as physical "domain walls" between the topologically non-trivial bulk and the surrounding topologically trivial vacuum. We use fermionic operators γ_n and $\gamma_n^\dagger$ to diagonalize the real space Hamiltonian using $c_{isw\sigma} = \sum_n (u^n_{isw\sigma}\gamma_n - \sigma v^{n*}_{isw\sigma}\gamma_n^\dagger)$. This transformation leads to a real space BdG equations given as

$$\mathbb{H}\Psi \quad = \quad \mathcal{E}\Psi \tag{3.25}$$

The BdG Hamiltonian which describes the entire ladder with N number of rungs. This structure accounts for both the ladder's spatial arrangement and the system's internal symmetries,

such as spin and sublattice degrees of freedom. The Hamiltonian takes a block diagonal form which is given by following form

$$\mathbb{H} = \begin{pmatrix} H_0 - \mu\mathbb{I}_{4N} & \mathbf{\Delta} \\ \mathbf{\Delta}^T & -H_0^* + \mu\mathbb{I}_{4N} \end{pmatrix} \tag{3.26}$$

here $\mathbb{I}_{4N}$ is the identity matrix of size $4N \times 4N$. The block H_0 and $\mathbf{\Delta}$ are themselves of a block diagonal structure. H_0 assumes a tri block diagonal form where each diagonal block ($D_\pm$ of size 4×4) describes ith rung and assuming sublattice ordering to be A, B, $\cdots$ the hamiltonian block is given as follows

$$H_0 = \begin{pmatrix} D_+ & T & 0 & \cdots & 0 \\ T^\dagger & D_- & T & \cdots & 0 \\ 0 & T^\dagger & D_+ & \cdots & 0 \\ \vdots & \vdots & \vdots & \ddots & \vdots \\ 0 & 0 & 0 & \cdots & \cdot \end{pmatrix} \tag{3.27}$$

since the Hamiltonian accounts for the each sublattice A and B as separate sites in its structure, the block $D_\pm = -h\,\nu^0\sigma^3 \mp m_0\,\nu^0\sigma^3$. As previously, ν and σ describe the wire and spin subspace of the system. Additionally, $T = -t\,\nu^0\sigma^0 - t_\perp\,\nu^1\sigma^0 - \imath\lambda\,\nu^0\sigma^1 - \eta\,\nu^2\sigma^1$, and $\mathbf{\Delta} = \imath\Delta\,\mathbb{I}_N\,\nu^0\sigma^2$.

The solution to the eigenvalue problem gives us the energy spectrum of the ladder for the chosen number of sites i.e. rungs. We choose a ladder with 201 sites/rungs which follows the sublattice sequence $A\ B\ A\ \cdots\ A$. We exactly diagonalize the Hamiltonian which gives the energy spectra for system, to obtain the bound states we vary the magnetic field and the chemical potential as shown in Fig. 3.8. The energy spectrum of the system is gapped identically for all the cases as evident from Fig. 3.8. The energy spectra can be clearly divided into two regions which are specifically identified by the absence of the zero energy modes and the presence of zero energy modes as the energy gap closes.

Closing of the superconducting gap is the pivotal event that separates the trivial and topological phases. As the tuning parameter (h for Fig. 3.8(a)-(b), and μ in Fig. 3.8(c)-(d)) is varied, the bulk quasiparticle energy gap closes completely to zero at the critical point. This closing of the gap is not just a spectral feature; it is at this value the system's topological invariant changes. Thus we designate the region with the superconducting band gap as trivial and the gap closing marks the beginning of topological region. Fig. 3.8(a) starts out with an energy gap which decreases with the Zeeman field. Before the gap closes, the system is in a

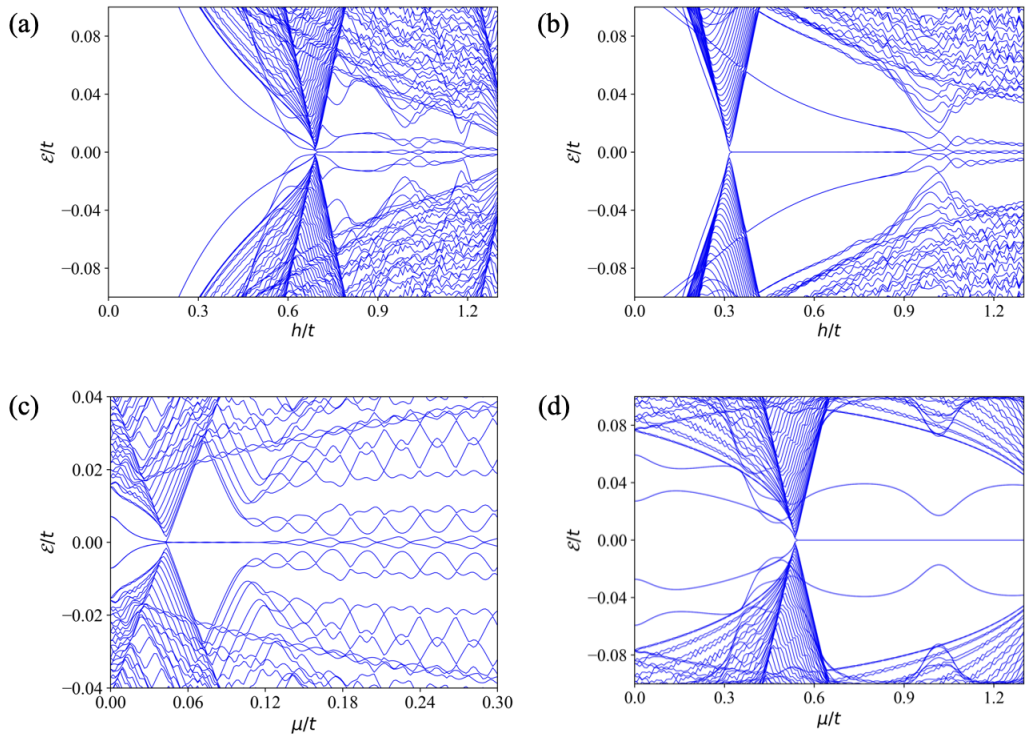

Figure 3.8: Energy spectrum for 201 rungs in the ladder. The parameters have been choosen such that $m_0 = 0.1t$, $\lambda = \eta = 0.15t$, $\Delta = 0.2t$, $t_\perp = t = -1$, (a) $\mu = 0.3335t$, (b) $\mu = -0.75t$, (c) $h = -0.9745t$, and (d) $h = -0.5t$.

trivial superconducting state with a finite gap with the topological invariant being 0. The two smallest positive energy levels are degenerate in the trivial region and as the magnetic field is increased the overall spectrum squeezes around the critical point (near $h/t \sim 0.69$ for Fig. 3.8(a)). The spectrum hereafter transitions from trivial to topological by virtue of formation of degenerate energy modes at zero energy. The system enters the topological phase. The topological invariant becomes 1. This change allows for the creation of the zero energy edge modes. In this gapped region these zero energy modes are cocooned by a pair of degenerate energy modes in some cases. These in gap energy modes are called the Andreev bound states (ABS) [44, 71, 125, 126]. In a conventional superconductor, electrons can't exist at a specific energy level (the "superconducting gap"). However, if a defect, an interface or a boundary is present, some quasiparticles can become trapped at that location these are the ABS. They are formed from a superposition of an electron and a hole, and they exist at an energy within the superconducting gap. In the ladder system placed in proximity to a superconductor, ABS can form at the ends of the ladder. This happens due to the proximity effect. The energy of these states is not zero but is tunable by external parameters like a magnetic field (Fig. 3.8(a) and (b)) or gate voltage, which change the chemical potential (Fig. 3.8(c) and (d)). These states are not just generic bound states; they are a direct

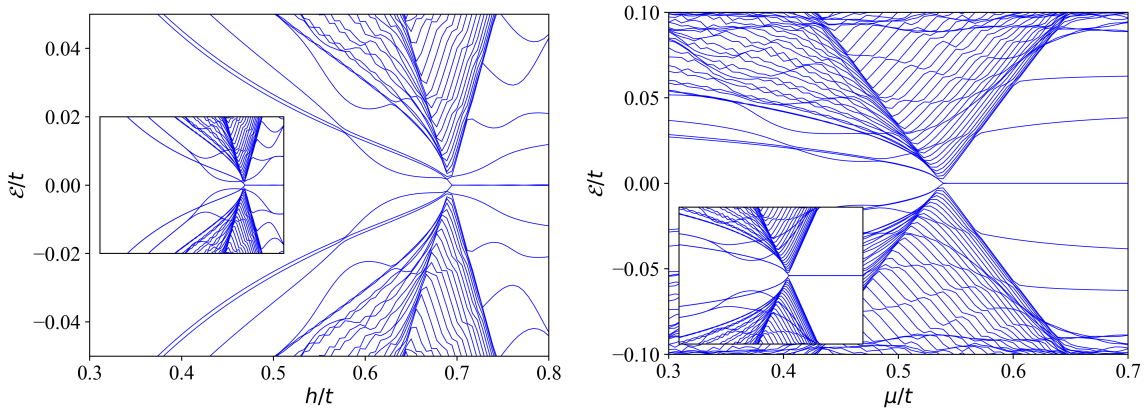

(a) (b)

Figure 3.9: Energy spectrum for 202 rungs in the ladder, the inset plot shows the spectrum for a Hamiltonian corresponding to 201 sites. The parameters have been choosen such that $m_0 = -0.1t$, $\lambda = \eta = -0.15t$, $\Delta = -0.2t$, $t_\perp = t = -1$, (a) $\mu = 0.3335t$, and (b) $h = -0.5t$.

consequence of the interplay between the semiconducting and superconducting properties at the ladder's boundaries, and their behavior is a key indicator of the topological phase transition to come. ABS themselves are not topologically protected. This means that under the change of parameters like the magnetic field or chemical potential, the energy of the ABS will shift. In a topological superconductor, two ABS, one at each end of a 1D system, can become a single, coherent pair of zero-energy states forming the MZM.

We now discuss the ladder system with even number of sites/rungs resulting in a sequence $A\ B\ A\ \cdots\ B$. Energy spectra for even number of sites (here we choose 202) is shown in Fig. 3.9]. The ladder with odd number of rungs sometimes had two pairs of degenerate modes within the superconducting gap. Changing the ladder from odd rungs to even rungs lifts this degeneracy pointing to the degeneracy resulting from the geometry of the ladder. Explaining the degeneracy requires further understanding of how the symmetry of ladder transform after the introduction of superconductivity. The degeneracy in the limit where $N \to \infty$ leads to non-trivial topological phase, which prevents from comment on the topological protection of such modes in finite limit.

The Local Density of States (LDOS), a quantity typically measured with a STM, serves as a crucial experimental probe for detecting MZM and confirming their topological characteristics. The LDOS is a measure of the number of available electronic states at a particular energy and spatial position within a material. The solution to the eigenvalue problem provides us a direct way to calculate the LDOS which can be formulated in terms of the eigenvectors using

the following form

$$\rho_{isw} = -\frac{1}{\pi}\sum_{\sigma} \mathrm{Im}\, G_{isw\sigma}(\omega + \imath 0^{+}) \tag{3.28}$$

$$= \sum_{n} \rho^{n}_{isw} = \sum_{n\sigma}[|u^{n}_{iswo}|^{2}\delta(\omega - \mathcal{E}_{n}) + |v^{n}_{iswo}|^{2}\delta(\omega + \mathcal{E}_{n})] \tag{3.29}$$

here i numerates the site on either wire hence alternating between sublattice A, B and δ is the Dirac delta function. G is the Greens function defined as $\langle c_{iswo}|(\omega - H)^{-1}|c^{\dagger}_{iswo}\rangle$

We now turn our attention towards the LDOS which will shine light on the nature of the states and their behaviour under different conditions. We plot the LDOS evaluated using Eq. 3.29 which has two sublattices and two wires. To make comparison natural we plot the LDOS for both wires on the same plot. LDOS of wire β is inverted and place below LDOS for wire α as shown in Fig. 3.10.

Fig. 3.10(a) and (b) depicts the LDOS for trivial region of the spectrum of Fig. 3.9(b).

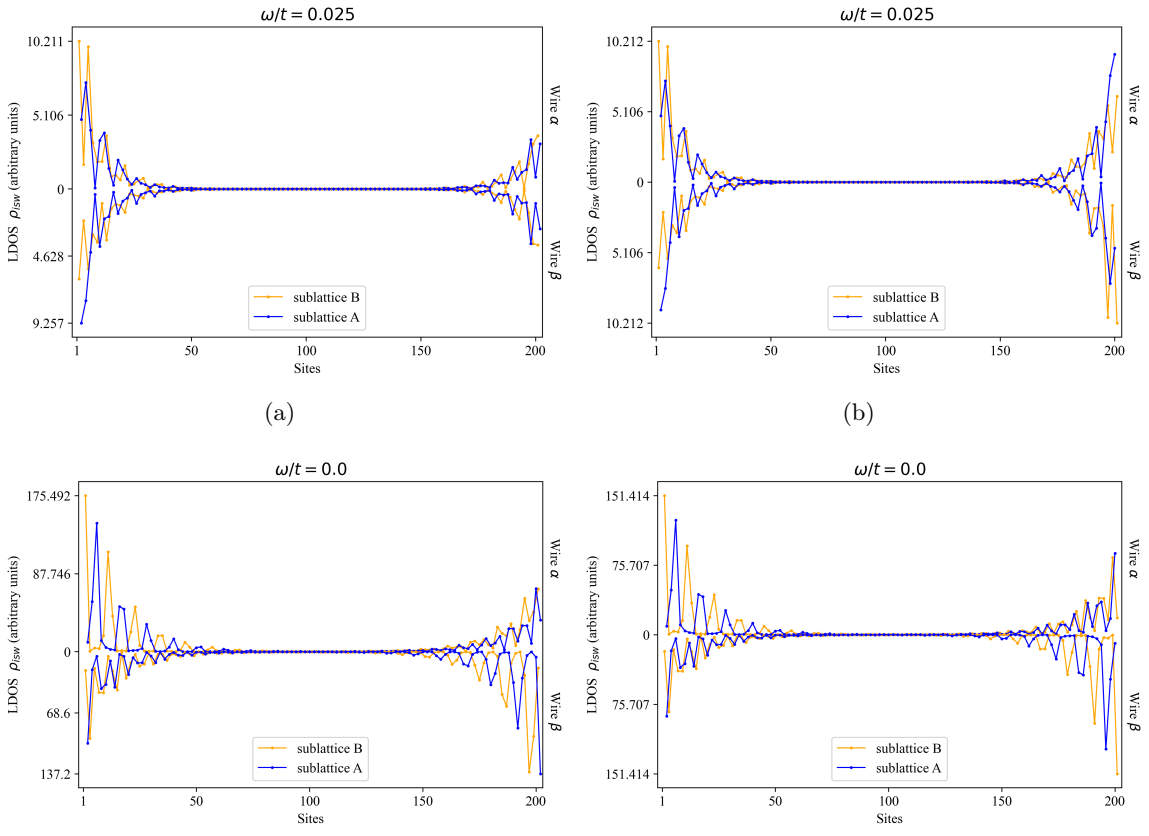

Figure 3.10: LDOS for even (left column) and odd (right column) number of rungs in the ladder. (a)-(b)The LDOS is calculated for energy spectrum shown in Fig. 3.9(b) at $\mu = -0.35t$. The LDOS is calculated in the trivial region of the spectra around or at the degenrate energy level i.e. $\omega = \pm 0.025t$. (c)-(d) Show the LDOS for the MBS for Fig. 3.9(a) for $h = -0.8t$.

While Fig. 3.10(c) and (d) are the LDOS for the topological region for the MZM in Fig. 3.8(a). We immediately note that the LDOS is not symmetric for the even number of rungs. On the other hand, LDOS for the odd number of rungs is symmetric under inversion. To be specific the LDOS for wire α is related to LDOS for wire β by inversion. This is the result of the accidental inversion invariance we discussed earlier.

In this chapter we presented our results for the quasi 1D system $BaFe_2S_3$. We model the molecule with two coupled nanowire(s) forming a ladder. We study the topological properties of the ladder with proximated s-type superconductivity along with a antiferromagnetic order in both nanowire in presence of a Rashba spin-orbit coupling and external Zeeman field. We find that in weakly coupled regime where the chains are not strongly coupled the topological phase of the ladder can be determined by superimposing the topological phase of single nanowire with shifted chemical potential. This linear superimposition falls off and non-linearity takes over as the coupling between the chains is increased. This gives rise to topological phase with winding number ± 3. For a finite number of rungs the ladder hosts Majorana bound states for topologically non-trivial regions found for the infinite chain. There appear additional degenerate modes in the finite ladder which extend beyond the superconducting gap. The nature of these degenrate modes remains to be understood.

Chapter 4

Bulk topological materials

In 2D and 3D, topological insulators are compelling due to their bulk-boundary correspondence, where robust edge modes or surface states emerge as manifestations of topological invariants. The field of topological materials emerged from profound developments in quantum Hall physics, laying the foundation for understanding topological insulators. The quantum Hall effect (QHE), discovered in 1980, demonstrated quantized Hall conductance in 2D electron systems subjected to strong magnetic fields. This phenomenon revealed the critical role of topology in electronic systems. Von Klitzing's observation of precisely quantized Hall plateaus which led to the Nobel Prize and marked a paradigm shift in condensed matter physics.

A key theoretical breakthrough came with the work of Thouless, Kohmoto, Nightingale, and Nijs (TKNN) in 1982 [3], who established a connection between the quantized Hall conductance and a topological invariant, now known as the TKNN invariant or the first Chern number. The TKNN invariant is an integer derived from the Berry curvature of electronic states over the Brillouin zone, encapsulating the global geometric properties of the wavefunctions. This provided a topological explanation for the robustness of the quantized Hall conductance against disorder and impurities.

The IQHE and its fractional counterpart FQHE sparked interest in identifying systems where topological phases could arise without an external magnetic field. Theoretical predictions by Haldane in 1988 demonstrated that a 2D lattice model with complex next-nearest-neighbor hopping could exhibit a quantized Hall effect in the absence of an external field. This conceptually paved the way for time-reversal-invariant systems, leading to the prediction and subsequent discovery of topological insulators [127, 128].

In 2005, Kane and Mele proposed a groundbreaking model for a 2D topological insulator based on graphene, incorporating spin-orbit coupling. They predicted the existence of the

QSHE, characterized by helical edge states protected by time-reversal symmetry. Experimental confirmation soon followed in HgTe/CdTe quantum wells [18], where the unique edge transport properties were observed.

3D topological insulators, such as BiSe [129] and BiTe [130], were subsequently discovered, showcasing insulating bulk behavior with conducting surface states. These materials exhibit spin-momentum-locked surface states described by Dirac-like Hamiltonians, which are protected against backscattering and localization by time-reversal symmetry. The bulk-boundary correspondence, a hallmark of topological phases, ensures the existence of these surface states as a consequence of nontrivial bulk topology.

Experimental techniques such as ARPES and STM have been instrumental in visualizing the surface states of 3D topological insulators. Furthermore, transport measurements have demonstrated their unique properties, including the suppression of backscattering and quantized magnetoelectric effects. The field of topological insulators has since expanded into a broader study of topological phases of matter, including higher-dimensional systems, superconductors, and semimetals. Connections to Dirac and WSM, which host gapless excitations protected by topology, highlight the unifying framework of topology in quantum materials.

In this chapter we will lay the foundation for the study of topological insulators which will lead the pathway to introduce the Dirac and Weyl semimetals. We will begin with the topological invariant (Sec. 4.1) itself with the use of standard mathematical tools like Berry's curvature e.t.c (Sec. 4.1.1) along with its nuanced application in Sec. 4.1.2 which will be applied to a two level toy model in Sec. 4.1.3. Starting with graphene and its prevelent models in Sec. 4.2.1, we will make our way to models for topological insulators in Sec. 4.2.2-4.2.3, and eventually introduce the semimetals in Sec. 4.2.4. Finally, we will study the most vital consequences of the topological insulators and the semimetals in Sec. 4.3.

4.1 Emergence of topological invariant

In crystalline solids, the periodicity of the lattice imposes a periodic structure on the electronic wavefunctions, leading to the natural definition of momentum space, or reciprocal space. For 2D materials, the momentum space is topologically equivalent to a torus, while for 3D materials, it forms a higher-dimensional analogue of a torus. Importantly, momentum space can serve as the parameter space for the eigenstates of the Hamiltonian. These eigenstates, or wavefunctions, are defined at every point in momentum space, forming a vector bundle. It is the topology of this vector bundle which encodes the system's physical properties and is captured by topological invariants. We employ the concept of Berry curvature,

which is the local vector field from which the Berry phase is derived. Analogous to the way a magnetic field's integral gives magnetic flux, the integral of the Berry curvature over a closed surface in the parameter space (like the Brillouin zone) yields the total Berry phase. These concepts provide the means to asses a material's topology: adiabatic dynamics creates the conditions for the Berry phase to emerge, and the Berry curvature provides the mathematical tool to calculate the topological invariant that classifies the material and predicts the existence of protected edge states via the bulk-boundary correspondence.

4.1.1 Berry's gadgets

Consider a material with a space translation symmetry which allows for the momentum space description of the system with a Hamiltonian $H(\boldsymbol{k})$, where $\boldsymbol{k}$ is the momentum in the crystal (serving as the parameter space). Let $|\psi_n(\boldsymbol{k})\rangle$ be the eigenstates corresponding to the nth eigen-energy state

$$H(\boldsymbol{k})|\psi_n(\boldsymbol{k})\rangle = E_n(\boldsymbol{k})|\psi_n(\boldsymbol{k})\rangle\,. \tag{4.1}$$

An eigenstate with a particular index (or energy level) varies as the momentum varies. For each momenta the solution to the above eigenvalue equation gives a local vector space of eigenstates. In general as a momentum is varied these vector spaces do not have to share any characteristics. Nevertheless, its the local behavior of parameter space that is, continuity which allows a comparison of wavefunction as the underlying parameter is varied.

Consider a closed path through the parameter space, one would think that as the momenta is varied along the closed path we would arrive at the same value of the wavefunction as we complete traversing the loop. As quantum mechanics has showed time and time again nothing is ever so straightforward. The above could be true but never a necessity, as seen we saw in the Chapter 1, where it was the magnetic field which caused a phase shift. There are numerous experimental results which violate the above. To verify the above we need to develop some tools namely, an object which can measure the change in phase as one changes the parameters. As we are interested in the behavior of the eigenstates as the momentum is varied. This can be achieved by following

$$A_{ni}(\boldsymbol{k})|\psi_n(\boldsymbol{k})\rangle = \imath\partial_{k_i}|\psi_n(\boldsymbol{k})\rangle \tag{4.2}$$

$$A_{ni}(\boldsymbol{k}) = \imath\langle\psi_n(\boldsymbol{k})|\partial_{k_i}\psi_n(\boldsymbol{k})\rangle\,. \tag{4.3}$$

This quantity is formally known as Berry connection. A_{ni} is the ith component of $\boldsymbol{A}_n$ forming

a vector field defined over the momentum space. The form of Berry connection makes it clear that loosely speaking it measures the phase that the eigenstate acquires over an infinitesimal change in momentum. This makes it gauge dependent, under a phase transformation $|\psi_n(\boldsymbol{k})\rangle \to e^{-\imath\phi(\boldsymbol{k})}|\psi_n(\boldsymbol{k})$, the Berry connection transforms as

$$A_{ni}(\boldsymbol{k}) \quad \to \quad A_{ni}(\boldsymbol{k}) - \imath\, \partial_{k_i}\phi(\boldsymbol{k})\,. \tag{4.4}$$

Consider a 2D crystal which leads to 2D momentum space (generalization to 3D is natural). A quantity can be defined which measures the accumulation of the Berry connection as we move along a closed path Σ enclosing region Γ in momentum space for a band labeled by n. Formally called Berry phase this can be mathematically written as follow

$$\gamma_n = \int_\Sigma \boldsymbol{A}_n(\boldsymbol{k}) \cdot d\boldsymbol{k}\,, \tag{4.5}$$

$$\gamma_n = \int_\Gamma (\nabla \times \boldsymbol{A}_n(\boldsymbol{k})) \cdot \hat{k}\; d^2\boldsymbol{k} \tag{4.6}$$

here, $\hat{k}$ unit vector along Γ. Additionally, $\boldsymbol{A}_n$ is the Berry connection for the nth band. As the path Σ is a closed one, the Berry phase forms a gauge invariant quantity. It is customary to define the curl of Berry connection as Berry curvature $\boldsymbol{\Omega}_n(\boldsymbol{k}) = \nabla \times \boldsymbol{A}_n(\boldsymbol{k})$. It follows immediately from the definitions that Berry curvature forms another vector field defined over the momentum space like Berry connection. Unlike the Berry connection, Berry curvature is a gauge invariant vector field. Naturally, the Berry curvature can be shown to have different forms,

$$\boldsymbol{\Omega}_n = \nabla \times \boldsymbol{A}_n \tag{4.7}$$

$$\boldsymbol{\Omega}_n = \imath\nabla \times \langle\psi_n|\nabla\psi_n\rangle = \imath\langle\nabla\psi_n| \times |\nabla\psi_n\rangle \tag{4.8}$$

$$= \imath \sum_{m\neq n} \langle\nabla\psi_n|\psi_m\rangle \times \langle\psi_m|\nabla\psi_n\rangle \tag{4.9}$$

using the chain rule on the time independent eigenvalue equation for the energy eigenstates we get $\langle\psi_m|\nabla\psi_n\rangle = \langle\psi_m|\nabla H|\psi_n\rangle/(E_n - E_m)$. Consequently,

$$\boldsymbol{\Omega}_n = \imath \sum_{m\neq n} \frac{\langle\psi_n|\nabla H|\psi_m\rangle \times \langle\psi_m|\nabla H|\psi_n\rangle}{(E_m - E_n)^2}\,. \tag{4.10}$$

Before we move forward we address some subtleties. It is clear that the Berry phase is a quantity which is only well defined modulo 2π. Considering the fact that Berry curvature is gauge invariant and Berry connection is not, the application of Stokes theorem in Eq. 4.6

only makes sense for certain gauge. The condition for the choice of gauge for the phase of $|\psi_n\rangle$ should be such that it is smooth everywhere within the region Γ including the boundary Σ. The poles of the Berry curvature are specific points, typically found at high-symmetry points in the BZ, where the curvature becomes singular or diverges. These points are often associated with degeneracies in the energy bands (when $E_m = E_n$). The topological properties of a material are encoded in the integral of this Berry phase over the entire BZ. The integral of the Berry curvature gives a quantized integer called the Chern number, a topological invariant. This invariant is a direct consequence of the presence of these Berry curvature monopoles (or poles). As long as the system remains gapped, these poles cannot simply disappear or change their total flux, ensuring the Chern number remains an integer. This robustness is the defining feature of a topological phase of matter.

The concept of parallel transport provides an intuitive way to understand the geometric nature of the Berry phase. Consider a vector placed on the surface of a sphere. Now as we slowly "parallel transport" this vector along a closed path. For instance, starting at the equator, move north to the pole, turn and move along a line of longitude, and finally return along a third line of latitude to the starting point. When the vector returns, it will have rotated relative to its original orientation, even though we tried to keep it "parallel" at every point. This rotation is a direct consequence of the curvature of the sphere's surface.

In a quantum system, the eigenstate acts as the vector, and the parameter space (e.g., the BZ) is the curved surface. When the system's parameters are slowly varied, the quantum state is parallel transported along certain path. The Berry phase is precisely this geometric angle of rotation that the quantum state acquires after completing a closed loop. The Berry curvature is the local measure of this 'quantum curvature' of the parameter space. A non-zero total Berry phase around a closed loop indicates a non-trivial curvature of the quantum state's parameter space, which is the underlying geometric origin of topology in quantum systems.

4.1.2 Adiabatic dynamics

In the previous section we reviewed tools that allow us to quantify the change of the phase of the wavefunction as the underlying parameters namely, momentum is smoothly altered. Although powerful this does not describe the complete picture, in this section we will examine 'parameter space' and its 'smooth change' with more care and generality. Consider a Hamiltonian describing a physical system with P, real parameters, $\boldsymbol{\lambda} = (\lambda_1, \cdots, \lambda_P)$. The

time-independent eigenvalue equation now reads as

$$H(\boldsymbol{\lambda})|n(\boldsymbol{\lambda})\rangle \;=\; E_n(\boldsymbol{\lambda})|n(\boldsymbol{\lambda})\rangle. \tag{4.11}$$

Here, as before $E_n(\boldsymbol{\lambda})$ are the energy levels and we assume a system such that they are non degenerate for all $\boldsymbol{\lambda}$. We need to choose the gauge for all levels, which must undergo a smooth transition as we vary $\boldsymbol{\lambda}$. The time-dependent Schrodinger equation on the other hand dictates the wavefunction $|\psi_n(t)\rangle$ to follow

$$H(\boldsymbol{\lambda}(t))|\psi_n(t)\rangle \;=\; \imath\frac{\partial}{\partial t}|\psi_n(t)\rangle\,. \tag{4.12}$$

We assume that time t varies from $0 \to T$, and the corresponding variation in parameters $\boldsymbol{\lambda}(t)$ is 'slow'. To be precise, it must be small compared to the frequencies corresponding to the energy gaps. This adiabatic approximation gives us the recipe for the ansatz for the time-dependent wavefunction which read

$$|\psi_n(t)\rangle \;=\; e^{\imath\gamma_n(t)}\, e^{-\imath\int_0^t E_n(\boldsymbol{\lambda}(\tau))d\tau}|n(\boldsymbol{\lambda}(t))\rangle \tag{4.13}$$

here, $|n(\boldsymbol{\lambda}(t))\rangle$ are the eigenstates of the time-dependent equation at time t. $\boldsymbol{\lambda}(t)$ is a directed curve in the parameter space whose rate change allows for the application of the adiabatic approximation. The phase $\gamma_n(t)$ satisfies the following equation

$$\frac{d}{dt}\gamma_n \;=\; \imath\langle n(\boldsymbol{\lambda})|\frac{d}{dt}|n(\boldsymbol{\lambda}(t))\rangle \tag{4.14}$$

$$\frac{d}{dt}\gamma_n \;=\; \imath\frac{d\boldsymbol{\lambda}}{dt}\langle n(\boldsymbol{\lambda})|\nabla_{\boldsymbol{\lambda}} n(\boldsymbol{\lambda})\rangle \tag{4.15}$$

$$\gamma_n \;=\; \int dt\frac{d\boldsymbol{\lambda}}{dt}\boldsymbol{A}_n(\boldsymbol{\lambda}) = \int_\Sigma d\boldsymbol{\lambda}\cdot\boldsymbol{A}_n(\boldsymbol{\lambda})\,. \tag{4.16}$$

This is a remarkable result which says that the phase appearing in the time-dependent wave function is independent of the rate at which the path is traversed in the parameter space. Moreover, it only depends upon the path traced in the parameter space and hence the time evolution phase only needs to be augmented with the Berry phase in the parameter space. Although the phase of wavefunction is quantity usually not associated with observable(s) of the system. The Berry phase is a measurable quantity the experimental setups usually use the interference of wavefunctions which traverse opposite paths in parameter space.

The adiabatic evolution is generalized by focusing on the entire degenerate manifold of states. Instead of focusing on the evolution of a single eigenstate, the system evolves within

the multi-dimensional subspace. The resulting geometric phase is no longer a simple scalar but a unitary matrix, known as the non-Abelian Berry phase. We will not discuss the generalization any further as it is beyond the scope of this thesis.

4.1.3 Two-level system

We will analyze a toy model with two energy eigenstates, to understand how and where topology arises in bulk system. The Hamiltonian describing such a two level system can always be represented in Pauli basis i.e. $\sigma = (\sigma_0, \sigma_x, \sigma_y, \sigma_z)$ and given by

$$H(\boldsymbol{k}) \quad = \quad \boldsymbol{d}(\boldsymbol{k}) \cdot \sigma \tag{4.17}$$

here, $\boldsymbol{d}(\boldsymbol{k})$ are the coefficient of Pauli basis, which we will be addressing as the pseudo spin basis. We simplify the situation further by assuming a 2D system where $d_0 = 0$, $d_x = k_x$, $d_y = k_y$, and $d_z = m$. The energy eigenvalues for this system are given by

$$E_{\pm} \quad = \quad \pm\sqrt{m^2 + k_x^2 + k_y^2}\,. \tag{4.18}$$

We further perform a change of variables for the ease of handling and a more elegant representation, $d = \sqrt{m^2 + k_x^2 + k_y^2}$, $m = d\,\cos\theta$, $k_x = d\,\sin\theta\,\cos\phi$, and $k_y = d\,\sin\theta\,\sin\phi$. Here, $\theta \in \{0,\, \pi\}$, $\phi \in \{0,\, 2\pi\}$ and it is evident that $d \geq 0$. The eigenvectors can be chosen such that

$$\psi_+ = \begin{pmatrix} \cos\frac{\theta}{2} \\ e^{\imath\phi}\sin\frac{\theta}{2} \end{pmatrix}, \qquad \text{and} \qquad \psi_- = \begin{pmatrix} e^{-\imath\phi}\sin\frac{\theta}{2} \\ -\cos\frac{\theta}{2} \end{pmatrix}. \tag{4.19}$$

In terms of the introduced spherical polar variables the eigenvalues are $\pm d$ and it is natural to identify the variables $(\theta,\, \phi)$ with a point on the surface of a 3D sphere. The spin-1/2 degree of freedom for a real space spin can be represented using Pauli matrices σ, it is natural to ask if the Hamiltonian at all describes such a degree of freedom. The answer of this question lies in time reversal symmetry, specifically, the Hamiltonian must be invariant under time reversal symmetry. The time reversal operator is given by

$$\mathcal{T} \quad = \quad \imath\,\sigma_y\,K \tag{4.20}$$

here, K is the charge conjugation operator.

$$\mathcal{T}H(\boldsymbol{k})\mathcal{T}^{\dagger} \quad \neq \quad H(-\boldsymbol{k}) \tag{4.21}$$

the Hamiltonian does not preserves the time reversal symmetry and a non-zero m is the reason for the breaking of time reversal symmetry. The Hamiltonian describes a fermion and owing to the broken time reversal symmetry the fermion described is not a quasiparticle with real spin-1/2 but a pseudo-spin. The Hamiltonian becomes time-reversal only for $k_x = k_y = 0$, and $m = 0$ consequently, the fermion is too. The energy dispersion becomes degenerate at this same point as we will soon learn there is much more to it.

We employ the tools we derived in previous section namely, Berry connection and Berry curvature. We will calculate the Berry connection first and for a given value of m we find that

$$\begin{aligned} \boldsymbol{A}_{\pm} &= (A_d,\, A_\theta,\, A_\phi) && (4.22)\\ &= \imath \left\langle \psi_{\pm} \middle| \left(0,\, \frac{1}{d\,\sin\theta}\frac{\partial}{\partial\theta}\sin\theta,\, \frac{1}{d\,\sin\theta}\frac{\partial}{\partial\phi}\right) \middle| \psi_{\pm} \right\rangle && (4.23) \end{aligned}$$

Consequently, we get

$$\boldsymbol{A}_{\pm} = \mp\frac{1}{2d}\,\tan\frac{\theta}{2}\,\hat{\boldsymbol{\phi}} \tag{4.24}$$

and the Berry curvature is given by

$$\boldsymbol{\Omega}_{\pm} = \mp\frac{\hat{\boldsymbol{d}}}{2d^2}\,. \tag{4.25}$$

We immediately note that both connection and curvature have poles at $d = 0$ for which we must have $m = 0$. Moreover, the energy spectrum has a degeneracy and the Hamiltonian is invariant under the time reversal symmetry at this momenta. As the materials are 2D following our discussion from previous section, we can evaluate the Berry phase over the entire momentum space for a non-zero m

$$\begin{aligned} \gamma_{\pm} &= \mp\int \frac{d\boldsymbol{S}\cdot\hat{\boldsymbol{d}}}{2d^2}\\ &= \mp\int d\phi\, dk\, k\, \frac{m}{2(k^2+m^2)^{\frac{3}{2}}}\\ &= -\pi\,\mathrm{sgn}(m) && (4.26) \end{aligned}$$

It is evident from above that the Berry phase over the entire momentum space comes in two variety based on the sign of m. In a periodic system, this integral over the entire Brillouin zone is refereed as the Chern number of the system. The fermion described by the Hamiltonian for m has a time reversal partner at $-m$, hence they are separated in parameter

space. When $m = 0$ things change and the Hamiltonian can potentially host either of the fermions, and we will see in later sections how this plays into a condensed matter system.

4.2 Condensed matter models with Weyl and Dirac fermions

Armed with the tools necessary to quantify non-trivial topology of 2D and 3D systems we now present models which revolutionized the understand of topological behavior of electronic states in condensed matter physics. Historically this began with the surprising discovery of massless charge carriers in graphene, whose 2D Dirac cones hinted at a deeper connection between band structure and geometry. This insight spurred a theoretical leap with the Kane-Mele model, which demonstrated the vital role of spin-orbit coupling could open a topological gap and give rise to a new phase of matter: the quantum spin Hall insulator, a theoretical precursor to the modern topological insulator.

The subsequent development of the Bernevig-Hughes-Zhang (BHZ) model translated this abstract theory into a realistic and experimentally verifiable prediction in HgTe/CdTe quantum wells, solidifying the existence of 2D topological insulators. The field then expanded encapsulating 3D material with the 3D BHZ model, which predicted and led to the discovery of materials with robust, protected surface states. This progression ultimately led to the exploration of systems where the band gap closes at isolated points or lines in momentum space, giving rise to topological semimetals such as Dirac and Weyl semimetals. The following discussion will trace this remarkable path, exploring how these foundational models have illuminated the profound role of topology in defining the properties of matter.

4.2.1 Graphene

Graphene is a 2D material composed of carbon atoms arranged in a honeycomb lattice. The lattice geometry is defined by two primitive vectors [c.f. Fig. 4.1(a)]

$$\boldsymbol{a}_1 = -\frac{a}{2}(3, \sqrt{3}), \qquad \text{and} \quad \boldsymbol{a}_2 = \frac{a}{2}(3, -\sqrt{3})\,. \tag{4.27}$$

Here a is the lattice constant. The honeycomb structure gives rise to unique electronic properties, as it is not a Bravais lattice but can be treated as such by including the two sublattices explicitly in the Hamiltonian. The nearest neighbor vectors are given by

$$\boldsymbol{\delta}_1 = \frac{a}{2}(1, \sqrt{3})\,, \quad \boldsymbol{\delta}_2 = \frac{a}{2}(1, -\sqrt{3})\,, \qquad \text{and} \quad \boldsymbol{\delta}_3 = (1, 0) \tag{4.28}$$

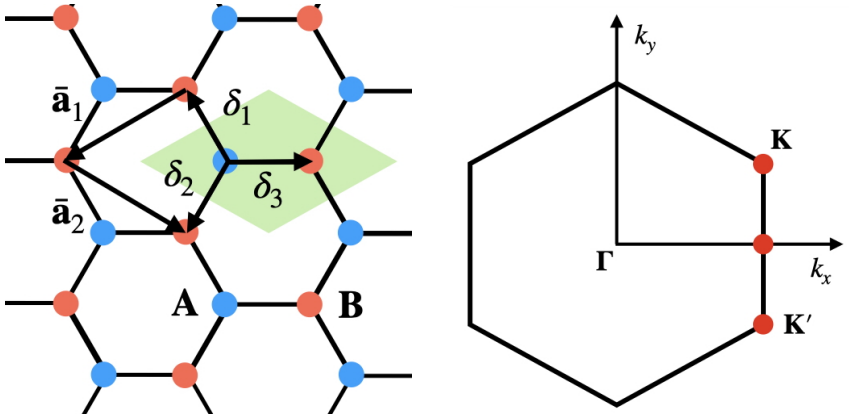

(a) (b)

Figure 4.1: (a) Real space lattice configuration of Carbon atoms at site A and B forming honeycomb structure. (b) Depicts the Brillouin zone in the momentum space along with energy degenerate points.

The electronic properties of graphene are well described by a nearest-neighbor tight-binding model. The Hamiltonian is given by

$$H = -t \sum_{\langle i,j \rangle} \left(a_i^\dagger b_j + \text{h.c.} \right) \tag{4.29}$$

where t is the hopping parameter between nearest neighbors, $a_i^\dagger$ and $b_i^\dagger$ are creation operators for electrons on sublattices A and B, respectively. The summation runs over all nearest-neighbor pairs. To analyze the system in momentum space, we apply a Fourier transform. The resulting Hamiltonian in momentum space is given as

$$H(\boldsymbol{k}) \;=\; -t \begin{pmatrix} 0 & f(\boldsymbol{k}) \\ f^*(\boldsymbol{k}) & 0 \end{pmatrix}, \quad \text{here} \;\; f(\boldsymbol{k}) = e^{-\imath \boldsymbol{k}\cdot\boldsymbol{\delta}_1} + e^{-\imath \boldsymbol{k}\cdot\boldsymbol{\delta}_2} + e^{-\imath \boldsymbol{k}\cdot\boldsymbol{\delta}_3}. \tag{4.30}$$

Employing the Pauli matrices the Hamiltonian can be represented as

$$H(\boldsymbol{k}) \;=\; -t \left(\sum_i^3 \cos \boldsymbol{k}\cdot\boldsymbol{\delta}_i \right) \sigma_x - t \left(\sum_i^3 \sin \boldsymbol{k}\cdot\boldsymbol{\delta}_i \right) \sigma_y \,. \tag{4.31}$$

This formulation enables us to investigate the electronic structure and its topological features. The energy eigenvalues are given by

$$E(\boldsymbol{k}) \;=\; \pm\sqrt{h_1^2 + h_2^2} \quad \text{where,} \tag{4.32}$$

$$h_1 = -t \left[\sum_i^3 \cos \boldsymbol{k}\cdot\boldsymbol{\delta}_i \right], \qquad \text{and} \qquad h_2 = -t \left[\sum_i^3 \sin \boldsymbol{k}\cdot\boldsymbol{\delta}_i \right] \tag{4.33}$$

It can be easily verfied that the zeros of the energy are at the corner of the Brillouin zone at $\boldsymbol{K} = (2\pi/3a,\, 2\pi/3\sqrt{3}a)$ and $\boldsymbol{K'} = \boldsymbol{K} - (0,\, 4\pi/3\sqrt{3}a)$ as shown in Fig. 4.1(b). As these points are described by a Dirac equation they are called 'massless' Dirac points or Weyl points. To investigate further we can expand the Hamiltonian about of one these points upto linear order in momentum $\boldsymbol{k} = \boldsymbol{K} + \boldsymbol{q}$. This gives us an effective model for the gapless point

$$H_{\text{eff}}(\boldsymbol{q}) = v_F \begin{pmatrix} 0 & q_x - iq_y \\ q_x + iq_y & 0 \end{pmatrix}, \tag{4.34}$$

here $v_F = 3ta/2$ is the Fermi velocity. We can now calculate the energy eigenstates which will eventually let us to compute Berry curvature and Chern number. The eigenstates are given by

$$|\psi_+(\boldsymbol{q})\rangle = \frac{1}{\sqrt{2}} \begin{pmatrix} 1 \\ e^{i\theta(\boldsymbol{q})} \end{pmatrix}, \qquad |\psi_-(\boldsymbol{q})\rangle = \frac{1}{\sqrt{2}} \begin{pmatrix} e^{-i\theta(\boldsymbol{q})} \\ -1 \end{pmatrix}, \tag{4.35}$$

where

$$\theta(\boldsymbol{q}) \;=\; \arctan\left(\frac{q_y}{q_x}\right). \tag{4.36}$$

These states represent the conduction ($|\psi_+\rangle$) and valence ($|\psi_-\rangle$) bands. The Berry connection and Berry curvature are given as

$$\begin{aligned} \boldsymbol{A}_+(\boldsymbol{q}) &= \frac{1}{2}\partial_{\boldsymbol{q}}\theta(\boldsymbol{q}) = \pm\left(\frac{q_y}{q^2}, -\frac{q_x}{q^2}, 0\right) \\ \boldsymbol{\Omega}(\boldsymbol{q}) &= \pm\frac{1}{2}\delta(\boldsymbol{q}). \end{aligned} \tag{4.37}$$

here $\delta(\boldsymbol{q})$ is the 2D Dirac delta function which implies that the Berry curvature vanishes everywhere except $\boldsymbol{q} = 0$, the Dirac point. Note that Berry curvature is a vector valued quantity which points perpendicular to $q_x - q_y$ plane. Performing the simple integral for Chern number we get ± 1. The Hamiltonian describing the Weyl point is simply $\boldsymbol{q} \cdot \boldsymbol{\sigma}$, suggesting that the pseudo-spin $\boldsymbol{\sigma}$ can be either parallel or anti-parallel with $\boldsymbol{q}$. This is called the chirality of the Weyl point and for pristine graphene, chirality of Weyl nodes is tied with the momentum they appear on. The contributions to the Chern number from the Weyl points cancels out, leading to a total Chern number of 0 in the Brillouin zone. The tight binding Hamiltonian for graphene preserves the time reversal symmetry where $\mathcal{T}$ is complex conjugation operator. Recall from the previous section that the conjugation operator as the

time reversal operation implies that Hamiltonian describes a pseudo spin. This translates to the sublattice A and B behaving as a pseudo spin space for graphene.

Haldane in 1988 [131] presented a model based on honeycomb lattice which does not preserves the time reversal symmetry even without an external magnetic field applied. Haldane introduced the following

$$H_{haldane} = m\sum_{ij}(a_i^\dagger a_i - b_i^\dagger b_i) - t\sum_{\langle\langle ij\rangle\rangle} e^{\pm\imath\phi}(a_i^\dagger a_i + b_i^\dagger b_i) + \text{h.c.} \tag{4.38}$$

here m is an onsite potential which has opposite sign for sublattice A and B breaking the sublattice symmetry. The model has a next to nearest neighbor hoping with a complex phase of $e^{\pm\imath\phi}$ which takes positive or negative sign based on the direction of hopping. Incorporating the Haldane terms in graphene and using periodic boundary condition we get a additive term in the Hamiltonian as the coefficient to σ_z given by

$$h_3 = m + 2t\,\sin\phi\sum_{i=1}^{3}\sin\boldsymbol{k}_i\cdot\boldsymbol{a}_i \tag{4.39}$$

here, $\boldsymbol{a}_3 = -\boldsymbol{a}_2 - \boldsymbol{a}_1$. The Brillouin zone remains the same and the energy dispersion is gapless when $h_1 = h_2 = h_3 = 0$ simultaneously. This requires that if there are gapless states (degenerate energy states) they will still be located at $\boldsymbol{K}$ and $\boldsymbol{K'}$. If $m > 2t\,\sin\phi$ there can be no gap in the system as there are no real momenta which would satisfy $h_3 = 0$. As the gap closes at $\boldsymbol{K}$ and $\boldsymbol{K'}$ the condition for which the degenerate states can exist read as follow

$$\begin{aligned} h_3(\boldsymbol{k} = \boldsymbol{K}) &= 0 \\ m + 3\sqrt{3}\,t\,\sin\phi &= 0 \end{aligned} \tag{4.40}$$

the above is an essential condition for the gap closing at $\boldsymbol{K}$ which does not imply gap closing at $\boldsymbol{K'}$ which requires $m - 3\sqrt{3}\,t\,\sin\phi = 0$. The gap-closing happens for different values of m at $\boldsymbol{K}$ and $\boldsymbol{K'}$ except when $\phi = 0, \pi$. To further understand the situation consider the Hamiltonian near the gap-closing point $\boldsymbol{K}$. We invoke the spherical polar representation we introduced in the previous section, the pseudo spin vector for the Hamiltonian points in the north (south) for $h_3 > 0$ ($h_3 < 0$).

When the staggered on-site potential (m) is large and positive it breaks inversion symmetry and opens a band gap at the Dirac points. The complex hopping term's influence is minimal, and while it creates local Berry curvature. The orientation on the Bloch sphere is largely fixed and even though the pseudo spin vector feels "pseudo-magnetic field" that points

north, and all it does is small wobbles as the momentum vector $\boldsymbol{k}$ changes. The band gap is wide, and thus total rotation over the entire BZ is zero. Consequently, the Chern number is zero, and the system is a trivial insulator with no protection. This phase is non-topological because its properties can be adiabatically connected to those of a simple insulator.

The magic happens at the phase transition, when the on-site potential m becomes precisely equal to one of the critical values as we discussed. At these specific points, the band structure inverts, and the Berry curvature becomes singular. The Chern number is not well-defined at these exact point because a topological invariant can only change when the bulk band gap closes. This band inversion is the mechanism for the change in the Chern number. After passing through the phase transition, the on-site potential m becomes negative, and the system enters the topological regime. This term breaks time-reversal symmetry and generates a net Berry flux over the entire Brillouin zone. The integral of this flux yields a non-zero, quantized integer value for the Chern number, which is typically ± 1. This non-zero Chern number indicates that the bulk material is in a topologically non-trivial state.

Kane and Mele [5] presented a model based on honeycomb lattice which generalizes the Haldane model by not only incorporates next nearest neighbor spin-orbit interaction (λ_{SO}) alongwith Rashba spin-orbit coupling (λ_R) and alternating on-site potential (λ_v) given as follows

$$\begin{aligned} H &= t\sum_{\langle ij\rangle} a_i^\dagger b_j + \imath\lambda_{SO}\sum_{\langle\langle ij\rangle\rangle} \nu_{ij}(a_i^\dagger a_j + b_i^\dagger b_j)s_z \\ &\quad +\imath\lambda_R\sum_{\langle ij\rangle} a_i^\dagger(\boldsymbol{s}\times\hat{\boldsymbol{d}}_{ij})_z b_j + \lambda_v\sum_i (a_i^\dagger a_i - b_i^\dagger b_i) \end{aligned} \tag{4.41}$$

here $\hat{\boldsymbol{d}}_{ij}$ represents the radial vector connecting the sits i and j, and $\boldsymbol{s}$ represents the spin. ν_{ij} takes a value of ± 1 based on the clockwise or anticlockwise path it takes to reach the next nearest neighbor. The term with λ_{SO} is known as the Kane-Mele (KM) term, and it takes its inspiration from the model presented by Haldane [131]. Haldane's model breaks the time reversal symmetry by adding the mass term which here is given by λ_v and spin-independent exchange of next nearest neighbor hopping term with a complex phase $e^{\pm\imath\phi}$. Kane and Mele model preserves the time reversal symmetry by simultaneously handling the copies of Haldane model at $\boldsymbol{K}$ and $\boldsymbol{K'}$ within the KM term by a spin exchange. In other words the model is constructed such that it has the time reversal partners at $\boldsymbol{K}$ and $\boldsymbol{K'}$ and the time reversal operator when acts on the Hamiltonian it ends up connecting the valley points. This non trivial way of opening the gap comes at a cost namely, the Hamiltonian is now in Kronecker product basis of sublattice σ, valley τ, and spin s space.

The KM model is a highly idealized representation. Its intrinsic SOC term is a next-nearest-neighbor hopping, which is a weak effect in real graphene. This requires an unphysically large SOC strength to open a bulk gap and realize the topological phase.

4.2.2 BHZ model

Bernevig-Hughes-Zhang (BHZ) model is an effective low-energy Hamiltonian designed to capture the electronic properties of Mercury Telluride (HgTe) quantum wells sandwiched by Cadmium Telluride (CdTe) barriers. The BHZ model did not suggest a material class but provided a quantitative prescription for engineering a topological state. HgTe and CdTe both have a intertwined face centered cubic structure of cations and anions. The bulk band structure around the Γ point is shown in Fig. 4.2(a). The energy band gap in HgTe is smaller

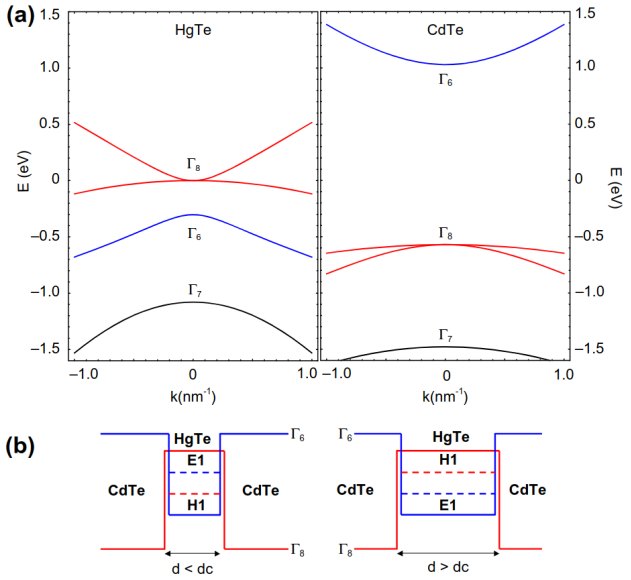

Figure 4.2: (a) Bands for HgTe and CdTe respectively near Γ point. (b) Schematic of HgTe/CdTe quantum well depicting the subbands $H1$ -$E1$ begin inverted to $E1$-$H1$ depending on the thickness (d) of the quantum well relative to critical thickness (d_c).

than CdTe although with inverted bands. In the original work [6] neglected the effect of Γ_7 band due to its negligible effects. Moreover, they argued that its the $|\Gamma_6, \pm\frac{1}{2}\rangle$, $|\Gamma_8, \pm\frac{1}{2}\rangle$, and $|\Gamma_8, \pm\frac{3}{2}\rangle$ which combine to give rise to the 3 subbands of the Quantum well namely, $H1$, $E1$, and $L1$. They proposed that the ordering of the subbands 'inverts' based on the thickness of the quantum well. Additionally, they claimed that there exists a critical thickness d_c of quantum well which separates the two distinct phases of the system. Furthermore, the phenomenon of band inversion and the underlying physics is relatively unaffected by $L1$, leaving us with a four-band model. Employing various symmetry conditions on the states,

four-band BHZ model is given by

$$H = \begin{pmatrix} h(k) & 0 \\ 0 & h^*(-k) \end{pmatrix}; \quad h(k) = \boldsymbol{\epsilon}(k) + \boldsymbol{d}\cdot\boldsymbol{\sigma} \tag{4.42}$$

here, $\boldsymbol{\sigma}$ is the Pauli matrix vector, $\boldsymbol{\epsilon}(k) = C - 2D\,(2 - \cos k_x - \cos k_y)$ and $\boldsymbol{d} = [A\sin k_x,\, A\sin k_y,\, -2B(2 - M/2B - \cos k_x - \cos k_y)]$. The parameters A, B, C, D and M control the geometry of the quantum well. For the ease of representation we define

$$\tau_y = \begin{pmatrix} 0 & -\imath\mathbb{I} \\ \imath\mathbb{I} & 0 \end{pmatrix}, \qquad \tau_z = \begin{pmatrix} \mathbb{I} & 0 \\ 0 & -\mathbb{I} \end{pmatrix} \tag{4.43}$$

$\mathbb{I}$ is a 2 x 2 block matrix. The time reversal symmetry operation can be represented as $\mathcal{T} = \imath\tau_y\, K$ and the Hamiltonian preserves the time reversal symmetry. We have an additional charge conjugation symmetry $\mathcal{C}^\dagger H(k)\,\mathcal{C} = -H(k)$, given $\mathcal{C} = \imath\sigma_y\, K$. The energy eigenvalues for H are $\epsilon(k) \pm |d|$. It is clear that the energy eigenvalues are degenerate and this can be attributed to the fact that time reversal operator obeys $\mathcal{T}^\dagger\mathcal{T} = -1$. This results in model to have Kramer's degeneracy thus

$$\begin{aligned} \mathcal{T}H(k)|\psi_k\rangle &= E(k)\mathcal{T}|\psi_k\rangle \\ H(-k)\mathcal{T}|\psi_k\rangle &= -E(k)\mathcal{T}|\psi_k\rangle \\ H(-k)|\mathcal{T}\psi_k\rangle &= E(k)|\mathcal{T}\psi_k\rangle \end{aligned} \tag{4.44}$$

hence every $|\psi_k\rangle$ has a degenerate Kramer partner $|\mathcal{T}\psi_k\rangle$. Expanding the Hamiltonian about the Γ point we get, $\boldsymbol{d} = (A\,k_x,\, A\,k_y,\, \mathcal{M}(k))$, and $\boldsymbol{\epsilon} = C - D(k_x^2 + k_y^2)$ where $\mathcal{M}(k) = M - B(k_x^2 + k_y^2)$. As pointed out earlier, H has degenerate spectrum and thus the eigenvalues of $h(k)$ along with their Kramer partner form the entire spectrum. The energy eigenvalues for $h(k)$ are $E_\pm = \epsilon \pm \sqrt{Ak^2 + \mathcal{M}^2}$, now if $B = 0$ the spectrum follows the dispersion of a Dirac fermion with mass M making it appropriate to refer $\mathcal{M}$ as the mass term. Recall in the previous section we represented the two level system in polar basis, whereby the vector $\boldsymbol{d}$ rotated as k changed leading to different topological phases. Analogous to two-level system the vector $\boldsymbol{d}$ at $k_x = k_y = 0$ makes angle $\arccos\frac{d_z}{|d|}$ with the north pole which is related to the sgn(M). For $M/B > 0$, vector $\boldsymbol{d}$ points in the north(south) pole for positive(negative) M and as $k \to$ inf it rotates and points in the south(north) pole imparting the system with a non trivial topology. Due to time reversal partner pair the total chern number is still zero. Nevertheless, the topological signature can be observed in the system with finite size or an

edge as we will see in later section. Additionally, for $M/B < 0$ the system not only has a gap but the wavefunction never acquires the additional phase for topological phase transition making it a trivial insulator. Mass term also directly gives the gap in the spectrum, the change of sign of M points to thickness of quantum well which is then used to compute the critical thickness d_c.

4.2.3 Model for 3D topological insulator

In the 2D BHZ model, as discussed in the context of HgTe quantum wells, the topological insulating phase indeed arises from a composite structure- a heterostructure of HgTe and CdTe. The key is the quantum confinement in the well, which tunes the energy levels of the HgTe layers relative to the CdTe barriers, leading to the necessary band inversion. The road towards a model for 3D topological insulator was realized with the observation of massive Dirac fermion in $Bi_{0.9}Sb_{0.1}$ [132] being part of a broader family of $Bi_{1-x}Sb_x$. It was predicted by Fu. et al. [133] using the parity of the eigenvalues of the states at the time reversal invariant points in the Brillouin zone that $Bi_{1-x}Sb_x$ is a topological insulator, and this was further strengthened by prediction made using phenomenological arguments in [134]. The understanding of 3D TIs often begins with a low-energy effective Hamiltonian that captures the essential physics near the Fermi level and the topological phase transition. For many prominent 3D TIs, such as the bismuth chalcogenides (e.g., Bi_2Se_3, Bi_2Te_3, Sb_2Te_3), the crystal structure is rhombohedral with five atoms in a unit cell (quintuple layers). The crucial aspect for their topological nature is the "band inversion" phenomenon, where the typical ordering of conduction and valence bands at certain high-symmetry points in the Brillouin zone (similar to the heterostructure of HgTe) is inverted due to strong spin-orbit coupling (SOC).

A widely adopted effective model for the bulk states near the Γ point (Brillouin zone center) for these materials is a 4×4 Dirac-like Hamiltonian. This Hamiltonian is typically constructed by considering the relevant atomic orbitals contributing to the band inversion, usually p-orbitals from the constituent elements (e.g., Bi p-orbitals and Se p-orbitals in Bi_2Se_3). The Hamiltonian can be expressed in a basis of parity eigenstates, reflecting the inversion symmetry often present in these materials. A general form of such a Hamiltonian,

assuming time-reversal symmetry and inversion symmetry, can be written as

$$H(k) = \epsilon_0(\boldsymbol{k})I + \begin{pmatrix} M(\boldsymbol{k}) & A_1k_z & 0 & A_2k_- \\ A_1k_z & -M(\boldsymbol{k}) & A_2k_+ & 0 \\ 0 & A_2k_- & M(\boldsymbol{k}) & -A_1k_z \\ A_2k_+ & 0 & -A_1k_z & -M(\boldsymbol{k}) \end{pmatrix} \tag{4.45}$$

where $\boldsymbol{k} = (k_x, k_y, k_z)$, along with $k_\pm = k_x \pm \imath k_y$ and I representing a 4×4 identity matrix. The Hamiltonian has a shift of energy $\epsilon_0 = C + D_1k_z^2 + D_2(k_x^2 + k_y^2)$ overall being parabolic in nature. $M(\boldsymbol{k}) = M_0 - B_1k_z^2 - B_2(k_x^2 + k_y^2)$ represents the mass term. The change of sign of M_0 at the Γ point represents the band inversion. The parameters involved are material specific and represent different coupling strength and fitted to the experimental data or ab initio calculations.

Thallium-based Chalcogenides: Thallium based compounds like $TlBiSe_2$, $TlBiTe_2$, $TlSbSe_2$ share a rhombohedral crystal structure similar to Bi_2Se_3 but incorporate Tl. They are predicted [135] and confirmed [136] to be strong TIs with significant energy gaps.

Rare-earth based Chalcogenides: This class includes stoichiometric compounds like $LnBiTe_3$ and $LnSbTe_3$, where Ln is a rare earth element like La or Y that doesn't have f-electrons. They are derived from the Bi_2Se_3 type by substituting one cation atom with a rare earth element. $LaBiTe_3$ is predicted [137] to be a TI.

$PbBi_2Se_4$ type: These are layered chalcogenides formed by inserting double layers for instance -Pb-Se- into the quintuple layers of Bi_2Se_3. Examples include $Pb_nBi_2Se_{3+n}$ and $Pb_nSb_2Te_{3+n}$ for certain values of 'n' and have been predicted to be candidates for 3D TI [138].

Strained Bulk HgTe, HgSe, and $\alpha-HgS$: While HgTe is famous for 2D TIs in quantum wells, its bulk form, along with HgSe and $\alpha-$HgS, can become 3D TIs when cubic symmetry is broken, for example, by applying uniaxial strain. This opens up an energy gap, revealing their topological nature [139].

Heusler Compounds: This diverse class of ternary materials where XYZ or X_2YZ stoichiometry shares structural and electronic similarities with zincblende semiconductors like HgTe. Many Heusler compounds like LuPtBi, YPtBi have been predicted and shown to exhibit band inversion similar to HgTe, making them 3D TIs [140–142].

Chalcopyrite Semiconductors: Ternary ABC_2 chalcopyrite compounds are isoelectronic analogs to binary semiconductors. Their crystal structure, a doubled zincblende, allows for a natural breaking of cubic symmetry, leading to a finite energy gap and topological properties similar to HgTe [143].

$\alpha-$ and $\beta-$ Ag_2Te: $\alpha-Ag_2Te$ is identified as a HgTe-type TI. Upon a structural phase transition to the $\beta-$phase at low temperatures, it becomes a true TI with an anisotropic surface Dirac cone [144].

Skutterudites and filled Skutterudites: Materials like $RhSb_3$ and $IrSb_3$ are predicted to be zero-gap TIs. In filled skutterudites the band inversion occurs between p and d orbitals, or even d and f orbitals, leading to topological properties often coexisting with other phenomena like Kondo effect or magnetism [145].

PbTe, SnTe, and Related Materials: SnTe is a *crystalline topological insulator* where surface states are protected by mirror symmetry. Uniaxial strain can also induce a strong TI phase in materials like PbSe [146].

Correlated Materials with d or f Orbitals: This is a frontier area, including Ir-based materials like $Ln_2Ir_2O_7$ [147] pyrochlore oxides and certain Kondo insulator like SmB_6 [148]. These materials exhibit topological phases where electron correlation effects, coupled with strong SOC, play a significant role.

4.2.4 Semimetals

The conceptual link between these TIs and semimetals is a natural, continuous one, where a topological insulator can be driven into a topological semimetal phase by tuning material parameters. The modern era of topological materials was heralded by the theoretical prediction and subsequent experimental discovery of 3D topological insulators. This relationship is deeply rooted in the theoretical foundations of both high energy particle physics and condensed matter band theory, offering a unified perspective on these seemingly disparate states of matter. To fully appreciate this transition, it is essential to consider two seemingly unrelated topics from the early days of quantum mechanics: relativistic wave equations for fermions and the conditions for degeneracies in energy spectra. Following the introduction of the Dirac equation, Hermann Weyl proposed a simplified version of this equation, which described massless fermions with a definite "chirality" or handedness. While these concepts found vast application in particle physics, the search for fundamental Weyl fermions proved elusive. In parallel, in condensed matter physics, the problem of "accidental degeneracies" in electronic band structures was being investigated. A fundamental result from quantum mechanics, known as the von Neumann-Wigner theorem, states that in a generic quantum system (described by a Hermitian Hamiltonian) without any protecting symmetries, two energy levels will typically not be degenerate. One must tune the parameters of the Hamiltonian to enforce degeneracy in the system. This can be understood by considering a 2×2

Hermitian Hamiltonian H, which can be written in the most general form as:

$$H = \sum_{i=0}^{3} \alpha_i(\boldsymbol{k})\boldsymbol{\sigma}_i \tag{4.46}$$

here, $\alpha_i(\boldsymbol{k})$'s are general function of momentum and $\boldsymbol{\sigma}_i$ are the Pauli matrices. The eigenvalues are given by $E = \alpha_0(\boldsymbol{k}) \pm \sqrt{\alpha_1(\boldsymbol{k})^2 + \alpha_2(\boldsymbol{k})^2 + \alpha_3(\boldsymbol{k})^2}$ and it is essential for the α_i (for $i \in \{1, 3\}$) to vanish at certain momentum $\boldsymbol{k}$ in order to ensure degeneracy. This is a crucial point, such band degeneracies are not accidental in a 1D or 2D parameter space and can occur at isolated points in a 3D momentum space naturally. The dispersion relation near such a degeneracy is generically linear, resembling the Weyl equation, even in the non-relativistic context of a solid-state material. The profound connection between these two ideas was later solidified by the realization that these band-touching points act as sources and sinks of Berry curvature in momentum space.

The quasiparticle excitations in Dirac and Weyl semimetals are viewed as low-energy effective descriptions of the electronic states in solid-state systems that behave like relativistic fermions. The existence of these gapless excitations is fundamentally protected by a combination of time reversal symmetry and crystal symmetry. In a Dirac semimetal, both time reversal symmetry ($\mathcal{T}$) and inversion symmetry ($\mathcal{I}$) are preserved. Time reversal symmetry ensures that for every energy band $E(\boldsymbol{k})$, there is a corresponding partner band at $E(-\boldsymbol{k})$. Similarly, inversion symmetry imposes the condition that $E(\boldsymbol{k}) = E(-\boldsymbol{k})$. The combined effect of these two symmetries creates a crucial constraint on the electronic structure. It dictates that for a given momentum $\boldsymbol{k}$, the eigenstates must be four-fold degenerate. The four-fold degeneracy that defines a Dirac point is a direct consequence of this combined symmetry protection. A Dirac point can be theoretically understood as two distinct, two-fold degenerate Weyl points of opposite chirality that are pinned to the same location in momentum space by both time reversal and inversion symmetry. The breaking of this delicate symmetry balance is what gives rise to the different types of topological semimetals. To demonstrate this more concretely, we can consider a low-energy effective 4×4 Hamiltonian that describes a Dirac semimetal near a degeneracy point. This Hamiltonian is typically derived from $\boldsymbol{k} \cdot \boldsymbol{p}$ perturbation theory, taking into account the symmetries of the crystal. The theoretical prediction of Na_3Bi uses a common representation with two sets of Pauli

matrices, one for spin (σ) and one for pseudo spin degrees of freedom (τ) [149, 150]:

$$H_{\text{Dirac}} = \epsilon_0(\boldsymbol{k})I + \begin{pmatrix} M(\boldsymbol{k}) & Ak_+ & 0 & B^*(\boldsymbol{k}) \\ Ak_- & -M(\boldsymbol{k}) & B^*(\boldsymbol{k}) & 0 \\ 0 & B(\boldsymbol{k}) & M(\boldsymbol{k}) & -Ak_- \\ B(\boldsymbol{k}) & 0 & -Ak_+ & -M(\boldsymbol{k}) \end{pmatrix} \tag{4.47}$$

here, $\epsilon_0(\boldsymbol{k}) = C_0 + C_1k_z^2 + C_2(k_x^2 + k_y^2)$, and mass term $M(\boldsymbol{k}) = M_0 - M_1k_z^2 - M_2(k_x^2 + k_y^2)$. The off-diagonal term are given by $Ak_\pm$ and $B(\boldsymbol{k}) = \alpha k_z k_+^2$, where $k_\pm = k_x \pm \imath k_y$. The parameter C_i, M_i (for $i \in \{1, 3\}$), and A are determined by the material geometry. The eigenvalue of the Hamiltonian is given by

$$E(\boldsymbol{k}) = \epsilon(\boldsymbol{k}) \pm \sqrt{A^2k_+k_- + M^2(\boldsymbol{k}) + |B(\boldsymbol{k})|^2} \tag{4.48}$$

The energy vanishes at $\boldsymbol{k}_0 = (0, 0, \pm m)$, where $m = \sqrt{M_0/M_1}$. These momentum are four fold degenerate and identified as the Dirac points. The inversion symmetry is given by $\mathcal{I} = \tau_z\,\sigma_0$, and the Hamiltonian obeys $\mathcal{I}H_{\text{Dirac}}(\boldsymbol{k})\mathcal{I}^{-1} = H_{\text{Dirac}}(-\boldsymbol{k})$ to posses inversion symmetry. Similarly, time reversal symmetry $\mathcal{T} = \imath\tau_0\,\sigma_y K$, where K is the complex conjugation operator. Time reversal symmetry demands the Hamiltonian to follow $\mathcal{T}H_{\text{Dirac}}(\boldsymbol{k})\mathcal{T}^{-1} = H_{\text{Dirac}}(-\boldsymbol{k})$. The presence of both time reversal and inversion symmetries is what enforces the merging of two Weyl points with opposite chirality at the same momentum, thereby creating and protecting a four-fold degenerate Dirac point. This occurs precisely where the momentum dependent coefficients in the Hamiltonian vanish simultaneously.

The rich diversity of topological semimetals arises when one of these protective symmetries is broken. Consider the simplest of the case with $\alpha = 0$, in the vicinity of the Dirac points the Hamiltonian after keeping the leading order terms takes the following form

$$H_{\text{Dirac}} = m\tau_z\,\sigma_0 + v_xk_x\tau_x\,\sigma_z - v_yk_y\tau_y\,\sigma_0 + v_zk_z\tau_z\,\sigma_z \tag{4.49}$$

$$= \begin{pmatrix} m\tau_z + v_zk_z\tau_z + v_xk_x\tau_x - v_yk_y\tau_y & 0 \\ 0 & m\tau_z - v_zk_z\tau_z - v_xk_x\tau_x + v_yk_y\tau_y \end{pmatrix} \tag{4.50}$$

The structure makes the existence of Weyl points obvious. The material when tuned with $\alpha = 0$ leads to decoupling of Weyl points and creates two Weyl points at $\boldsymbol{k}_0$ with opposite chirality. In case of materials like Bi_2Se_3 or Bi_2Te_3, $B(\boldsymbol{k})$ takes a linear form again coupling the Weyl points and making the system gapped hence with massive Dirac points.

Turning a topological insulator or a Dirac semimetal into a Weyl semimetal allows for the

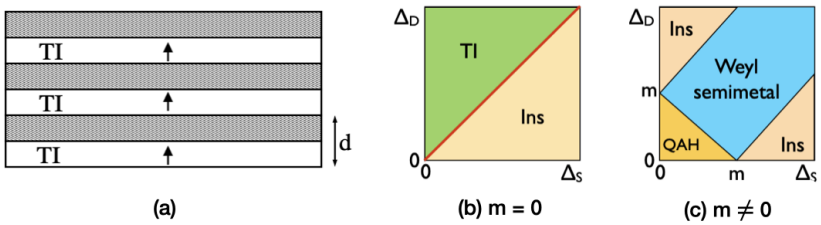

Figure 4.3: (a) Schematic of a multi-layered structure composed of alternating layers of topological insulator (shaded) and normal insulator (unshaded). The topological phase of the multi-layered structure for the parameter regime which leads to (b) gapless states within BZ signified by $m = 0$, and without these (c) gapless states when $m \neq 0$. Δ_D is the tunneling amplitude for adjacent layers of neighboring topological insulator layer. Δ_S is the tunneling amplitude within the bottom and top layer of the same topological insulator. Adopted from Ref. [151]

controlled creation of exotic topological phases. This transition is fundamentally governed by the manipulation of symmetries that protect the initial topological state. The most direct and well-studied pathways involve breaking either time reversal symmetry or inversion symmetry.

A straightforward approach involves breaking time reversal symmetry, typically by applying an external magnetic field. The field acts as a perturbation, lifting the degeneracy and splitting the single Dirac point into a pair of distinct Weyl points. The separation of these Weyl points in momentum space is directly proportional to the strength of the magnetic field. A foundational work proposing this mechanism is Burkov *et. al* [151] presented a theoretical model for creating a WSM in a heterostructure composed of a 3D topological insulator and a ferromagnetic insulator as shown in Fig. 4.3(a). This setup uses the magnetic proximity effect to introduce an effective Zeeman field, which breaks time reversal symmetry. This perturbation closes the bulk gap of the TI at two distinct points in momentum space and then reopens it, resulting in the creation of a pair of Weyl nodes with opposite chiralities. This phase transition can be understood through a phase diagram where the spin splitting exchange strength m and the intrinsic bulk parameters of the TI namely, tunneling amplitude within the top and bottom surface of same TI layer Δ_S and amplitude between top and bottom surface of neighbouring TI layers Δ_D. The system in the absence of m is in a topological insulator phase when the mass term (which defines the bulk gap Δ_D) is dominant as shown in Fig. 4.3(b). As the m increases, it competes with these intrinsic mass. The transition to the WSM phase occurs at a critical point where the magnetic perturbation becomes strong enough to close the bulk gap at two momentum points, leading to the creation of Weyl nodes. Further increase in the m moves the Weyl nodes further apart in momentum space. Alternatively, the DSM can be doped with magnetic impurities to split the Dirac points into

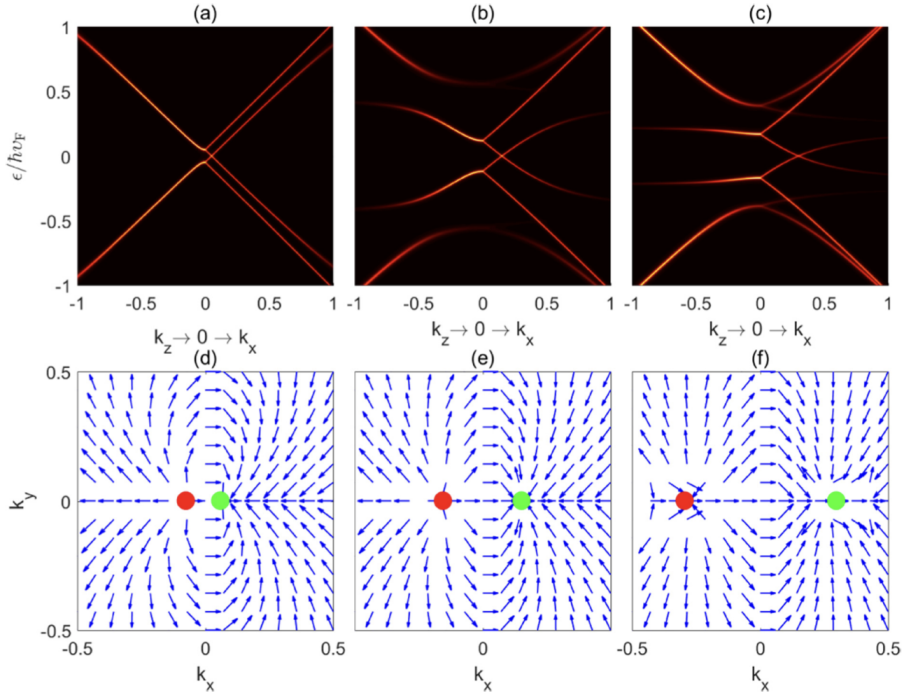

Figure 4.4: A Dirac semimetal doped magnetic impurities, the electric potential of the impurity is $U_0 = 0$ for the entire panel. The spin-dependent magnetic potential U_M is 0.5, 1.5, and 3 for first, second, and third column respectively. First row (a)-(c) is the dispersion of the Dirac semimetal along $k_z - 0 - k_x$, and the second row (d)-(f) is the corresponding map of the Berry curvature of the corresponding dispersion. The magnetic impurity splits and the Dirac node into two Weyl nodes and drives them apart as shown in red (positive chirality) and green (negative chirality) circles. Adopted from Ref. [152]

Weyl points. Evidence for this mechanism has been observed in materials like Cd_3As_2, where signatures of a magnetic field induced WSM phase were reported in [153] when doped with Mn. This local magnetic impurity breaks the time reversal symmetry to induce WSM phase.

Lee *et. al* [154] have demonstrated using non magnetic Au ion implantation into $Bi_{0.96}Sb_{0.04}$ which breaks the inversion symmetry to induce WSM phase from a DSM. The other primary method to break inversion symmetry can be achieved by applying strain or pressure to the material's lattice, which alters the crystal structure and lifts the protection of the Dirac point. In materials with a natural lack of inversion symmetry, the Dirac nodes are already split into Weyl nodes. Weng *et. al* [155] explicitly discussed how the absence of an inversion center in noncentrosymmetric transition metal monophosphides (TaAs, TaP, NbAs, and NbP) would split the Dirac nodes, providing a general theoretical framework for this transition. This was soon confirmed experimentally [24] by directly observing the Weyl points in TaAs.

The discovery of WSM marked a new era in condensed matter physics, introducing a class of materials whose low energy electronic excitations behave as massless, chiral fermions.

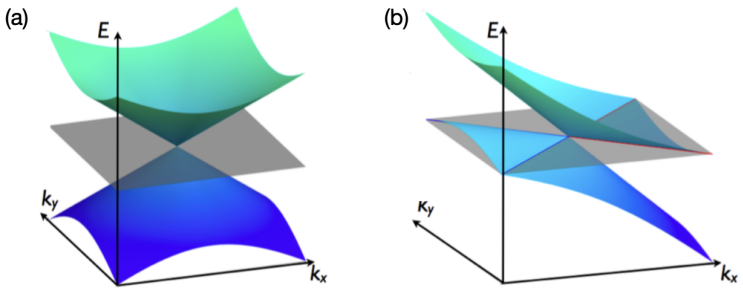

Figure 4.5: The dispersion of a Weyl node for $k_z = 0$. The grey shaded plane marks the Fermi level with $E = 0$ and cuts the Weyl node for both (a) and (b). (a) Is the type Weyl node with a point-like Fermi surface. (b) Type II Weyl node with an unbounded Fermi surface due to the tilt of the Weyl cone. Adopted from Ref. [156]

Theoretical and experimental studies have revealed a rich diversity in these materials, leading to a new classification based on the geometry of their electronic band structure: Type I and Type II WSMs. Type I WSM are the "standard" or more conventional type. In these materials, the Weyl cone is upright or only slightly tilted as shown in Fig. 4.5(a). The defining characteristic is that the Fermi energy crosses the Weyl node at a single point in momentum space. This results in a pointlike Fermi surface at the Weyl node itself. Energy dispersion near the Weyl node are well defined, and the low energy physics is accurately described by the linear dispersion of a relativistic Weyl fermion. The canonical examples of Type I WSM are the non-centrosymmetric transition-metal monopnictides, such as TaAs.

Type II WSM represents a more exotic phase. In these materials, the Weyl cone is significantly tilted, so much so that it can be "over-tilted" as shown in Fig. 4.5(b). As a result, the Fermi energy does not cross the Weyl node at a single point but rather intersects the cone over an extended region. This leads to a unique situation where the Weyl node emerges at the boundary between electron and hole pockets, creating a saddle point in the energy dispersion. This has profound consequences and the Fermi surface is no longer a point but consists of small, connected electron and hole pockets. The quasiparticles are no longer purely relativistic, and the low energy physics is a mixture of states. This tilting can lead to distinct transport properties, for instance, a breakdown of the chiral anomaly under certain conditions. WTe_2 is one of many theoretically predicted and experimentally verified Type II WSM [157].

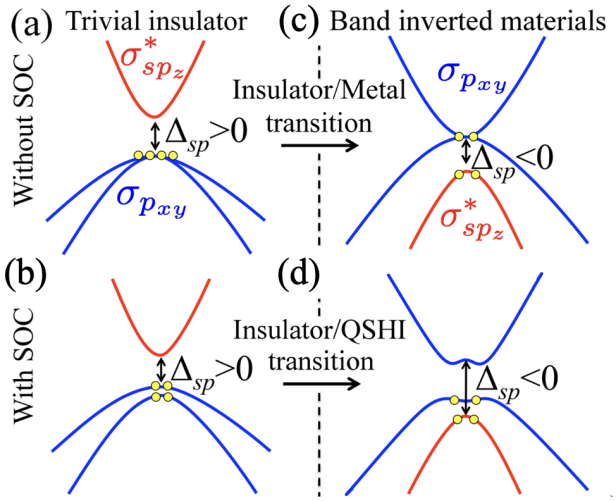

Figure 4.6: Band structure representation of the functionalized honeycomb lattice material. The bands near the Fermi level for the material (a), (c) without and (b), (d) with spin-orbit coupling. In presence of spin-orbit coupling the insulator transition leads to quantum spin hall insulator (QSHI) along with inverted band. Δ_{sp} denotes the band gap after hybridization and directly corelates to the robustness of the topological nature of the material. Adopted from Ref. [158]

4.3 Surface of Topological materials

The central organizing principle of topological materials is the bulk-boundary correspondence. This profound theoretical concept asserts that a material with a topologically non trivial bulk electronic structure, characterized by a non trivial topological invariant, must necessarily host protected, gapless electronic states at its interfaces with a topologically trivial medium, such as a vacuum. These boundary states arise from the change in the topological invariant across the interface. The specific nature of these states, i.e. whether they are helical edge channels, surface Dirac cones, or Fermi arcs is a direct manifestation of the bulk's topology and is robust against local perturbations and disorder due to its topological origin [159].

The initial breakthrough in topological insulators was in 2D, which gave rise to the QSH effect. In this state, a material that is a bulk insulator supports a pair of conducting edge channels where electrons with opposite spins travel in opposite directions. This spin-momentum locking, or helicity, is guaranteed by time reversal symmetry and strong spin-orbit coupling. 2D topological insulators exhibit edge states that traverse the bulk gap. These modes, protected by the Chern number and remain robust against perturbations preserving the underlying symmetry. The quantum spin Hall effect being the hallmark of such systems, where counter-propagating edge modes with opposite spins are protected by time-reversal symmetry. Experimental realizations in HgTe quantum wells [18, 161] and other materials

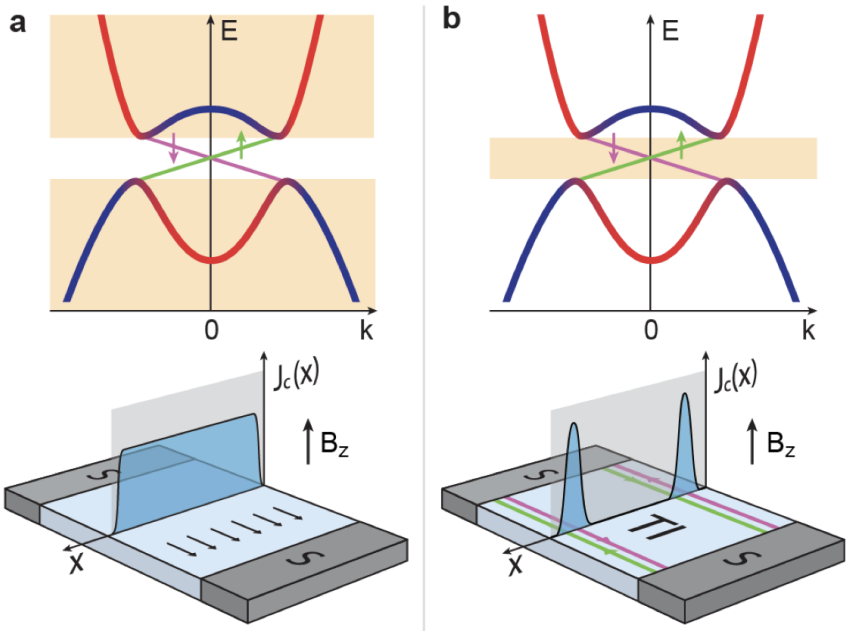

Figure 4.7: Band structure for the InAs/GaSb quantum well with electron (red) and hole (blue) contribution with a 2D bulk band crossing. (a) Shows the absence of edge states in case of the Fermi level adjusted in the bulk and (b) the localized current density on the edge when Fermi level is situated within topological gap. Adopted from Ref. [160].

have confirmed these theoretical predictions.

The theoretical underpinnings for the emergence of these helical edge states lie in the phenomenon of band inversion driven by SOC. In many 2D systems, the band structure is composed of conduction and valence bands originating from different atomic orbitals (e.g., s-like and p-like orbitals) as shown in Fig. 4.6. In a trivial insulator, the conduction band lies above the valence band, separated by an energy gap. However, when SOC is strong, it can significantly alter the band ordering. The SOC interaction preferentially lowers the energy of the s-like orbital-derived bands and raises the energy of the p-like orbital-derived bands. In certain materials like HgTe, this effect is so pronounced that at the Γ point of the Brillouin zone, the p-like bands are pushed to a higher energy, causing them to cross and invert their position with the s-like bands. This "band inversion" is the crucial event that changes the topological invariant of the bulk. According to the bulk-boundary correspondence, this change necessitates the presence of gapless edge states. Since time reversal symmetry is preserved, the electrons are still Kramers degenerate, meaning a state and its time reversed partner have the same energy. The edge states exist within the bulk gap and are spin-polarized, with opposite spins moving in opposite directions along the edge. This strong spin-momentum locking prevents backscattering from non-magnetic impurities, as a spin-up electron moving to the right cannot scatter into a spin-up state moving to the left, which is

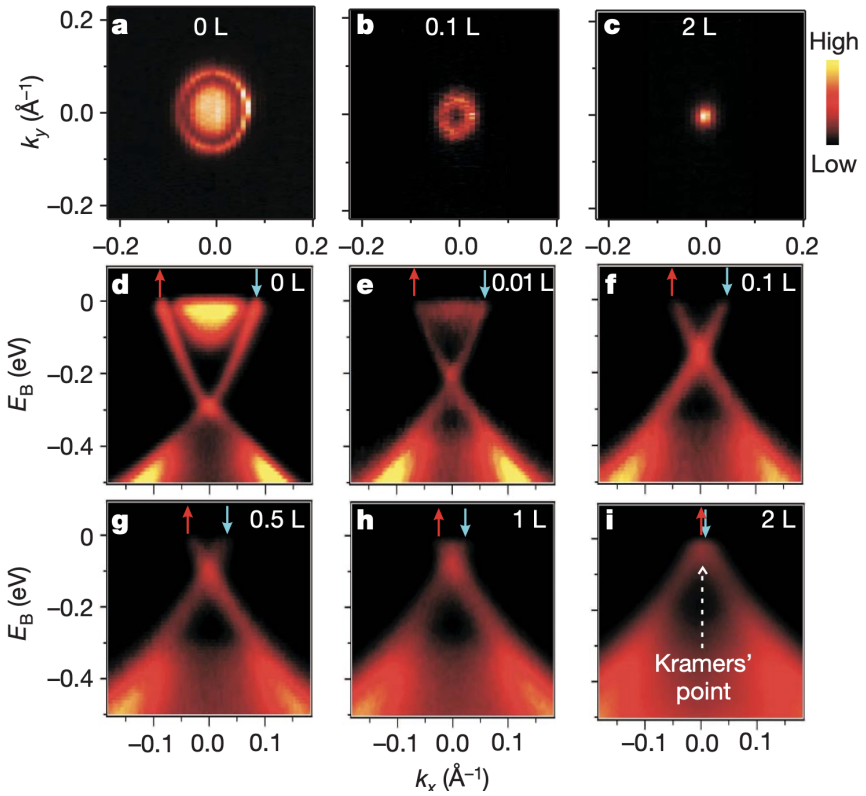

Figure 4.8: An ARPES map of the topological Fermi surface of $Bi_{2-\delta}Ca_\delta Se_3$, the results demonstrate the effects of the surface adsorption of NO_2. (a) Show the ring originating from the bulk-boundary resonance. The increase in dosage of NO_2 (b)-(c) show the elimination of the resonance and (c) and (i) show that a high dosage of 2L leads to Fermi level crossing the Dirac point. The arrows denote the spin polarization of the bands. Adopted from Ref. [21].

not an available state. The topological protection ensures this quantization is robust, leading to the observed quantized conductance.

The observation of these exotic edge states is critically dependent on the position of the Fermi level. For the topological phase to be observable, the Fermi level must be located within the bulk energy gap as shown in Fig. 4.7(b). In this scenario, the bulk of the material remains insulating, while the helical edge states provide the only available transport channels. This leads to the quantized conductance observed in experiments. If, however, the Fermi level is tuned to lie inside either the bulk conduction or valence band [c.f. Fig. 4.7(a)], the system behaves as a conventional metal. The bulk states, being far more numerous, dominate transport, effectively "shorting out" the topological edge states and making their unique properties impossible to distinguish through transport measurements. The type of edge state itself does not change, but its physical manifestation in experiments is entirely dependent on the Fermi level's position.

3D topological materials led to the discovery of new phases, all characterized by unique surface states that were directly linked to their bulk topology. The most effective technique

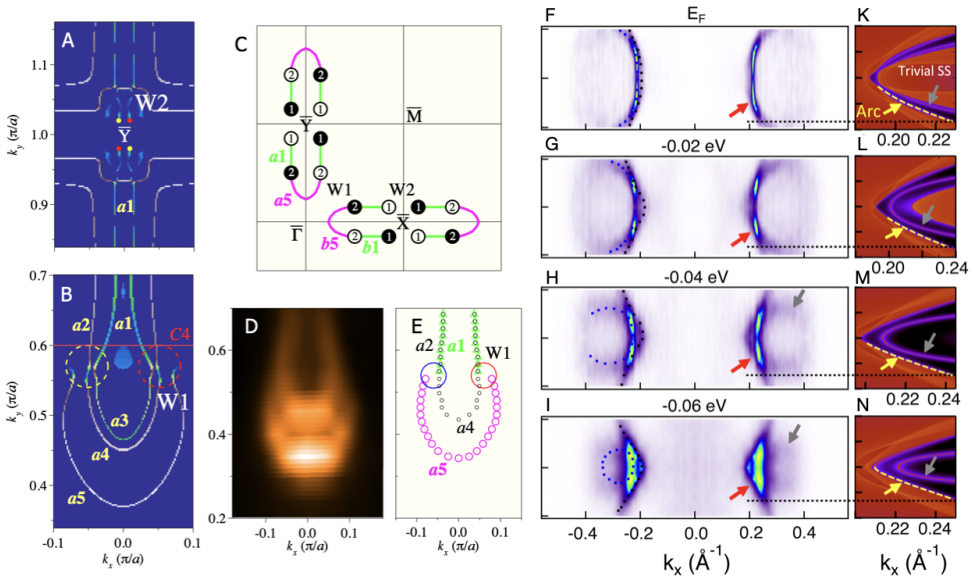

Figure 4.9: (A)-(E) Adopted from Ref. [24], are the surface Fermi arcs for TaAs. (A)-(B) Results from first principle calculations show the Weyl nodes highlighted with red and yellow circles, and (B) with dashed circles due to small offset of chemical potential. (C) Schematics of the part of momentum space, showcasing the locations of Weyl nodes with opposite chiralities (dark and hollow) connected with Fermi arcs. (D) The photoemission plot of $W1$ around the Fermi energy from with the respective Fermi arc shown in (E). (F)-(N) Surface Fermi arc plots for $MoTe_2$. (F)-(I) ARPES intensity map at $E_F = 0.005$ eV to -0.06 eV respectively. Red and gray arrow point towards the topological and trivial surface states respectively. (K)-(N) Calculated plots from ab-initio calculations with yellow and gray arrows pointing towards the topological and trivial states. Dotted line is the guide to the eyes at the points where the Fermi arcs terminate. Adopted from [162].

for visualizing these electronic structures is ARPES. In materials like Bi_2Se_3 and Bi_2Te_3 the key signature is a single, gapless Dirac cone on their surface, with a linear dispersion relation protected by time reversal symmetry.

Hsieh et al. [21] were among the first to use ARPES to definitively show a surface Dirac cone in Bi_2Se_3 as shown in Fig. 4.8. Their experiments revealed a beautiful, conical band structure on the material's surface, located within the bulk energy gap. The Fermi level is tuned by exposing the cleaved surface with NO_2 gas in different concentration as denoted by L in Fig. 4.8. This clear observation was the foundational experimental proof for the existence of 3D TIs and their unique surface states.

WSMs are characterized by the existence of chiral Weyl nodes in the bulk. The topological charge of these nodes gives rise to the much celebrated Fermi arcs. These are open-ended surface states that connect the projections of two Weyl nodes of opposite chirality. Unlike the closed loops of a conventional Fermi surface, the non-closed nature of the Fermi arcs is a direct consequence of the chirality of the bulk Weyl nodes, which act as sources and sinks for

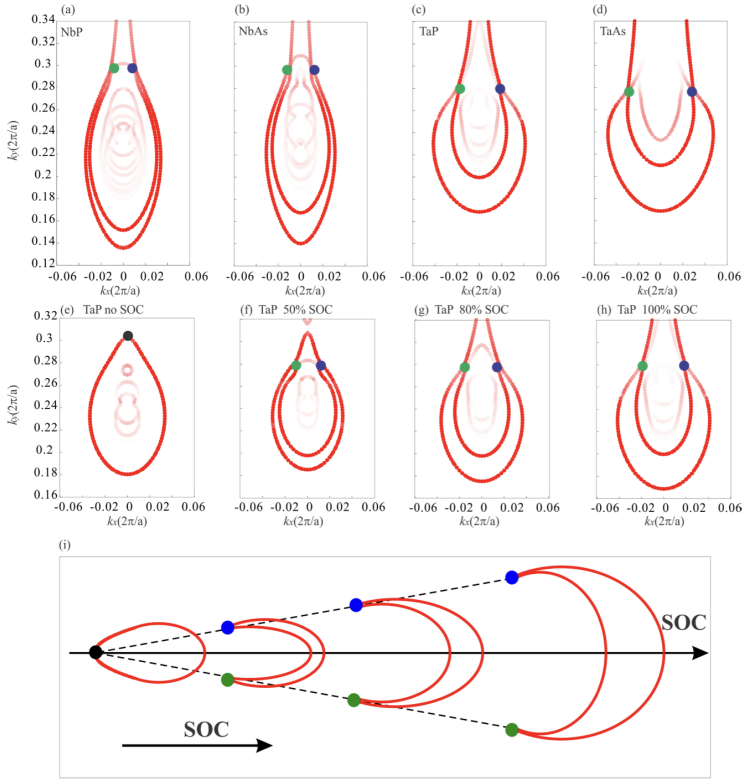

Figure 4.10: (a)-(d) The Fermi surface for NbP, NbAs, TaP, and TaAs, with Weyl points marked with green and blue circles. (e)-(h) Demonstrates the splitting of a closed topologically trivial Fermi circle and generating the Weyl points connected with Fermi arcs. (i) Shows the effect of SOC on the length of the Fermi arcs. Adopted from Ref. [163].

the arcs. The experimental confirmation of the first WSM TaAs came from ARPES, which provided the first direct visualization of the Fermi arcs as shown in Fig. 4.9. In a series of breakthrough papers published in 2015, research teams including Xu et al. [13] used ARPES to show unambiguous, non closed Fermi arcs on the surface of TaAs. This observation was a powerful confirmation of the theoretical predictions and served as a definitive experimental signature of the Weyl semimetal phase. Fermi arcs have been observed in both type I (TaAs) [24] and type II ($MoTe_2$) [162] WSMs. The length of these Fermi arcs is directly correlated with the momentum space separation of the Weyl nodes, a separation that is a direct consequence of the strength of the spin orbit coupling. This connection arises because a Dirac node is protected by both time reversal and inversion symmetry. To create Weyl nodes, one of these symmetries must be broken. Strong spin-orbit coupling, in concert with the broken symmetry, acts as the primary mechanism that splits a single Dirac node into a pair of separated Weyl nodes in momentum space. A stronger SOC typically results in a larger momentum space separation between the Weyl nodes [c.f. Fig. 4.10], which in turn leads to longer Fermi arcs on the material's surface, as they must span the distance between the projected nodes.

Chapter 5

Study of semimetal-insulator interface

As we saw in last chapter, topological insulators are materials which act as insulators in their bulk but entertain conducting boundaries also called edge modes. The remarkable robustness of these edge modes against disorder or non-magnetic impurities protected by the time reversal symmetry only adds to their prominence. We also studied the theoretical underpinning for TIs largely relies on effective models, simplified Hamiltonians that capture the essential low-energy physics. We specifically studied 2D TI HgTe/CdTe quantum wells, the BHZ model aimed at providing an effective Hamiltonian for the band inversion phenomenon. For 3D TIs, like bismuth selenide (Bi_2Se_3) and bismuth telluride (Bi_2Te_3), the effective Hamiltonian took a Dirac-like form, describing a single Dirac cone on the surface. These surface states are composed of massless Dirac fermions, similar to those found in graphene. The robustness of these surface states is a direct consequence of the non-trivial bulk topology, again protected by time-reversal symmetry. The simplicity and predictive power of these Dirac models has been instrumental in guiding experimental efforts, from material synthesis to angle-resolved photoemission spectroscopy (ARPES) measurements, which directly visualizes these iconic Dirac surface states. In parallel research has also been focused on understanding and manipulating the properties of these materials (semimetals) in isolation. The goal of these studies is to exploit the protected surface states of topological insulators for spintronics and quantum computing, and to study the exotic transport phenomena in topological semimetals. However, as the field matured, the focus has branched out naturally from single-component systems to the new and fascinating physics that emerges when different materials are brought into contact. This shift has given rise to the exciting subfield of composite topological systems, where the interfaces between different topological materials are the primary subject of study. By creating interfaces of topological and topologically trivial materials, we can leverage their distinct properties to engineer novel electronic and

spin behaviors. Semimetal-insulator interfaces whether physical or electronic, are where the most dramatic changes in electronic structure occur, giving rise to novel phenomena such as proximity-induced magnetism, tunable band alignments, and the creation of new protected states can be explored and harnessed. At these boundaries, the material's energy bands can undergo a profound transformation, often leading to band inversion and the opening of a gap, which in turn gives rise to new, emergent properties that do not exist in the bulk materials. Examples of this include the formation of topological edge states that allow for dissipationless electron flow and the Quantum Anomalous Hall (QAH) effect, both of which are strictly interfacial phenomena.

Experimentalists have used doping which creates an electronic interface by spatially controlling the concentration of impurities within a material. The boundary between a doped, insulating region and an undoped, semimetallic region becomes an active site for a phase transition. This was exemplified by the first principle calculations [164] showing that doping a topological insulator like Bi_2Se_3, Bi_2Te_3 and Sb_2Se_3 with magnetic impurities would open a band gap at the Dirac point, thus creating an insulating region with a semimetal-like bulk. This interface between the gapped surface state and the trivial bulk is where the QAH effect is predicted to emerge. This was confirmed by observing a quantized Hall resistance plateau at zero magnetic field on the surface of a Bi_2Te_3 and Sb_2Te_3 film doped with chromium and vanadium [29]. Chemical doping has been applied as a precise tool to create and control interfacial transitions. It was showed that nitrogen doping can be used to engineer a metal-to-insulator transition in $SrNbO_3$, leading to a remarkable increase in resistivity that could be leveraged for future electronic devices [165]. Similarly, an application of doping was demonstrated in Ta_2NiSe_5, where potassium deposition was used to precisely control the excitonic insulator-to-semimetal transition, providing a mechanism for actively tuning a material's band structure for optoelectronic applications [166].

While bulk pressure can induce a uniform phase transition, non-uniform pressure or strain can create a sharp, physical interface between two different electronic phases within a single crystal. Inhomogeneous strain provides an alternative to chemical doping. As pressure is applied to an elemental Te crystal, the electronic bands deform, leading to a band-crossing that creates an interface between a trivial semiconductor and a WSM [167]. Similarly, strain engineering, a more localized approach, can be used to create such interfaces with high spatial precision. Using first principles study [168], $PtTe_2$ monolayer demonstrates a critical amount of biaxial tensile strain can induce a topological phase transition from a trivial insulator to a topological insulator. Under axial strain which involves applying a compressive

in plane biaxial strain and a tensile strain perpendicular to the plane, phosphorene shows a topolological phase transition [169]. The phase transition happens in the electronic band structure within the tight binding approximation with the inclusion of the SOC. Moreover, recent study highlights the general potential of strain engineering to induce phase transitions among trivial insulating, semimetallic, and topological phases in a wide variety of 2D materials [170].

Layering different materials in heterostructures and superlattices is the most direct and designed method for creating a sharp, physical semimetal-insulator interface. The unique properties of these interfaces are a result of charge transfer, orbital hybridization, and symmetry breaking at the boundary. The theoretical foundation for creating new topological states in layered structures was established by A. A. Burkov and L. Balents, who proposed a method for realizing a WSM at the interface of a superlattice [151].

Before the advent of the topological insulators the theoretical groundwork for the interface engineering was laid in the 1980s by B. A. Volkov and o. A. Pankratov [171, 172]. They showed that in a composite system like HgCd/CgTe which experiences a smooth inversion of band gap a massive edge state appears at the interface. Within a two band continuum model of a topological heterostructure describing a Dirac node, the resulting states have at least one chiral mode which is topologically robust [173–175]. In this chapter we will study a topological heterostructure which is an interface of insulator and a Weyl semimetal. We model the WSM to be invariant under time reversal symmetry and thus leading to a model with four Weyl node. Such a system is expected to host versatile edge states along the interface,and we begin with carefully modelling the interface in Sec. 5.1.1. We describe the possibilities such an interface posses in Sec. 5.1.2 by describing its phase diagram. Selecting appropriate model we solve the eigenvalue problems to get the energy spectrum in Sec. 5.2. Finally, we discuss our results and observations in Sec. 5.3.

5.1 Building the interface

The success of effective models in TIs naturally paved the way for exploring other topological phases, particularly those where protecting symmetries are broken. We build an effective model for an interface with an insulator and a WSM with a smooth boundary [c.f. Fig. 5.1]. The effective model for a WSM typically is constructed by taking a small energy expansion around the Weyl node of either chirality. This approach is well suited for systematic study of physical phenomenon which are mostly influenced by the Weyl node and its immediate surrounding like behavior of Landau levels in the vicinity of the Weyl node under application

Figure 5.1: Cartoon of an interface of insulator and a Weyl semimetal. The gradient signifies the smooth transition from trivial topological phase to non-trivial topological phase.

of an external magnetic field. On the contrary surface states are special electronic states that are confined to the surface or boundary of a material, existing even when the bulk of the material is an insulator and hence requiring more than just the immediate vicinity of Weyl nodes. The surface states of a Weyl semimetal, known as Fermi arcs, are a direct consequence of the topological nature of the Weyl nodes. When the 3D momentum space of the bulk material is projected onto the 2D surface Brillouin zone, the bulk Weyl nodes also get projected onto this surface. As a single Weyl node is a "monopole" of Berry curvature, a single Fermi arc must emerge from each projected node [147]. Therefore, the Fermi arcs are not closed loops, but rather open segments in the surface Brillouin zone. Each arc connects two projected Weyl nodes of opposite chirality, acting as a "bridge" between them [176]. They represent a unique and dramatic consequence of the famous bulk-boundary correspondence, demonstrating how a 3D bulk property (the Weyl nodes) directly dictates a 2D surface phenomenon (the Fermi arcs).

5.1.1 Semimetal-insulator interface Model

To begin with we consider a two band model for WSM describing two pairs of Weyl nodes making up the semimetal section of the interface. The Hamiltonian expanded in the Pauli matrix basis $\boldsymbol{\sigma} = (\mathbb{I}, \sigma_x, \sigma_y, \sigma_z)$ is given by

$$H = \boldsymbol{N} \cdot \boldsymbol{\sigma} \tag{5.1}$$

the coefficient $\boldsymbol{N} = (N_x, N_y, N_z)$ and the components are given as follows

$$\begin{aligned} N_x &= \Delta_x - \frac{\hbar^2}{2}\left(\frac{q_x^2}{m_x^x} + \frac{q_z^2}{m_z^x}\right) && (5.2)\\ N_y &= \hbar\, c_y\, q_y && (5.3)\\ N_z &= \Delta_z - \frac{\hbar^2}{2}\left(\frac{q_x^2}{m_x^z} + \frac{q_z^2}{m_z^z}\right) && (5.4) \end{aligned}$$

m_i^j where $\{i, j\} \in \{x, z\}$ are the effective masses for the respective direction. c_y is the Fermi velocity in y direction. Δ_x, and Δ_z are the gap parameter which accounts the separation between the Weyl nodes. We note that such a description of WSM is time-reversal invariant in nature, which explains that one pair of Weyl nodes are the Kramer partner of the other pair. To simplify the representation we perform a rotation in the Pauli basis about σ_x by $\pi/2$

$$\begin{aligned} H &= \exp\left(-\frac{\imath\pi}{4}\sigma_x\right) H \exp\left(\frac{\imath\pi}{4}\sigma_x\right)\\ &= N_x\,\sigma_x - N_z\,\sigma_y + N_y\,\sigma_z \end{aligned}$$

It is only natural to work in natural units with $\hbar = c = 1$. We also unify the gap parameters $\Delta = \Delta_x + \imath\Delta_z$, along side we define complex effective masses $1/m_x = 1/m_x^x + \imath/m_x^z$, and $1/m_z = 1/m_z^x + \imath/m_z^z$ giving us the following

$$H = \begin{pmatrix} c_y q_y & \Delta - \frac{1}{2}\left(\frac{q_x^2}{m_x} + \frac{q_z^2}{m_z}\right)\\ \Delta^* - \frac{1}{2}\left(\frac{q_x^2}{m_x^*} + \frac{q_z^2}{m_z^*}\right) & -c_y q_y \end{pmatrix} \quad (5.5)$$

The energy eigenvalues of H are given as follows

$$\begin{aligned} E_\pm &= \sqrt{c_y^2 q_y^2 + |D|^2} && (5.6)\\ &= \pm\sqrt{c_y^2 q_y^2 + \left|\Delta - \frac{1}{2}\left(\frac{q_x^2}{m_x} + \frac{q_z^2}{m_z}\right)\right|^2} && (5.7) \end{aligned}$$

The energy eigenvalues form two 3D surfaces and for $q_y = 0$ the surfaces are controlled by D i.e, $\mathrm{Re}(D) = N_x$ and $\mathrm{Im}(D) = N_z$. As a result the energy surfaces touch only and only for the momenta where $\mathrm{Re}(D) = \mathrm{Re}(D) = 0$. These simultaneous conditions imply that the Weyl nodes appear only if the ellipses made by N_x (say ellipse x) and N_z (say ellipse z) intersect giving the following equations necessary

$$\Delta_x = \frac{1}{2}\left(\frac{q_x^2}{m_x^x} + \frac{q_z^2}{m_z^x}\right) \qquad \text{and} \qquad \Delta_z = \frac{1}{2}\left(\frac{q_x^2}{m_x^z} + \frac{q_z^2}{m_z^z}\right)$$

Its important to note that both these equations must be satisfied simultaneously to have Weyl points. The lack of real valued solutions for the value of momenta leads to opening of a trivial band gap hence describing an insulator.

In order to model a material which is an interface between an Insulator and a WSM, the gap parameter can be made a function of the spatial dimension x. We introduce a smooth change of gap parameter Δ thus we can fulfill the requirements for the existence of the surface states. Hence we introduce the following

$$\Delta_x = \begin{cases} \Delta_1 - \delta_1 & \text{for } x < -l \\ \Delta_1 + \delta_1 \frac{x}{l} & \text{for } |x| \leq l \\ \Delta_1 + \delta_1 & \text{for } x > l \end{cases} \quad \text{and} \quad \Delta_z = \begin{cases} \Delta_2 - \delta_2 & \text{for } x < -l \\ \Delta_2 + \delta_2 \frac{x}{l} & \text{for } |x| \leq l \\ \Delta_2 + \delta_2 & \text{for } x > l \end{cases} \tag{5.8}$$

When tuned appropriately behavior of Δ_x and Δ_z brings an insulator (on the left) and WSM (on the right) together with a smooth transition (with a linear dependence on x) and still a clear boundary. We also denote $\Delta_0 = \Delta_1 + \imath\Delta_2$.

The model can be made much richer by introducing a rotation which would allow the surface states to show diversity. The Weyl nodes can also reoriented by rotating them in the momentum space about the q_y by an angle θ with the following

$$q_z \to q_z \cos\theta - q_x \sin\theta \quad \text{and} \quad q_x \to q_z \sin\theta + q_x \cos\theta$$

It is important to note that this is just a geometric rotation and now a rotation in pseudo-spin. The Hamiltonian stays effectively identical from the perspective of its symmetries. The rotation leads to the addition of a new cross term in $q_z q_x$, and the non diagonal term D now

Figure 5.2: The energy dispersion of the continuum model with four Weyl nodes.

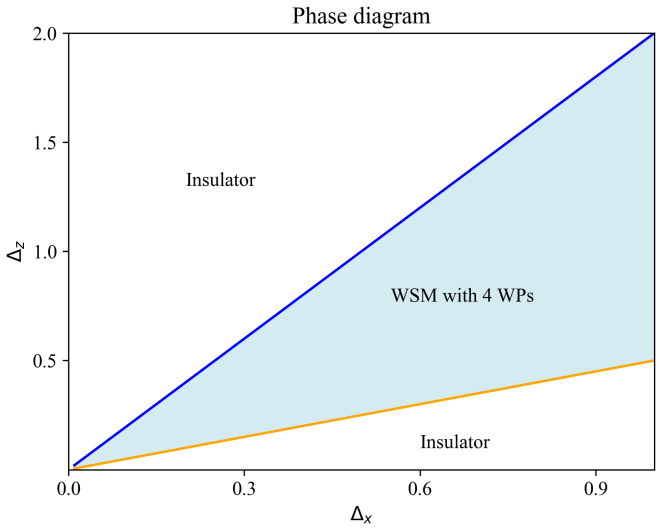

Figure 5.3: Phase diagram for the Hamiltonian, the blue and orange line mark the boundary between the Insulating phase and the Weyl semimetal phase. The insulating phase appears when either both Δ_x and Δ_z are negative or the ellipses realized by them do not intersect. When the right conditions are met the ellipses touch at only two points hence the Hamiltonian hosts two Weyl points. This results in the blue and orange boundaries between WSM and insulator.

takes the following form

$$D = \Delta - \frac{q_z^2}{2}\left(\frac{\cos^2\theta}{m_x^z} + \frac{\sin^2\theta}{m_z^z}\right) - \frac{q_x^2}{2}\left(\frac{\sin^2\theta}{m_x^z} + \frac{\cos^2\theta}{m_z^z}\right) - \frac{q_z q_x \sin 2\theta}{2}\left(\frac{1}{m_x^z} - \frac{1}{m_z^x}\right).$$

5.1.2 Phase space

We have already hinted that the parameters in the system need to be optimised, this happens because the gap parameter along with the effective masses are capable of resulting distinctive features which are different from our required interface. To understand this we begin by noting that the modeled system is not topological in case the ellipses do not intersect in other words $\Delta_x < 0$ or $\Delta_z < 0$ such a choice of parameters result in a gaped system leading in an insulating phase for all real momenta. It is important to note that the eccentricity which is managed by the effective mass cannot be tweaked to change this insulating phase. On the other hand, $\Delta_x > 0$ and $\Delta_z > 0$ can give us degenerate energy states resulting in WSM phase if and only if the the ellipses intersect. The ellipses can be manipulated by the effective masses m_i^j, affecting the location of the intersection and hence the location of the Weyl points. Nevertheless, the Weyl points are located symmetrically about $q_z = 0$ and $q_x = 0$. The gap parameters, Δ_x and Δ_x scale the size of respective ellipses.

We consider a symmetric configuration of Weyl nodes and fix the effective masses ac-

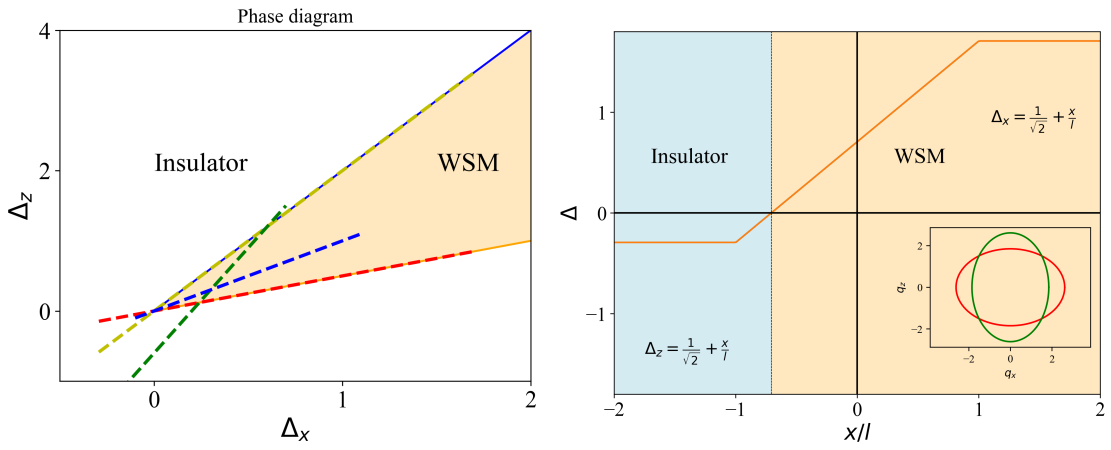

Figure 5.4: (a) Phase space with different cross sections. Blue dashed line corresponds to an interface of Insulator and a WSM with 4 WP. Green dashed line models a sandwiched system i.e. Insulator-WSM-Insulator. (b) Depicts the function dependence of Δ_x and Δ_z on x leading to boundaries between the insulating and topological phase.

cordingly. In our work we consider, $m_x^x = m_z^z = 2$ and $m_z^z = m_z^x = 1$. As x interpolates between $-l$ to l both ellipses change in size at different rates depending upon $\delta_{1,2}$. Hence certain choices of parameters can lead to one of the ellipse enclosing the other and forbidding any intersection of ellipses. We can calibrate $\Delta_{1,2}$ and $\delta_{1,2}$ in such a way that one of the ellipses just about touches the other ellipse at $x = -l$ and they both scale maintaining two intersection points. It is natural to consider a 'phase space' of the interface which describes the topological nature of the materials on either side of the interface. The ellipses can touch along q_x or q_z depending upon the values of chosen parameters. It is easy to determine that these extremes correspond to $\Delta_z\, m_x^z = \Delta_x\, m_x^x$ and $\Delta_z\, m_z^z = \Delta_x\, m_z^x$ respectively. For the chosen effective masses the two conditions described above result in the phase of interface which links insulator and a WSM with two Weyl nodes. This delicate balance separates the phase space of the interface of two kinds as shown in Fig. 5.3. The boundary in the phase space as shown in Fig. 5.3 in blue describes the interface with insulator and a WSM with Weyl nodes appearing along q_z and similarly the boundary in orange has a WSM with Weyl nodes along q_x. Scaling the ellipse now turns out to be a tuning factor which brings about the transition of phase of the interface. The dependence of gap parameter on the spatial dimension x produces the phase space and parameterization of $\Delta_{x,z}$ with appropriate values leads to sampling of the phase diagram [Fig. 5.4(a)] with a linear cut of finite length. The

introduced parametrization of $\Delta_{x,z}$ can be represented in a form independent of x as follow

$$\Delta_x = \Delta_1 + \delta_1 \frac{x}{l}, \quad \text{and} \quad \Delta_z = \Delta_2 + \delta_2 \frac{x}{l} \tag{5.9}$$

$$\frac{\Delta_x - \Delta_1}{\delta_1} = \frac{\Delta_z - \Delta_2}{\delta_2} \tag{5.10}$$

$$\Delta_z = \left(\frac{\delta_2}{\delta_1}\right)\Delta_x + \delta_2\left(\frac{\Delta_2}{\delta_2} - \frac{\Delta_1}{\delta_1}\right) \tag{5.11}$$

As mentioned previously, $\Delta_{x,z}$ in this form independent of x, corresponding to any finite slice across the phase diagram we can model an interface with with different stacking as shown in Fig. 5.4(a). The finite nature of slice in phase diagram does not imply the a finite size of the insulating region or the topological region along the x direction. This will turn-out to be not very crucial with respect to the solution to the problem under consideration and will be revisited in Sec. 5.2. This re-imagined form of the gap parameters allow us to neatly classify different possible interface permitted as depicted in Fig. 5.4(a). The Interface can be modified by changing the values of parameters to have

- One boundary with insulator on the left and WSM phase on the right, with four Weyl nodes as shown in blue in Fig. 5.4(a) resulting from the choice of parameters shown in Fig. 5.4(b)
- An interface formed by sandwiching WSM with four Weyl nodes with insulators on either end. The four Weyl points merge into two Weyl points before the topological phase transitions to trivial phase forming the insulating region. Such an interface has resemblance with the quantum wells and is shown in green in Fig. 5.4(a).
- Apart from physical possibilty the model also allows for an interface of insulator and a WSM with two Weyl nodes as shown in yellow and red in Fig. 5.4(a).

We will choose parameters which results in the interface of first kind, as we sought out to.

5.2 Analytical and numerical method techniques

We wish to find the energy spectrum the Hamiltonian in the entire interface i.e. $x \in (-\infty, \infty)$. The gap parameter Δ changes the functional form at $\pm l$ and thus manifesting a piecewise form. The presence of the spatial dimension x in the Hamiltonian q_x is no longer a good quantum number due to $[x, q_x] = \imath$. We choose to solve for the wavefunction across the interface as the function of the spatial dimension i.e. $|\psi\rangle = \psi(x, q_z, q_y)$. We know from elementary quantum mechanics that the wavefunction for the interface should be continuous.

As we look for the wavefunction solution to the eigenvalue problem as a function of spatial dimension x, at the boundaries $\pm l$ due to the presence of q^2 term in the Hamiltonian the wavefunction is additionally required to be doubly differentiable at $x = \pm l$.

The wavefunction in the clamped regions i.e. for $|x| > l$ is a 2 component Dirac spinor and the phase factor is given as follow

$$\text{phase} \quad = \quad \begin{cases} e^{\imath \boldsymbol{k}_i \cdot \boldsymbol{r}} & \text{for } x < -l \\ e^{-\imath \boldsymbol{k}_t \cdot \boldsymbol{r}} & \text{for } x \geq l \end{cases} \tag{5.12}$$

here $\boldsymbol{k}_i$ is the momentum vector in the insulating region of the interface corresponding to $x < -l$ and similarly $\boldsymbol{k}_t$ is the momentum vector for topological region for $x > l$. The momenta must satisfy the eigenvalue energy relation

$$E = \pm \sqrt{c_y^2 \, k_y^2 + \left| \Delta_{i,t} - \frac{1}{2} \left(\frac{k_x^2}{m_x} + \frac{k_z^2}{m_z} \right) \right|^2} \tag{5.13}$$

and the equation must be satisfied for both insulating region ($\boldsymbol{k} = \boldsymbol{k}_i$) and the topological region ($\boldsymbol{k} = \boldsymbol{k}_t$), and E is the energy of the interface. Assuming the insulating band gap is given by E_{bg}, in case the energy $|E| < E_{bg}/2$, then not all components $\boldsymbol{k}_i$ can be real valued to satisfy the energy equation for the interface. This fact forces the wave phase to takes a decaying nature in the insulating phase. This restricts the wavefunction energetically within the topological region.

The introduction of x quantizes the energy spectrum, the allowed energy states can be found by constructing the eigenfunction in terms of the Harmonic oscillator states. To begin with we define $m = |m_x|$, and $\delta = \delta_1 + \imath \delta_2$ allows us to write the annihilation operator

$$a \quad = \quad \left(\frac{m|\delta|}{4\, l^2} \right)^{\frac{1}{4}} \left(x - \imath \frac{l}{\sqrt{m|\delta|}} q_x \right) \tag{5.14}$$

The creation and annihilation operators satisfy the anti commutation relation $[a^\dagger, \, a] = 1$. This choice of annihilation operator brings out an inherent length scale in the system

$$\alpha = \left(\frac{l^2}{m|\delta|} \right)^{\frac{1}{4}} \tag{5.15}$$

It is important to note that the choice for a is not unique and we will revisit this point later in this section. The off diagonal term from the Hamiltonian can be written in terms of these

creation and annihilation operators which gives us the following,

$$D = \Delta + \delta\frac{x}{l} - \frac{1}{2}\left(\frac{q_x^2}{m_x} + \frac{q_z^2}{m_z}\right) \tag{5.16}$$

$$= \Delta - \frac{q_z^2}{m_z} + \frac{\delta}{(4m|\delta|l^2)^{\frac{1}{4}}}(a^\dagger + a) + \frac{1}{2m_x}\left(\frac{m|\delta|}{4l^2}\right)^{\frac{1}{2}}(a^\dagger - a)^2 \tag{5.17}$$

The wavefunction can be constructed using the harmonic oscillator states $|n\rangle$ which are solution to

$$\left(a^\dagger a + \frac{1}{2}\right)|n\rangle = N|n\rangle \tag{5.18}$$

here $N = n + 1/2$. The wavefunction in the linear region of the interface itself being is a two component spinor. Each of component of wavefunction is composed of all harmonic oscillator states and thus has a coherent states-like structure as follow

$$\psi_n^{\pm}(x,\, q_z,\, q_y) = \sum_{i=0}^{\infty}\begin{pmatrix}\alpha_{i,n}^{\pm}(q_z,\, q_y)|i\rangle \\ \beta_{i,n}^{\pm}(q_z,\, q_y)|i\rangle\end{pmatrix} \tag{5.19}$$

Here $\pm$ correspond to the conduction or valance band. We solve for the coefficients $\alpha_{i,n}^{\pm}$ and $\beta_{i,n}^{\pm}$ numerically.

The complete solution for the entire interface appears after we match the boundary condition which in this case puts constrain on the phase of Dirac spinor for $|x| > l$. As we are not studying the reflective or transmissive properties of the interface we can get away with matching. We note that the eigenvectors are not square integrable in q_z and in this sense q_z only parametrizes the wavefunction.

5.2.1 Nature of solution

We discuss the interface of first kind as marked by blue in Fig. 5.4(a) corresponding to the parameters plotted in Fig. 5.4(b). In the process of choosing a cut across the phase space we end up fixing δ and thus the only free parameter left in the model is l which entirely controls the length scale α ultimately the model. It is the harmonic oscillator states which shape up the wavefunction. These states are themselves localized in a parabolic potential and hence have a Gaussian spread across x given as follows

$$|n\rangle \propto e^{-x^2/\alpha^2} \tag{5.20}$$

$$= \exp\left(-\frac{x^2}{l^2}\frac{l^2}{\alpha^2}\right) = \exp\left(-\eta^2\frac{x^2}{l^2}\right). \tag{5.21}$$

Here $\eta = \sqrt{l^2 m|\delta|}$ i a dimensionless quantity. The wavefunction as a function of x/l has a spread (standard deviation) inversely related to l as the above makes clear. Due to presence of multiple energy and length scales, the wavefunction when represented as a function of x the spread shows a direct proportionality with l. The Gaussian spread implies that the wavefunction is localized around a value of x which depends upon $\alpha^{\pm}_{i,n}(q_y, q_z)$ and $\beta^{\pm}_{i,n}(q_y, q_z)$. It is also fruitful to note that the momentum space wavefunction which is the Fourier partner of the $\psi_n(x)$ will also be localized due to the Gaussian nature of $|n\rangle$. Nevertheless, l has the inverse effect on the spread of momentum space wavefunction compared to the real space wavefunction. Hence increase in l, results decrease in the spread of momentum space wavefunction.

The wavefunction is the result of quantization of the entire interface, meaning, the final energy eigenvalues and wavefunction itself accounts for not only the insulating phase but also the topological phase. This topological phase has Weyl nodes and quantization takes into account the variation in their separation which happens as x changes. However, the gap parameter Δ does not experiences any change due to l, as far as it is concerned it depends upon δ and gap at $x = 0$ i.e. Δ_0. This is a vital observation as the size of ellipses is controlled by Δ, its independence from l implies that the ellipses in the momentum space do not get affected by l either.

Due to the quantization the eigen energies are no longer function of either of x or q_x. Consider a real space picture which involves taking a projection of q_x on $x - q_z$ plane. The momentum space picture can be imagined as aggregation of all slices of momentum $q_x - q_z$ (assuming $q_y = 0$ for simplicity) corresponding to every values of x. It might appear that such a projection on $q_x - q_z$ plane loses the boundary of the system. But it turns out that the boundary is now interpreted as the lack of intersection of the ellipses. Effectively, both pictures are a trade-off between x and q_x and play an important part in understanding the system. The observations made above are basically real space and momentum space picture of the eigenvalue problem. The consequence of the localization of real space wavefunction along x implies that the sampling by the wavefunction of the region with Weyl points with large separation (rooting from large x) will always be suppressed exponentially. Similarly, the insulating region with large band gap E_{bg} (resulting from large $-x$) will also be suppressed exponentially. Additionally, in the momentum space picture the observation asserts that the the spread of momentum space wavefunction decreases with l. Prompting a sampling of momentum space i.e. $q_x - q_z$ plane where the Weyl points are located with a sharp momentum space wavefunction as the separation of Weyl points in $q_x - q_z$ plane remains unaffected by

l.

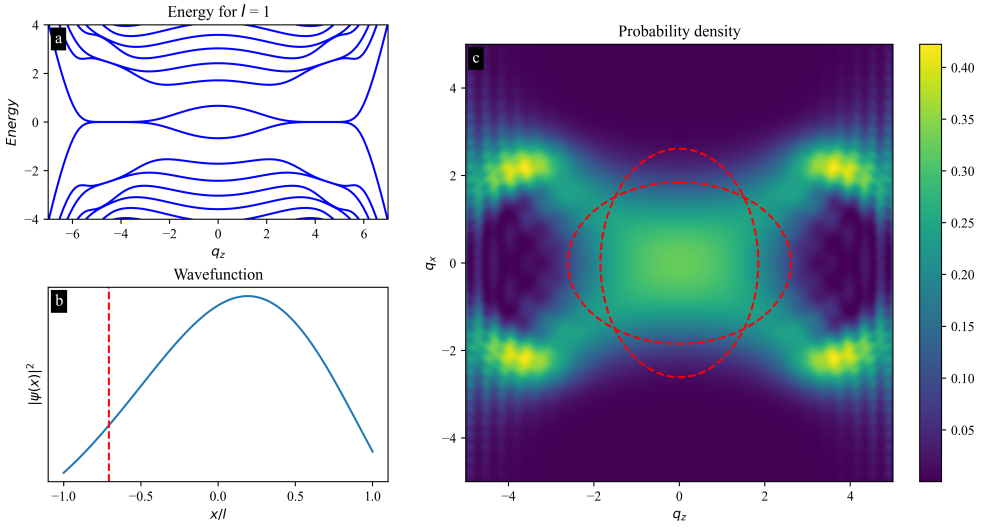

Figure 5.5: Panel shows the (a) dispersion of allowed energy levels, (b) the wavefunction density for $n = +1$ band at $q_z = 0$, and (c) the map of $|\psi(q_x, q_z)|^2$ for $n = +1$ band. The red-dashed line on (b) marks the boundary where the insulator transitions to the WSM phase. Red ellipse correspond to the ellipse of WSM region for $x = l$. The parameters chosen are from the Fig. 5.4(b) and $l = 1$.

The interface modeled here is a smooth (linear) transition of the gap parameter but the topological phase transition from insulating phase to WSM phase is abrupt. The parameters chosen the interface has the topological boundary for x_0, where the intersection of ellipses lead to real valued solution. For the chosen parameters as shown in Fig. 5.4(b) is at $x_0 = -l(\Delta_1/\delta_1) = -l/\sqrt{2}$.

5.3 Energy spectrum of the interface

As the wavefunction is not square-integrable in q_z, we treat it as the parameter. We numerically solve the eigenvalue equation varying q_z. Fig. 5.5(a) shows some allowed bands around zero energy for $l = 1$. The spectrum is calculated assuming $q_y = 0$. q_y can be reinstated using Eq. (5.6) for small value of energy the dispersion is quadratic along q_y. As expected the energy spectrum is symmetric about $q_z = 0$. The energy eigen states shows degeneracy between E_0^+ and E_0^- for certain range of q_z and the spectrum is gapped around $q_z = 0$. All adjacent energy bands beyond $E_0^\pm$ are degenerate within the same range of q_z. Fig. 5.5(b) plots the square of the absolute value of the wavefunction for $q_z = 0$ as the function of x/l. The red dashed line marks the boundary between the insulating and WSM phase of the interface. Fig. 5.5(c) is the density plot for the square of the absolute value of the momentum space wavefunction in $q_x - q_z$ plane. The red dashed line shows the ellipses

at $x = l$ marking the end of linear regime of the gap parameter.

We recall from previous discussion that the wavefunction is localized and this introduces an effective natural smooth boundary for the region $|x| > l$. The states remain confined around the boundary of the topological phase transition (x_0). Such a localization is not novel and had already been noted first by Volkov and Pankratov with gap parameter which varies smoothly over the interface [171, 172]. The localization of the energy states has been noted even for the gap parameter which is linear around the topological phase boundary and clamped beyond some length [173, 174]. These localized states are the aforementioned VP states and they generically appear in topological heterostructures as the interface model considered here. We can exploit this confinement by choosing an l which leads to momentum space wavefunction to be localized within the purview of the ellipses resulting from the clamped region of WSM phase (ellipses at $x = l$) i.e. red dashed region of momentum space as shown in Fig. 5.5(c).

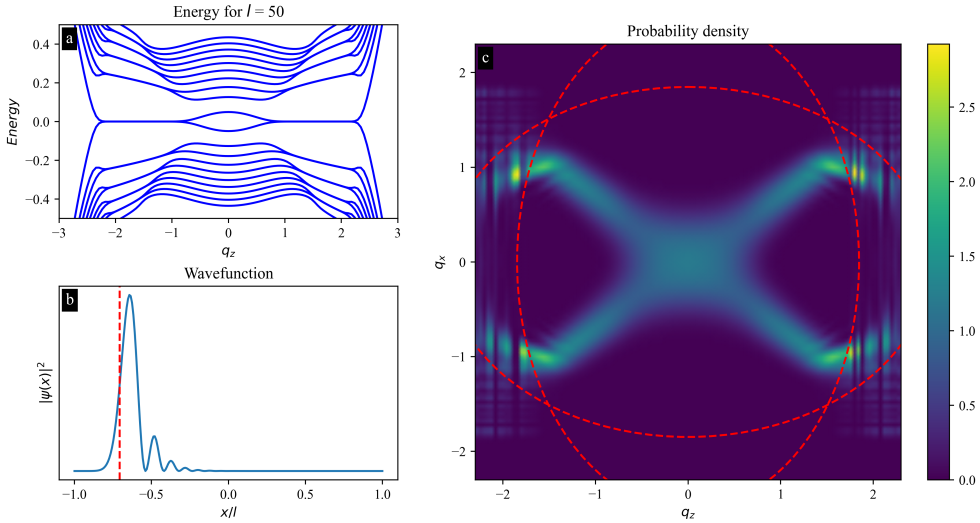

Figure 5.6: Panel shows the (a) energy bands, (b) wavefunction density, and (c) map of the momentum space wavefunction density same as Fig. 5.5 for $l = 50$.

Natural confinement of the wavefunction within the linear range ($x \in [-l, l]$) of the gap parameter because of the Gaussain weight, the wavefunction behaves closely mimics the exact solution of the problem in the clamped region ($|x| > l$) as well. A qualitative inspection leads us to conclude that $l = 50$ is best suited as the solution for the interface. A comparison of the wavefunctions for the case of $l = 1$ (Fig. 5.5(b)) and $l = 50$ (Fig. 5.6(b)) shows a clear localization of the wavefunction for $q_z = 0$. This seeming opposite behavior of wavefunction was explained earlier and is the artifact of the result being represented as x/l.

5.3.1 Spectral Analysis of the interface

The geometry of the interface is such that the system is unbounded along y and z direction. The boundary between insulator and the WSM is located along x. The bulk boundary correspondence states that the topological properties of a material's bulk directly dictate the existence and properties of protected, conducting states on its lower dimensional boundary (surface or edges). When a 3D bulk insulator and a 3D topological material (WSM in our

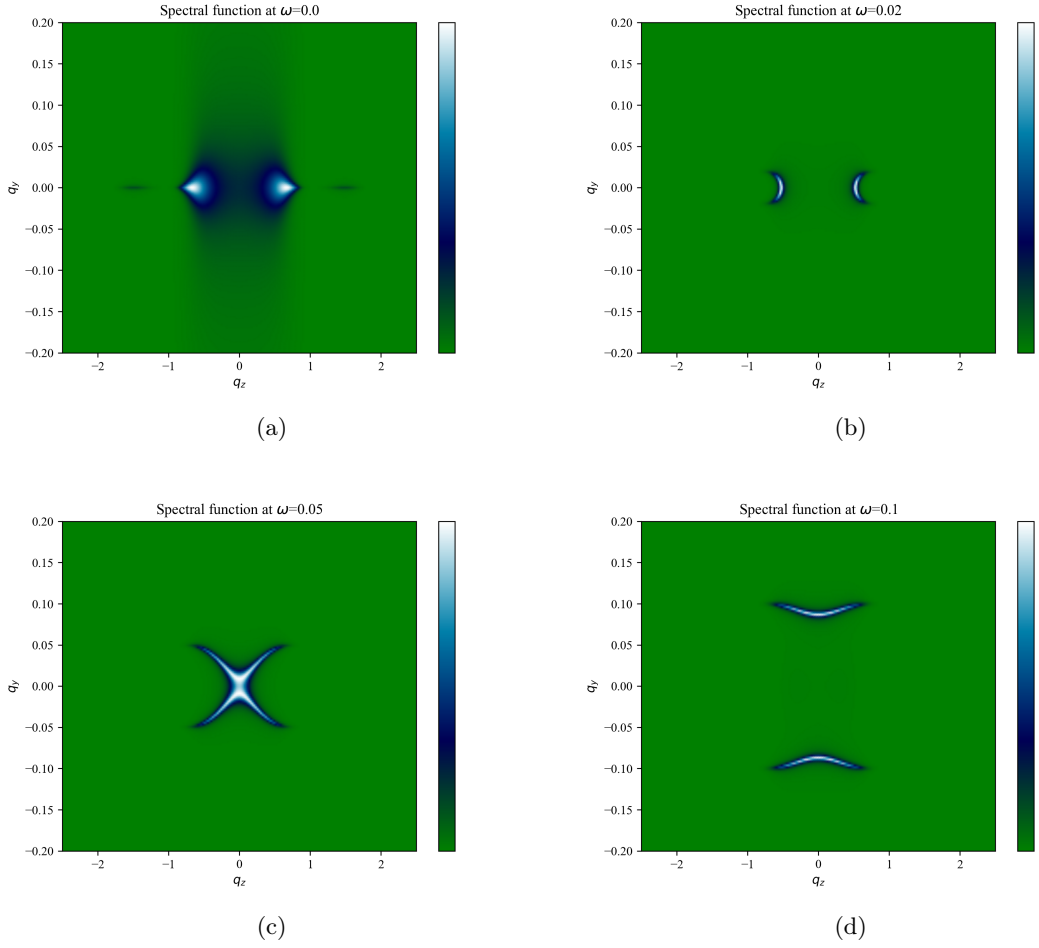

Figure 5.7: The spectral function evaluated for the interface at different frequencies ω. The integral of the spectral function is evaluated for $w = 0.2l$ around the boundary of the interface at $x_0 = -l/\sqrt{2}$ for the chosen parameters.

case) are brought together, a gapless interface state forms at their shared boundary. This is the direct consequence of the bulk boundary correspondence and the difference in their topological invariants. The topological invariant of a system cannot change unless the energy gap closes. Since the topological material and the normal insulator have different invariants, their interface acts as a domain wall where the topology must change. For this transition to occur, the energy gap must close at the interface, which results in the formation of gapless

interface states. As seen in Fig. 5.6(a) the energy gap closes and making the topologically protected surface states (at the boundary of the interface $x = x_0$) inevitable.
To observe these surface states we write down the following spectral function

$$\mathcal{A}(\omega) \quad = \quad \mathrm{Im}\left[\lim_{\epsilon\to 0}\int_{x_0-w}^{x_0+w} dx \sum_n \frac{\langle\psi_n(q_z,q_y;x)|\psi_n(q_z,q_y;x)\rangle}{\omega - E_n(q_z,q_y) + \imath\epsilon}\right] \tag{5.22}$$

here we measure the contribution from the states around the energy ω from the whole bulk which is ensured by summing over all states. To make sure we only observe the edge the integral is performed around the boundary x_0 of the interface within a width of $2w$. Fig. 5.7 shows the evaluated spectral function around the boundary for different ω. As $\epsilon \to 0$ in Eq.(5.22) the contribution from states with energy not around ω falls off.

In the limit $\epsilon \to 0$, the wavefunction density becomes the kernel for the Dirac delta function. Hence the zero value of spectral function implies that the wavefunction density from the effective edge $(x_0 - w,\, x_0 + w)$ has no contribution. The peaks in the Fig. 5.7(a) appear right around the $q_z \sim \pm 1$ which is shared by the q_z where the energy gap closes (Fig. 5.6(a)) the first time as we move from $q_z = 0$. The integral in the spectral function over the entire interface (x) would be exactly equal to the wavefunction density in the momentum space, however the finite limit around the boundary, introduces an oscillating weight. Nonetheless, the integral is still a carefully chosen 'average' of either certain range x or q_x with some oscillating weight. It is quite peculiar that the spectral function in Fig. 5.7(a) is zero beyond $|q_z| > 1$, and this happens because the wavefunction density in the degenerate part of the energy section for $n = \pm 1$ comes from the bulk WSM phase. This can be argued based on a simple fact that energy is smaller that insulating band gap energy hence will always be exponentially suppressed. The integral of wavefunction density gives a zero result as we probe the higher energy in Fig. 5.7(b), therefore we observe that the edge states are open curves (half moons) and symmetric about $q_y = 0$ and $q_z = 0$. For the degenerate region of the spectrum for $n = \pm 1$, the energy for non zero q_y is simply given by $E_1^{\pm} = \pm|q_y|$. The end points of half moon are with opposite chirality. Increasing the ω transforms the surface states as shown in Fig. 5.7(b)-(d). The half moons grow larger and due to the presence of the nondegenerate dome around $q_z = 0$ having a near edge contribution as shown in Fig. 5.6(a)-(b). The half moons warp as the frequency is increased and eventually merge at the energy near the top of the dome [c.f. Fig. 5.6(a)] as shown in Fig. 5.7(c). A further increase in the frequency shows separated arms dispersing along q_z as two open-ended curves as shown in Fig. 5.7(d).

In summary, we modeled an interface with a diverse phase which includes trivial and

topological regions [c.f. Fig. 5.3]. Choosing the set of parameters which lead to an interface of an insulator and WSM, we numerically solved for the energy spectrum for the interface. In doing so we broke the inversion symmetry of the Hamiltonian by introducing the x dependence within the gap parameter. Owing to the Gaussian nature of the solutions, the eigen states experience a natural cutoff. We exploited this fact to argue that the energy spectrum for large enough l ($l = 50$ for our case) best approximates the solution to the interface with clamped gap parameters beyond $|x| \geq l$. Finally, using the spectral function peaked around the boundary of the interface we demonstrated that the edge states undergo a chiral flip as they connect points in the momentum space with opposite chirality.

Chapter 6

Summary

This thesis explores the fascinating properties of states that are confined to the edges and boundaries of 1D and 3D topological materials. Chapter 1 provided a comprehensive overview of these systems and their unique characteristics. The study began with a general introduction to the observable effects of topology in condensed matter physics. We first discussed the QHE, which results from the quantization of charge carrier orbits, and then extend this discussion to related phenomena such as the SQHE and the AQHE. This foundation provides the necessary context for understanding more complex systems. Moreover, the thesis reviews prominent edge modes, focusing specifically on the MBS that appear on 1D topological superconductors. This section delves into the unique, non-trivial properties of these modes. The Chapter concludes by presenting a detailed classification of topological materials using the universally recognized framework, the "tenfold way". This classification system is essential for organizing and understanding the diverse landscape of topological phases.

The classification allows us the crucial points of distinction of topological materials, from the dimensionality of their boundaries to the different mathematical invariants that describe their topological properties. 1D topological materials are distinguished from 3D topological insulators by the dimensionality of their boundaries and the nature of their topological invariants. In 1D systems, the topology is described by an integer winding number that dictates the existence of robust, zero-energy states localized at the material's 0D ends. In contrast, 3D topological insulators are characterized by a gapped bulk with protected, gapless metallic states residing on their 2D surfaces, where their topology is governed by a $\mathbb{Z}_2$ invariant. This fundamental difference in their topological descriptions leads to distinct boundary states: localized end states in 1D and extended surface states in 3D.

In Chapter 2 we began with the SSH model to demonstrate the notion of topological

invariant in a 1D materials. Expanding the model around the degenerate point in the Brillouin zone, we arrived at the effective model for SSH model around the degenerate point. A spatially varying mass term introduced which led to the emergence of edge mode around the boundary of the effective model. We further reviewed the superconducting nanowire system which borrow superconductivity due to proximity effect. The Kitaev's chain formed the basis of our discussion, we revisited the edge modes associated to the degenerate zero energy states of the Kitaev chain. Finally, we discussed the topological phase and the experimental advances pertaining the edge modes in spin-full nanowires with ferromagnetic and anti-ferromagnetic ordering.

We presented our results in the Chapter 3 on the study of 1D structure made of coupled nanowires. We used the foundational techniques introduced in the Chapter 2 to study the topological phase of the ladder system. We found that the topological phase of the ladder in the weakly coupled regime is composed of the topological phase of a single nanowire with altered chemical potential. However, this approximation deviates as the strength of Rashba SOC between wires, η is increased. The nonlinear composition of topological phases of single nanowire creates unexpected patterns which ultimately lead to winding number ± 3. The finite ladder system with open boundary condition hosts zero energy modes which are the MBS. Additionally, the energy spectrum also has degenerate energy bands within the superconducting gap. The LDOS associated with the degenerate bands is localized at the edge of the ladder.

We discussed the bulk topological materials in the Chapter 4, wherein we take a similar route as earlier and introduce the basic notions used in quantifying the topological properties of bulk materials. We demonstrated the consequences of the non-trivial topological characteristics in models based on 2D honeycomb lattice. We advanced our discussion to with BHZ model, an effective model designed to capture the band inversion in HgTe/CdTe quantum wells. It is the BHZ model which forms the bridge between the composite 2D materials to 3D topological materials and this was shown in the 3D version of BHZ model. Naturally, the 3D BHZ model gave way to discuss the Dirac fermions and later Weyl fermions which are the characteristic quasi-particles of Dirac and Weyl semimetals, respectively. Such topological quasi-particles in BZ lead to localised states on the 2D surface of the 3D material. We discussed extensively the experimental findings of various types of topological materials like topological insulators, Weyl semimetals, and heterostructures.

The Chapter 5 constituted our results on the study of an interface of insulator and a WSM. Starting with a time reversal effective model of WSM, we designed a Hamiltonian

with a spatially varying gap parameter resulting in the interface. We explored the topological behavior of the interface depending upon the chosen values of gap parameter. Fixing our model parameters which lead to a insulator-WSM interface, we solve the eigenvalue problem numerically. We note that the eigenstates are naturally confined due to the Gaussian weight of the basis states. The natural confinement of the eigenstates allows us to bypass the matching the boundary values of the wavefunction for appropriate value of l. We observe that the allowed spectrum shows degeneracy with adjacent energy eigenstates. We study the associated edge modes using the spectral function for $\omega = (0, 0.1)$ range.

Bibliography

[1]K. v. Klitzing, G. Dorda, and M. Pepper, "New method for high-accuracy determination of the fine-structure constant based on quantized Hall resistance", Phys. Rev. Lett. **45**, 494 (1980).

[2]K. von Klitzing, "The quantized Hall effect", Rev. Mod. Phys. **58**, 519 (1986).

[3]D. J. Thouless, M. Kohmoto, M. P. Nightingale, and M. den Nijs, "Quantized Hall conductance in a two-dimensional periodic potential", Phys. Rev. Lett. **49**, 405 (1982).

[4]A. Y. Kitaev, "Unpaired Majorana fermions in quantum wires", Physics-Uspekhi **44**, 131 (2001).

[5]C. L. Kane and E. J. Mele, "Z_2 topological order and the quantum spin Hall effect", Phys. Rev. Lett. **95**, 146802 (2005).

[6]B. A. Bernevig, T. L. Hughes, and S.-C. Zhang, "Quantum spin Hall effect and topological phase transition in HgTe quantum wells", Science **314**, 1757 (2006).

[7]B. A. Bernevig and S.-C. Zhang, "Quantum spin hall effect", Phys. Rev. Lett. **96**, 106802 (2006).

[8]D. C. Tsui, H. L. Stormer, and A. C. Gossard, "Two-dimensional magnetotransport in the extreme quantum limit", Phys. Rev. Lett. **48**, 1559 (1982).

[9]R. B. Laughlin, "Anomalous quantum Hall effect: an incompressible quantum fluid with fractionally charged excitations", Phys. Rev. Lett. **50**, 1395 (1983).

[10]X.-L. Qi and S.-C. Zhang, "Topological insulators and superconductors", Rev. Mod. Phys. **83**, 1057 (2011).

[11]Y. Zhang, K. He, C.-Z. Chang, C.-L. Song, L.-L. Wang, X. Chen, J.-F. Jia, Z. Fang, X. Dai, W.-Y. Shan, S.-Q. Shen, Q. Niu, X.-L. Qi, S.-C. Zhang, X.-C. Ma, and Q.-K. Xue, "Crossover of the three-dimensional topological insulator Bi_2Se_3 to the two-dimensional limit", Nature Physics **6**, 584 (2010).

[12]V. Mourik, K. Zuo, S. M. Frolov, S. R. Plissard, E. P. A. M. Bakkers, and L. P. Kouwenhoven, "Signatures of Majorana fermions in hybrid superconductor-semiconductor nanowire devices", Science **336**, 1003 (2012).

[13]S.-Y. Xu, I. Belopolski, N. Alidoust, M. Neupane, G. Bian, C. Zhang, R. Sankar, G. Chang, Z. Yuan, C.-C. Lee, S.-M. Huang, H. Zheng, J. Ma, D. S. Sanchez, B. Wang, A. Bansil, F. Chou, P. P. Shibayev, H. Lin, S. Jia, and M. Z. Hasan, "Discovery of a Weyl fermion semimetal and topological Fermi arcs", Science **349**, 613 (2015).

[14]R. G. Clark, J. R. Mallett, S. R. Haynes, J. J. Harris, and C. T. Foxon, "Experimental determination of fractional charge e/q for quasiparticle excitations in the fractional quantum Hall effect", Phys. Rev. Lett. **60**, 1747 (1988).

[15]X. Lin, R. Du, and X. Xie, "Recent experimental progress of fractional quantum Hall effect: 5/2 filling state and graphene", National Science Review **1**, 564 (2014).

[16]C.-X. Liu, S.-C. Zhang, and X.-L. Qi, "The quantum anomalous Hall effect: theory and experiment", Annu. Rev. Condens. Matter Phys. **7**, 301–321 (2016).

[17]M. Kohmoto, "Topological invariant and the quantization of the Hall conductance", Annals of Physics **160**, 343 (1985).

[18]M. König, S. Wiedmann, C. Brüne, A. Roth, H. Buhmann, L. W. Molenkamp, X.-L. Qi, and S.-C. Zhang, "Quantum spin Hall insulator state in HgTe quantum wells", Science **318**, 766 (2007).

[19]SPECSGROUP - SPECS GmbH, *SPM, STM, AFM*, https://www.specs-group.com/specsgroup/knowledge/methods/detail/spm-stm-afm/ (visited on 09/10/2025).

[20]Yang Lab, University of Chicago, *Instrumentation*, https://yanglab.uchicago.edu/instrumentation/ (visited on 09/10/2025).

[21]D. Hsieh, Y. Xia, D. Qian, L. Wray, J. H. Dil, F. Meier, J. Osterwalder, L. Patthey, J. G. Checkelsky, N. P. Ong, A. V. Fedorov, H. Lin, A. Bansil, D. Grauer, Y. S. Hor, R. J. Cava, and M. Z. Hasan, "A tunable topological insulator in the spin helical Dirac transport regime", Nature **460**, 1101 (2009).

[22]S. Wu, V. Fatemi, Q. D. Gibson, K. Watanabe, T. Taniguchi, R. J. Cava, and P. Jarillo-Herrero, "Observation of the quantum spin Hall effect up to 100 kelvin in a monolayer crystal", Science **359**, 76 (2018).

[23]B. Q. Lv, S. Muff, T. Qian, Z. D. Song, S. M. Nie, N. Xu, P. Richard, C. E. Matt, N. C. Plumb, L. X. Zhao, G. F. Chen, Z. Fang, X. Dai, J. H. Dil, J. Mesot, M. Shi, H. M. Weng, and H. Ding, "Observation of Fermi-arc spin texture in TaAs", Phys. Rev. Lett. **115**, 217601 (2015).

[24]B. Q. Lv, H. M. Weng, B. B. Fu, X. P. Wang, H. Miao, J. Ma, P. Richard, X. C. Huang, L. X. Zhao, G. F. Chen, Z. Fang, X. Dai, T. Qian, and H. Ding, "Experimental discovery of Weyl semimetal TaAs", Phys. Rev. X **5**, 031013 (2015).

[25]F. Arnold, C. Shekhar, S.-C. Wu, Y. Sun, R. D. dos Reis, N. Kumar, M. Naumann, M. O. Ajeesh, M. Schmidt, A. G. Grushin, J. H. Bardarson, M. Baenitz, D. Sokolov, H. Borrmann, M. Nicklas, C. Felser, E. Hassinger, and B. Yan, "Negative magnetoresistance without well-defined chirality in the Weyl semimetal TaP", Nat. Commun. **7**, 11615 (2016).

[26]H. Zheng and M. Zahid Hasan, "Quasiparticle interference on type-I and type-II Weyl semimetal surfaces: a review", Advances in Physics: X **3**, 1466661 (2018).

[27]H. Inoue, A. Gyenis, Z. Wang, J. Li, S. W. Oh, S. Jiang, N. Ni, B. A. Bernevig, and A. Yazdani, "Quasiparticle interference of the Fermi arcs and surface-bulk connectivity of a Weyl semimetal", Science **351**, 1184 (2016).

[28]R. Li, J. Li, L. Wang, J. Liu, H. Ma, H.-F. Song, D. Li, Y. Li, and X.-Q. Chen, "Underlying topological Dirac nodal line mechanism of the anomalously large electron-phonon coupling strength on a be (0001) surface", Phys. Rev. Lett. **123**, 136802 (2019).

[29]C.-Z. Chang, J. Zhang, X. Feng, J. Shen, Z. Zhang, M. Guo, K. Li, Y. Ou, P. Wei, L.-L. Wang, Z.-Q. Ji, Y. Feng, S. Ji, X. Chen, J. Jia, X. Dai, Z. Fang, S.-C. Zhang, K. He, Y. Wang, L. Lu, X.-C. Ma, and Q.-K. Xue, "Experimental observation of the quantum anomalous Hall effect in a magnetic topological insulator", Science **340**, 167 (2013).

[30]R. M. Lutchyn, E. P. A. M. Bakkers, L. P. Kouwenhoven, P. Krogstrup, C. M. Marcus, and Y. Oreg, "Majorana zero modes in superconductor–semiconductor heterostructures", Nat. Rev. Mater. **3**, 52 (2018).

[31]D. Wang, L. Kong, P. Fan, H. Chen, S. Zhu, W. Liu, L. Cao, Y. Sun, S. Du, J. Schneeloch, R. Zhong, G. Gu, L. Fu, H. Ding, and H.-J. Gao, "Evidence for Majorana bound states in an iron-based superconductor", Science **362**, 333 (2018).

[32]J. Wiedenmann, E. Bocquillon, R. S. Deacon, S. Hartinger, O. Herrmann, T. M. Klapwijk, L. Maier, C. Ames, C. Brüne, C. Gould, A. Oiwa, K. Ishibashi, S. Tarucha, H. Buhmann, and L. W. Molenkamp, "4π-periodic Josephson supercurrent in HgTe-based topological Josephson junctions", Nat. Commun. **7**, 10303 (2016).

[33]A. Altland and M. R. Zirnbauer, "Nonstandard symmetry classes in mesoscopic normal-superconducting hybrid structures", Phys. Rev. B **55**, 1142 (1997).

[34]D. Sticlet, B. Nijholt, and A. Akhmerov, "Robustness of Majorana bound states in the short-junction limit", Phys. Rev. B **95**, 115421 (2017).

[35]M. Laubach, C. Platt, R. Thomale, T. Neupert, and S. Rachel, "Density wave instabilities and surface state evolution in interacting Weyl semimetals", Phys. Rev. B **94**, 241102 (2016).

[36]D. Litinski and F. von Oppen, "Quantum computing with Majorana fermion codes", Phys. Rev. B **97**, 205404 (2018).

[37]A. A. Soluyanov, D. Gresch, Z. Wang, Q. Wu, M. Troyer, X. Dai, and B. A. Bernevig, "Type-II Weyl semimetals", Nature **527**, 495 (2015).

[38]Y. Guo, X. Zhang, Z. Huang, J. Chen, Z. Luo, J. Zhang, J. Li, Z. Zhang, J. Zhao, X. Han, and H. Wu, "Quantum materials for spintronic applications", npj Spintronics **2**, 36 (2024).

[39]S. Chi, Z. Li, H. Yu, G. Wang, S. Wang, H. Zhang, and J. Wang, "Symmetrical broken and nonlinear response of weyl semimetal taas influenced by the topological surface states and weyl nodes", Annalen der Physik **529**, 1600359 (2017).

[40]S. Nadj-Perge, I. K. Drozdov, J. Li, H. Chen, S. Jeon, J. Seo, A. H. MacDonald, B. A. Bernevig, and A. Yazdani, "Observation of Majorana fermions in ferromagnetic atomic chains on a superconductor", Science **346**, 602 (2014).

[41]M. Sato and S. Fujimoto, "Topological phases of noncentrosymmetric superconductors: edge states, Majorana fermions, and non-Abelian statistics", Phys. Rev. B **79**, 094504 (2009).

[42]M. Ruby, B. W. Heinrich, Y. Peng, F. von Oppen, and K. J. Franke, "Exploring a proximity-coupled co chain on Pb(110) as a possible Majorana platform", Nano Lett. **17**, 4473 (2017).

[43]P. Zhang and F. Nori, "Majorana bound states in a disordered quantum dot chain", New Journal of Physics **18**, 043033 (2016).

[44]E. Prada, P. San-Jose, M. W. A. de Moor, A. Geresdi, E. J. H. Lee, J. Klinovaja, D. Loss, J. Nygård, R. Aguado, and L. P. Kouwenhoven, "From Andreev to Majorana bound states in hybrid superconductor–semiconductor nanowires", Nat. Rev. Phys. **2**, 575 (2020).

[45]S. Rahul, R. R. Kumar, Y. R. Kartik, and S. Sarkar, "Majorana zero modes and bulk-boundary correspondence at quantum criticality", Journal of the Physical Society of Japan **90**, 094706 (2021).

[46]C. J. Bolech and E. Demler, "Observing majorana bound states in p-wave superconductors using noise measurements in tunneling experiments", Phys. Rev. Lett. **98**, 237002 (2007).

[47]C. S. Amorim, K. Ebihara, A. Yamakage, Y. Tanaka, and M. Sato, "Majorana braiding dynamics in nanowires", Phys. Rev. B **91**, 174305 (2015).

[48]D. J. Clarke, J. D. Sau, and S. Das Sarma, "Probability and braiding statistics in majorana nanowires", Phys. Rev. B **95**, 155451 (2017).

[49]S. K. Kim, S. Tewari, and Y. Tserkovnyak, "Control and braiding of majorana fermions bound to magnetic domain walls", Phys. Rev. B **92**, 020412 (2015).

[50]A. J. Heeger, S. Kivelson, J. R. Schrieffer, and W. .-. Su, "Solitons in conducting polymers", Rev. Mod. Phys. **60**, 781 (1988).

[51]J. D. S. Bommer, H. Zhang, Ö. Gül, B. Nijholt, M. Wimmer, F. N. Rybakov, J. Garaud, D. Rodic, E. Babaev, M. Troyer, D. Car, S. R. Plissard, E. P. A. M. Bakkers, K. Watanabe, T. Taniguchi, and L. P. Kouwenhoven, "Spin-orbit protection of induced superconductivity in Majorana nanowires", Phys. Rev. Lett. **122**, 187702 (2019).

[52]M. T. Deng, C. L. Yu, G. Y. Huang, M. Larsson, P. Caroff, and H. Q. Xu, "Anomalous zero-bias conductance peak in a Nb–InSb nanowire–Nb hybrid device", Nano Lett. **12**, 6414 (2012).

[53]K.-H. Jin and F. Liu, "1D topological phases in transition-metal monochalcogenide nanowires", Nanoscale **12**, 14661 (2020).

[54]A. Das, Y. Ronen, Y. Most, Y. Oreg, M. Heiblum, and H. Shtrikman, "Zero-bias peaks and splitting in an Al-InAs nanowire topological superconductor as a signature of majorana fermions", Nat. Phys. **8**, 887 (2012).

[55]T.-P. Choy, J. M. Edge, A. R. Akhmerov, and C. W. J. Beenakker, "Majorana fermions emerging from magnetic nanoparticles on a superconductor without spin-orbit coupling", Phys. Rev. B **84**, 195442 (2011).

[56]B. Braunecker and P. Simon, "Interplay between classical magnetic moments and superconductivity in quantum one-dimensional conductors: toward a self-sustained topological Majorana phase", Phys. Rev. Lett. **111**, 147202 (2013).

[57]H. Kim, A. Palacio-Morales, T. Posske, L. Rózsa, K. Palotás, L. Szunyogh, M. Thorwart, and R. Wiesendanger, "Toward tailoring Majorana bound states in artificially constructed magnetic atom chains on elemental superconductors", Sci. Adv. **4**, eaar5251 (2018).

[58]R. M. Lutchyn, J. D. Sau, and S. Das Sarma, "Majorana fermions and a topological phase transition in semiconductor-superconductor heterostructures", Phys. Rev. Lett. **105**, 077001 (2010).

[59]J. Klinovaja and D. Loss, "Composite Majorana fermion wave functions in nanowires", Phys. Rev. B **86**, 085408 (2012).

[60]Y. Oreg, G. Refael, and F. von Oppen, "Helical liquids and Majorana bound states in quantum wires", Phys. Rev. Lett. **105**, 177002 (2010).

[61]E. Dumitrescu, B. Roberts, S. Tewari, J. D. Sau, and S. Das Sarma, "Majorana fermions in chiral topological ferromagnetic nanowires", Phys. Rev. B **91**, 094505 (2015).

[62]J. Alicea, "New directions in the pursuit of Majorana fermions in solid state systems", Rep. Prog. Phys. **75**, 076501 (2012).

[63]J. C. Y. Teo and C. L. Kane, "Topological defects and gapless modes in insulators and superconductors", Phys. Rev. B **82**, 115120 (2010).

[64]S. Tewari and J. D. Sau, "Topological invariants for spin-orbit coupled superconductor nanowires", Phys. Rev. Lett. **109**, 150408 (2012).

[65]G.-Y. Huang and H. Q. Xu, "Majorana fermions in topological-insulator nanowires: from single superconducting nanowires to Josephson junctions", Phys. Rev. B **95**, 155420 (2017).

[66]A. Kobiałka, N. Sedlmayr, M. M. Maśka, and T. Domański, "Dimerization-induced topological superconductivity in a rashba nanowire", Phys. Rev. B **101**, 085402 (2020).

[67]A. Kobiałka, N. Sedlmayr, and A. Ptok, "Majorana bound states in a superconducting rashba nanowire in the presence of antiferromagnetic order", Phys. Rev. B **103**, 125110 (2021).

[68]D. Crawford, E. Mascot, M. Shimizu, R. Wiesendanger, D. K. Morr, H. O. Jeschke, and S. Rachel, "Increased localization of Majorana modes in antiferromagnetic chains on superconductors", Phys. Rev. B **107**, 075410 (2023).

[69]K. T. Law, P. A. Lee, and T. K. Ng, "Majorana fermion induced resonant Andreev reflection", Phys. Rev. Lett. **103**, 237001 (2009).

[70]F. Nichele, A. C. C. Drachmann, A. M. Whiticar, E. C. T. O'Farrell, H. J. Suominen, A. Fornieri, T. Wang, G. C. Gardner, C. Thomas, A. T. Hatke, P. Krogstrup, M. J. Manfra, K. Flensberg, and C. M. Marcus, "Scaling of majorana zero-bias conductance peaks", Phys. Rev. Lett. **119**, 136803 (2017).

[71]M. T. Deng, S. Vaitiekėnas, E. B. Hansen, J. Danon, M. Leijnse, K. Flensberg, J. Nygård, P. Krogstrup, and C. M. Marcus, "Majorana bound state in a coupled quantum-dot hybrid-nanowire system", Science **354**, 1557 (2016).

[72]D. Bagrets and A. Altland, "Class D spectral peak in Majorana quantum wires", Phys. Rev. Lett. **109**, 227005 (2012).

[73]G. Kells, D. Meidan, and P. W. Brouwer, "Near-zero-energy end states in topologically trivial spin-orbit coupled superconducting nanowires with a smooth confinement", Phys. Rev. B **86**, 100503 (2012).

[74]D. Goldhaber-Gordon, H. Shtrikman, D. Mahalu, D. Abusch-Magder, U. Meirav, and M. A. Kastner, "Kondo effect in a single-electron transistor", Nature **391**, 156 (1998).

[75]F. Pientka, L. I. Glazman, and F. von Oppen, "Topological superconducting phase in helical Shiba chains", Phys. Rev. B **88**, 155420 (2013).

[76]S. Jeon, Y. Xie, J. Li, Z. Wang, B. A. Bernevig, and A. Yazdani, "Distinguishing a Majorana zero mode using spin-resolved measurements", Science **358**, 772 (2017).

[77]S. Nadj-Perge, I. K. Drozdov, B. A. Bernevig, and A. Yazdani, "Proposal for realizing Majorana fermions in chains of magnetic atoms on a superconductor", Phys. Rev. B **88**, 020407 (2013).

[78]M. Ruby, F. Pientka, Y. Peng, F. von Oppen, B. W. Heinrich, and K. J. Franke, "Tunneling processes into localized subgap states in superconductors", Phys. Rev. Lett. **115**, 087001 (2015).

[79]F. Pientka, L. I. Glazman, and F. von Oppen, "Topological superconducting phase in helical Shiba chains", Phys. Rev. B **88**, 155420 (2013).

[80]J. Klinovaja, P. Stano, A. Yazdani, and D. Loss, "Topological superconductivity and Majorana fermions in RKKY systems", Phys. Rev. Lett. **111**, 186805 (2013).

[81]M. M. Vazifeh and M. Franz, "Self-organized topological state with Majorana fermions", Phys. Rev. Lett. **111**, 206802 (2013).

[82]B. Braunecker and P. Simon, "Self-stabilizing temperature-driven crossover between topological and nontopological ordered phases in one-dimensional conductors", Phys. Rev. B **92**, 241410 (2015).

[83]G. M. Andolina and P. Simon, "Topological properties of chains of magnetic impurities on a superconducting substrate: interplay between the Shiba band and ferromagnetic wire limits", Phys. Rev. B **96**, 235411 (2017).

[84]V. Kaladzhyan, P. Simon, and M. Trif, "Controlling topological superconductivity by magnetization dynamics", Phys. Rev. B **96**, 020507 (2017).

[85]R. Aguado, "Majorana quasiparticles in condensed matter", Riv. Nuovo Cim. **40**, 523 (2017).

[86]R. Pawlak, S. Hoffman, J. Klinovaja, D. Loss, and E. Meyer, "Majorana fermions in magnetic chains", Prog. Part. Nucl. Phys. **107**, 1 (2019).

[87]R. Pawlak, M. Kisiel, J. Klinovaja, T. Meier, S. Kawai, T. Glatzel, D. Loss, and E. Meyer, "Probing atomic structure and Majorana wavefunctions in mono-atomic Fe chains on superconducting Pb surface", npj Quantum Inf. **2**, 16035 (2016).

[88]B. E. Feldman, M. T. Randeria, J. Li, S. Jeon, Y. Xie, Z. Wang, I. K. Drozdov, B. Andrei Bernevig, and A. Yazdani, "High-resolution studies of the Majorana atomic chain platform", Nat. Phys. **13**, 286 (2017).

[89]H. Kim, A. Palacio-Morales, T. Posske, L. Rózsa, K. Palotás, L. Szunyogh, M. Thorwart, and R. Wiesendanger, "Toward tailoring Majorana bound states in artificially constructed magnetic atom chains on elemental superconductors", Sci. Adv. **4**, eaar5251 (2018).

[90]M. Sato, Y. Takahashi, and S. Fujimoto, "Non-Abelian topological order in s-wave superfluids of ultracold fermionic atoms", Phys. Rev. Lett. **103**, 020401 (2009).

[91]M. Sato, Y. Takahashi, and S. Fujimoto, "Non-Abelian topological orders and Majorana fermions in spin-singlet superconductors", Phys. Rev. B **82**, 134521 (2010).

[92]A. Heimes, P. Kotetes, and G. Schön, "Majorana fermions from Shiba states in an antiferromagnetic chain on top of a superconductor", Phys. Rev. B **90**, 060507 (2014).

[93]M. Steinbrecher, R. Rausch, K. T. That, J. Hermenau, A. A. Khajetoorians, M. Potthoff, R. Wiesendanger, and J. Wiebe, "Non-collinear spin states in bottom-up fabricated atomic chains", Nat. Commun. **9**, 2853 (2018).

[94]L. Schneider, P. Beck, T. Posske, D. Crawford, E. Mascot, S. Rachel, R. Wiesendanger, and J. Wiebe, "Topological shiba bands in artificial spin chains on superconductors", Nat. Phys. **17**, 943 (2021).

[95]L. Schneider, P. Beck, L. Rózsa, T. Posske, J. Wiebe, and R. Wiesendanger, "Probing the topologically trivial nature of end states in antiferromagnetic atomic chains on superconductors", Nat. Commun. **14**, 2742 (2023).

[96]L. Schneider, S. Brinker, M. Steinbrecher, J. Hermenau, T. Posske, M. dos Santos Dias, S. Lounis, R. Wiesendanger, and J. Wiebe, "Controlling in-gap end states by linking nonmagnetic atoms and artificially-constructed spin chains on superconductors", Nat. Commun. **11**, 4707 (2020).

[97]L. Schneider, P. Beck, J. Neuhaus-Steinmetz, L. Rózsa, T. Posske, J. Wiebe, and R. Wiesendanger, "Precursors of Majorana modes and their length-dependent energy oscillations probed at both ends of atomic Shiba chains", Nat. Nanotechnol. **17**, 384 (2022).

[98]M. L. Amigó, Q. Stahl, A. Maljuk, A. U. B. Wolter, C. Hess, J. Geck, S. Wurmehl, S. Seiro, and B. Büchner, "Revisiting the influence of fe excess in the synthesis of $BaFe_2S_3$", Phys. Rev. Mater. **5**, 094801 (2021).

[99]H. Takahashi, A. Sugimoto, Y. Nambu, T. Yamauchi, Y. Hirata, T. Kawakami, M. Avdeev, K. Matsubayashi, F. Du, C. Kawashima, H. Soeda, S. Nakano, Y. Uwatoko, Y. Ueda, T. J. Sato, and K. Ohgushi, "Pressure-induced superconductivity in the iron-based ladder material $BaFe_2S_3$", Nat. Mater. **14**, 1008 (2015).

[100]H. Hong and H. Steinfink, "The crystal chemistry of phases in the Ba-Fe-S and Se systems", J. Solid State Chem. **5**, 93 (1972).

[101]Z. V. Popović, M. Šćepanović, N. Lazarević, M. Opačić, M. M. Radonjić, D. Tanasković, H. Lei, and C. Petrovic, "Lattice dynamics of $BaFe_2X_3$ (X=S, Se) compounds", Phys. Rev. B **91**, 064303 (2015).

[102]Y. Zhang, L.-F. Lin, J.-J. Zhang, E. Dagotto, and S. Dong, "Sequential structural and antiferromagnetic transitions in $BaFe_2Se_3$ under pressure", Phys. Rev. B **97**, 045119 (2018).

[103]S. Dong, J.-M. Liu, and E. Dagotto, "$BaFe_2Se_3$: a high T_C magnetic multiferroic with large ferrielectric polarization", Phys. Rev. Lett. **113**, 187204 (2014).

[104]W. Zheng, V. Balédent, M. B. Lepetit, P. Retailleau, E. V. Elslande, C. R. Pasquier, P. Auban-Senzier, A. Forget, D. Colson, and P. Foury-Leylekian, "Room temperature polar structure and multiferroicity in $BaFe_2Se_3$", Phys. Rev. B **101**, 020101 (2020).

[105]W. G. Zheng, V. Balédent, L. Bocher, A. Forget, D. Colson, and P. Foury-Leylekian, "Origin of spin-glass-like magnetic anomaly in the superconducting and multiferroic spin ladder $BaFe_2Se_3$", Phys. Rev. B **107**, 024423 (2023).

[106]H. Lei, H. Ryu, A. I. Frenkel, and C. Petrovic, "Anisotropy in $BaFe_2Se_3$ single crystals with double chains of fese tetrahedra", Phys. Rev. B **84**, 214511 (2011).

[107]Y. Nambu, K. Ohgushi, S. Suzuki, F. Du, M. Avdeev, Y. Uwatoko, K. Munakata, H. Fukazawa, S. Chi, Y. Ueda, and T. J. Sato, "Block magnetism coupled with local distortion in the iron-based spin-ladder compound $BaFe_2Se_3$", Phys. Rev. B **85**, 064413 (2012).

[108]V. Svitlyk, D. Chernyshov, E. Pomjakushina, A. Krzton-Maziopa, K. Conder, V. Pomjakushin, R. Pöttgen, and V. Dmitriev, "Crystal structure of $BaFe_2Se_3$ as a function of temperature and pressure: phase transition phenomena and high-order expansion of landau potential", J. Phys.: Condens. Matter **25**, 315403 (2013).

[109]P. Kong, J. Wang, Y. Jin, C. Zhang, C. Lu, Y. Tian, and H. Chen, "Exploration of high-pressure structural transition and electronic properties of $BaFe_2S_3$", J. Phys.: Condens. Matter **31**, 115401 (2019).

[110]V. Svitlyk, G. Garbarino, A. D. Rosa, E. Pomjakushina, A. Krzton-Maziopa, K. Conder, M. Nunez-Regueiro, and M. Mezouar, "High-pressure polymorphism of $BaFe_2Se_3$", J. Phys.: Condens. Matter **31**, 085401 (2019).

[111]S. Wu, J. Yin, T. Smart, A. Acharya, C. L. Bull, N. P. Funnell, T. R. Forrest, G. Simutis, R. Khasanov, S. K. Lewin, M. Wang, B. A. Frandsen, R. Jeanloz, and R. J. Birgeneau, "Robust block magnetism in the spin ladder compound $BaFe_2Se_3$ under hydrostatic pressure", Phys. Rev. B **100**, 214511 (2019).

[112]W.-G. Zheng, V. Balédent, C. V. Colin, F. Damay, J.-P. Rueff, A. Forget, D. Colson, and P. Foury-Leylekian, "Universal stripe order as a precursor of the superconducting phase in pressurized $BaFe_2Se_3$ spin ladder", Commun Phys. **5**, 183 (2022).

[113]A. Krzton-Maziopa, E. Pomjakushina, V. Pomjakushin, D. Sheptyakov, D. Chernyshov, V. Svitlyk, and K. Conder, "The synthesis, and crystal and magnetic structure of the iron selenide $BaFe_2Se_3$ with possible superconductivity at $T_c = 11$ K", J. Phys.: Condens. Matter **23**, 402201 (2011).

[114]J. Ying, H. Lei, C. Petrovic, Y. Xiao, and V. V. Struzhkin, "Interplay of magnetism and superconductivity in the compressed Fe-ladder compound $BaFe_2Se_3$", Phys. Rev. B **95**, 241109 (2017).

[115]H. Sun, X. Li, Y. Zhou, J. Yu, B. A. Frandsen, S. Wu, Z. Xu, S. Jiang, Q. Huang, E. Bourret-Courchesne, L. Sun, J. W. Lynn, R. J. Birgeneau, and M. Wang, "Nonsuperconducting electronic ground state in pressurized $BaFe_2S_3$ and $BaFe_2S_{2.5}Se_{0.5}$", Phys. Rev. B **101**, 205129 (2020).

[116]J. M. Caron, J. R. Neilson, D. C. Miller, K. Arpino, A. Llobet, and T. M. McQueen, "Orbital-selective magnetism in the spin-ladder iron selenides $Ba_{1-x}K_xFe_2Se_3$", Phys. Rev. B **85**, 180405 (2012).

[117]N. D. Patel, A. Nocera, G. Alvarez, A. Moreo, S. Johnston, and E. Dagotto, "Fingerprints of an orbital-selective Mott phase in the block magnetic state of $BaFe_2Se_3$ ladders", Commun. Phys. **2**, 64 (2019).

[118]J. M. Caron, J. R. Neilson, D. C. Miller, A. Llobet, and T. M. McQueen, "Iron displacements and magnetoelastic coupling in the antiferromagnetic spin-ladder compound $BaFe_2Se_3$", Phys. Rev. B **84**, 180409 (2011).

[119]M. Mourigal, S. Wu, M. B. Stone, J. R. Neilson, J. M. Caron, T. M. McQueen, and C. L. Broholm, "Block magnetic excitations in the orbitally selective Mott insulator $BaFe_2Se_3$", Phys. Rev. Lett. **115**, 047401 (2015).

[120]J. Rincón, A. Moreo, G. Alvarez, and E. Dagotto, "Exotic magnetic order in the orbital-selective Mott regime of multiorbital systems", Phys. Rev. Lett. **112**, 106405 (2014).

[121]J. Herbrych, N. Kaushal, A. Nocera, G. Alvarez, A. Moreo, and E. Dagotto, "Spin dynamics of the block orbital-selective Mott phase", Nat. Commun. **9**, 3736 (2018).

[122]M. Środa, E. Dagotto, and J. Herbrych, "Quantum magnetism of iron-based ladders: blocks, spirals, and spin flux", Phys. Rev. B **104**, 045128 (2021).

[123]J. Gao, Y. Teng, W. Liu, S. Chen, W. Tong, M. Li, X. Zhao, and X. Liu, "The synthesis and magnetic properties of $BaFe_2Se_3$ single crystals", RSC Adv. **7**, 30433 (2017).

[124]P. Materne, W. Bi, J. Zhao, M. Y. Hu, M. L. Amigó, S. Seiro, S. Aswartham, B. Büchner, and E. E. Alp, "Bandwidth controlled insulator-metal transition in $BaFe_2S_3$: a Mössbauer study under pressure", Phys. Rev. B **99**, 020505 (2019).

[125]C.-X. Liu, J. D. Sau, T. D. Stanescu, and S. Das Sarma, "Andreev bound states versus Majorana bound states in quantum dot-nanowire-superconductor hybrid structures: trivial versus topological zero-bias conductance peaks", Phys. Rev. B **96**, 075161 (2017).

[126]C. Beenakker, "Search for Majorana fermions in superconductors", Annu. Rev. Condens. Matter Phys. **4**, 113 (2013).

[127]J. E. Moore, "The birth of topological insulators", Nature **464**, 194 (2010).

[128]L. Fu, C. L. Kane, and E. J. Mele, "Topological insulators in three dimensions", Phys. Rev. Lett. **98**, 106803 (2007).

[129]K. Majhi, K. Pal, H. Lohani, A. Banerjee, P. Mishra, A. K. Yadav, R. Ganesan, B. R. Sekhar, U. V. Waghmare, and P. S. Anil Kumar, "Emergence of a weak topological insulator from the Bi_xSe_y family", Appl. Phys. Lett. **110**, 162102 (2017).

[130]M. Eschbach, M. Lanius, C. Niu, E. Młyńczak, P. Gospodarič, J. Kellner, P. Schüffelgen, M. Gehlmann, S. Döring, E. Neumann, M. Luysberg, G. Mussler, L. Plucinski, M. Morgenstern, D. Grützmacher, G. Bihlmayer, S. Blügel, and C. M. Schneider, "Bi_1Te_1 is a dual topological insulator", Nat. Commun. **8**, 14976 (2017).

[131]F. D. M. Haldane, "Model for a quantum Hall effect without landau levels: condensed-matter realization of the "parity anomaly"", Phys. Rev. Lett. **61**, 2015 (1988).

[132]D. Hsieh, D. Qian, L. Wray, Y. Xia, Y. S. Hor, R. J. Cava, and M. Z. Hasan, "A topological Dirac insulator in a quantum spin Hall phase", Nature **452**, 970 (2008).

[133]L. Fu and C. L. Kane, "Topological insulators with inversion symmetry", Phys. Rev. B **76**, 045302 (2007).

[134]J. C. Y. Teo, L. Fu, and C. L. Kane, "Surface states and topological invariants in three-dimensional topological insulators: application to $Bi_{1-x}Sb_x$", Phys. Rev. B **78**, 045426 (2008).

[135]B. Yan, C.-X. Liu, H.-J. Zhang, C.-Y. Yam, X.-L. Qi, T. Frauenheim, and S.-C. Zhang, "Theoretical prediction of topological insulators in thallium-based III-V-VI_2 ternary chalcogenides", EPL **90**, 37002 (2010).

[136]T. Sato, K. Segawa, H. Guo, K. Sugawara, S. Souma, T. Takahashi, and Y. Ando, "Direct evidence for the Dirac-cone topological surface states in the ternary chalcogenide $TlBiSe_2$", Phys. Rev. Lett. **105**, 136802 (2010).

[137]B. Yan, H.-J. Zhang, C.-X. Liu, X.-L. Qi, T. Frauenheim, and S.-C. Zhang, "Theoretical prediction of topological insulator in ternary rare earth chalcogenides", Phys. Rev. B **82**, 161108 (2010).

[138]H. Jin, J.-H. Song, A. J. Freeman, and M. G. Kanatzidis, "Candidates for topological insulators: Pb-based chalcogenide series", Phys. Rev. B **83**, 041202 (2011).

[139]C. Brüne, C. X. Liu, E. G. Novik, E. M. Hankiewicz, H. Buhmann, Y. L. Chen, X. L. Qi, Z. X. Shen, S. C. Zhang, and L. W. Molenkamp, "Quantum Hall effect from the topological surface states of strained bulk HgTe", Phys. Rev. Lett. **106**, 126803 (2011).

[140]D. Xiao, Y. Yao, W. Feng, J. Wen, W. Zhu, X.-Q. Chen, G. M. Stocks, and Z. Zhang, "Half-heusler compounds as a new class of three-dimensional topological insulators", Phys. Rev. Lett. **105**, 096404 (2010).

[141]X. M. Zhang, G. Z. Xu, Y. Du, E. K. Liu, Z. Y. Liu, W. H. Wang, and G. H. Wu, "A new class of topological insulators from I-III-IV half-heusler compounds with strong band inversion strength", J. Appl. Phys. **115**, 083704 (2014).

[142]J. C. Souza, M. V. Ale Crivillero, H. Dawczak-Dębicki, A. Ptok, P. G. Pagliuso, and S. Wirth, "Tuning the topological character of half-Heusler systems: a comparative study on YTBi (T = Pd, Pt)", Phys. Rev. B **108**, 165154 (2023).

[143]W. Feng, D. Xiao, J. Ding, and Y. Yao, "Three-dimensional topological insulators in I-III-VI_2 and II-IV-V_2 chalcopyrite semiconductors", Phys. Rev. Lett. **106**, 016402 (2011).

[144]W. Zhang, R. Yu, W. Feng, Y. Yao, H. Weng, X. Dai, and Z. Fang, "Topological aspect and quantum magnetoresistance of β-Ag_2Te", Phys. Rev. Lett. **106**, 156808 (2011).

[145]M. Yang and W.-M. Liu, "The d-p band-inversion topological insulator in bismuth-based skutterudites", Sci. Rep. **4**, 5131 (2014).

[146]T. H. Hsieh, H. Lin, J. Liu, W. Duan, A. Bansil, and L. Fu, "Topological crystalline insulators in the snte material class", Nat. Commun. **3**, 982 (2012).

[147]X. Wan, A. M. Turner, A. Vishwanath, and S. Y. Savrasov, "Topological semimetal and Fermi-arc surface states in the electronic structure of pyrochlore iridates", Phys. Rev. B **83**, 205101 (2011).

[148]M. Dzero, J. Xia, V. Galitski, and P. Coleman, "Topological kondo insulators", Annu. Rev. Condens. Matter Phys. **7**, 249 (2016).

[149]Z. Wang, Y. Sun, X.-Q. Chen, C. Franchini, G. Xu, H. Weng, X. Dai, and Z. Fang, "Dirac semimetal and topological phase transitions in A_3Bi (A = Na, K, Rb)", Phys. Rev. B **85**, 195320 (2012).

[150]E. V. Gorbar, V. A. Miransky, I. A. Shovkovy, and P. O. Sukhachov, "Dirac semimetals A_3Bi (A = Na, K, Rb) as $\mathbb{Z}_2$ Weyl semimetals", Phys. Rev. B **91**, 121101 (2015).

[151]A. A. Burkov and L. Balents, "Weyl semimetal in a topological insulator multilayer", Phys. Rev. Lett. **107**, 127205 (2011).

[152]M.-X. Deng, W. Luo, R.-Q. Wang, L. Sheng, and D. Y. Xing, "Weyl semimetal induced from a Dirac semimetal by magnetic doping", Phys. Rev. B **96**, 155141 (2017).

[153]H. Ness, I. Leahy, A. Rice, D. Pashov, K. Alberi, and M. van Schilfgaarde, *Doping topological Dirac semimetal with magnetic impurities: electronic structure of Mn-doped* Cd_3As_2, arXiv:2505.06662, 2025.

[154]W. J. Lee, Y. A. Salawu, H.-J. Kim, C. W. Jang, S. Kim, T. Ratcliff, R. G. Elliman, Z. Yue, X. Wang, S.-E. Lee, M.-H. Jung, J.-S. Rhyee, and S.-H. Choi, "Possible permanent Dirac- to Weyl-semimetal phase transition by ion implantation", NPG Asia Mater. **14**, 31 (2022).

[155]H. Weng, C. Fang, Z. Fang, B. A. Bernevig, and X. Dai, "Weyl semimetal phase in noncentrosymmetric transition-metal monophosphides", Phys. Rev. X **5**, 011029 (2015).

[156]N. P. Armitage, E. J. Mele, and A. Vishwanath, "Weyl and Dirac semimetals in three-dimensional solids", Rev. Mod. Phys. **90**, 015001 (2018).

[157]C. Wang, Y. Zhang, J. Huang, S. Nie, G. Liu, A. Liang, Y. Zhang, B. Shen, J. Liu, C. Hu, Y. Ding, D. Liu, Y. Hu, S. He, L. Zhao, L. Yu, J. Hu, J. Wei, Z. Mao, Y. Shi, X. Jia, F. Zhang, S. Zhang, F. Yang, Z. Wang, Q. Peng, H. Weng, X. Dai, Z. Fang, Z. Xu, C. Chen, and X. J. Zhou, "Observation of Fermi arc and its connection with bulk states in the candidate type-II Weyl semimetal WTe_2", Phys. Rev. B **94**, 241119 (2016).

[158]C. M. Acosta, R. Ouyang, A. Fazzio, M. Scheffler, L. M. Ghiringhelli, and C. Carbogno, *Analysis of topological transitions in two-dimensional materials by compressed sensing*, arXiv:1805.10950, 2018.

[159]M. Z. Hasan and C. L. Kane, "Colloquium: topological insulators", Rev. Mod. Phys. **82**, 304 (2010).

[160]V. S. Pribiag, A. J. A. Beukman, F. Qu, M. C. Cassidy, C. Charpentier, W. Wegscheider, and L. P. Kouwenhoven, "Edge-mode superconductivity in a two-dimensional topological insulator", Nature Nanotech. **10**, 593 (2015).

[161]X. Dai, T. L. Hughes, X.-L. Qi, Z. Fang, and S.-C. Zhang, "Helical edge and surface states in HgTe quantum wells and bulk insulators", Phys. Rev. B **77**, 125319 (2008).

[162]K. Deng, G. Wan, P. Deng, K. Zhang, S. Ding, E. Wang, M. Yan, H. Huang, H. Zhang, Z. Xu, J. Denlinger, A. Fedorov, H. Yang, W. Duan, H. Yao, Y. Wu, S. Fan, H. Zhang, X. Chen, and S. Zhou, "Experimental observation of topological Fermi arcs in type-II Weyl semimetal $MoTe_2$", Nat. Phys. **12**, 1105 (2016).

[163]Y. Sun, S.-C. Wu, and B. Yan, "Topological surface states and Fermi arcs of the noncentrosymmetric Weyl semimetals TaAs, TaP, NbAs, and NbP", Phys. Rev. B **92**, 115428 (2015).

[164]R. Yu, W. Zhang, H.-J. Zhang, S.-C. Zhang, X. Dai, and Z. Fang, "Quantized anomalous Hall effect in magnetic topological insulators", Science **329**, 61 (2010).

[165]H. Hong, H. Zhang, S. Lin, J. A. Dhas, B. Paudel, S. Xu, S. Chen, T. Cui, Y. Fan, D. Rong, Q. Jin, Z. Zhu, Y. Du, S. A. Chambers, C. Ge, C. Wang, Q. Zhang, L. Wang, K.-j. Jin, S. Dong, and E.-J. Guo, "Metal-to-insulator transition in oxide semimetals by anion doping", Interdisciplinary Materials **3**, 358–368 (2024).

[166]L. Chen, T. T. Han, C. Cai, Z. G. Wang, Y. D. Wang, Z. M. Xin, and Y. Zhang, "Doping-controlled transition from excitonic insulator to semimetal in Ta_2NiSe_5", Phys. Rev. B **102**, 161116 (2020).

[167]T. Ideue, M. Hirayama, H. Taiko, T. Takahashi, M. Murase, T. Miyake, S. Murakami, T. Sasagawa, and Y. Iwasa, "Pressure-induced topological phase transition in noncentrosymmetric elemental tellurium", PNAS **116**, 25530 (2019).

[168]J. Li, W. Lin, and D. X. Yao, *Strain-induced topological phase transition in two-dimensional platinum ditelluride*, arXiv:2106.16212, 2021.

[169]E. Taghizadeh Sisakht, F. Fazileh, M. H. Zare, M. Zarenia, and F. M. Peeters, "Strain-induced topological phase transition in phosphorene and in phosphorene nanoribbons", Phys. Rev. B **94**, 085417 (2016).

[170]S. Sharma and A. S. Banerjee, *Strain-tunable topological phase transitions in line- and split-graph flat-band lattices*, arXiv:2501.11783, 2025.

[171]B. A. Volkov and O. A. Pankratov, "Two-dimensional massless electrons in an inverted contact", Soviet Journal of Experimental and Theoretical Physics Letters **42**, 178 (1985).

[172]O. Pankratov, S. Pakhomov, and B. Volkov, "Supersymmetry in heterojunctions: band-inverting contact on the basis of $Pb_{1-x}Sn_xTe$ and $Hg_{1-x}Cd_xTe$", Solid State Communications **61**, 93 (1987).

[173]X. Lu and M. O. Goerbig, "Dirac quantum well engineering on the surface of a topological insulator", Phys. Rev. B **102**, 155311 (2020).

[174]S. Tchoumakov, M. Civelli, and M. O. Goerbig, "Magnetic description of the Fermi arc in type-I and type-II Weyl semimetals", Phys. Rev. B **95**, 125306 (2017).

[175]S. Tchoumakov, V. Jouffrey, A. Inhofer, E. Bocquillon, B. Pla çais, D. Carpentier, and M. O. Goerbig, "Volkov-pankratov states in topological heterojunctions", Phys. Rev. B **96**, 201302 (2017).

[176]S.-Y. Xu, I. Belopolski, N. Alidoust, M. Neupane, G. Bian, C. Zhang, R. Sankar, G. Chang, Z. Yuan, C.-C. Lee, S.-M. Huang, H. Zheng, J. Ma, D. S. Sanchez, B. Wang, A. Bansil, F. Chou, P. P. Shibayev, H. Lin, S. Jia, and M. Z. Hasan, "Discovery of a Weyl fermion semimetal and topological Fermi arcs", Science **349**, 613 (2015).